

COMPUTATION AIDED DESIGN IN
MOLECULAR NANOTECHNOLOGY

Thesis by

Wei-Qiao Deng

In Partial Fulfillment of the Requirements for the

Degree of

Doctor of Philosophy in Chemistry

CALIFORNIA INSTITUTE OF TECHNOLOGY

Pasadena, California

2004

(Defended April 23rd, 2004)

© 2004

Wei-Qiao Deng

All Rights Reserved

ACKNOWLEDGEMENTS

I wish to express my deep gratitude to my advisor, Professor William A. Goddard III, for his guidance in my PhD journey that consists of challenges and interests. His broad interest indeed showed me how many things a theorist can do. I appreciate what I have learned from him, not only the broad knowledge, sharp scientific instinct and creative ideas, but also the optimistic and confident personalities. I would also like to thank Professor Aron Kupperman, Professor Nathan S. Lewis, Professor Zheng-Gang Wang and Professor David G. Goodwin as my committee members.

I would like to thank Dr. Xin Xu, Dr. Richard P. Muller, Dr. Valeria Molinero and Sam Cheung for their collaboration in several topics and also thank all other people in the group who directly and indirectly contributed to my thesis. Especially, I would like to thank Darryl L. Willick and Shirley Wu for their warmhearted assistances.

I have spent six years at Caltech and I have had a great time here. My thanks go to all those who are responsible for this.

Funding for nano-electronics related topics came from MARCO at UCLA. I would like to thank all the collaborators at UCLA and Caltech in this project. Especially, I would like to thank Professor Fraser J. Stoddart, Professor James R. Heath and Dr. Amar Flood for their invaluable discussions.

Funding for fuel cell related topics came from General Motors. I would like to thank all the collaborators at GM fuel cell center who are pleasant to work with. Especially I would like to thank Dr. Gerald Voecks for his generous support and helpful discussions.

Finally, and most of all, I want to thank my family for their support.

ABSTRACT

We use multi-scale simulation strategy to understand, improve and rationally design novel materials with desired properties in molecular nanotechnology. The areas we have studied cover from molecular electronics, nano-structured materials to carbon nanotube technology.

In term of molecular and nano-electronics, first we used quantum mechanics to characterize the structure and current-voltage (I-V) performance of the Stoddart-Heath rotaxane-based programmable electronic switch. This methodology established a basis for iterative experimental-theoretical efforts to optimize systems for molecule-based electronics. We extended this switch principle and rationally designed an ultrafast molecular switch, proton-hopping molecular switch. Second we developed a kinetic model to study the hole mobility in organic semiconductor. After screening several designs, we presented a nano-bracelet as a competitive organic semiconductor.

We studied several topics related to the applications of nano-structured materials in fuel cell technology. Based on our simulation, we proposed a new kind of carbon-based materials for hydrogen storage. It can satisfy the target set up by the Department of Energy, USA. We develop a kinetic model to study the proton diffusion in proton exchange membrane of hydrogen fuel cell. We validated our proposed system, fluorinated imidazole impregnated nafion, as the candidate that can transfer proton above 100 °C at water – free media.

In term of carbon nanotube technology, we explored the reason why bimetallic catalysts are 10-100 times better than mono-metals at assisting single wall carbon nanotube growth. Based on our proposed two-stage growth mechanism, we screened and designed a better catalysis.

TABLE OF CONTENTS

Acknowledgements.....	iii
Abstract	iv
Table of Contents	v
Chapter I: Introduction.....	1
Section 1. Molecular and Nano-electronics	7
Chapter II: Mechanism of the Stoddart-Heath bistable rotaxane molecular switch	8
Chapter III: Ultrafast proton-hopping molecular switch	34
Chapter IV: Predictions of hole mobilities in oligoacene organic semiconductors from quantum mechanical calculations.....	52
Chapter V: The nano-bracelet, a new family of organic semiconductors.....	83
Section 2: Nano-structured materials in Fuel Cell technology.....	104
Chapter VI: Simulation of Li-doped pillared carbon based materials for reversible hydrogen storage.....	105
Chapter VII: Fluorinated imidazoles as proton carriers for water-free fuel cell membranes	132
Section 3: Carbon Nanotube technology.....	155
Chapter VIII: A two-stage mechanism of bimetallic catalyzed growth of single-wall carbon nanotubes	156
Appendix A: List of Publications	170
Appendix B: New alkali doped pillared carbon materials designed to achieve practical reversible hydrogen storage for transportation.	172

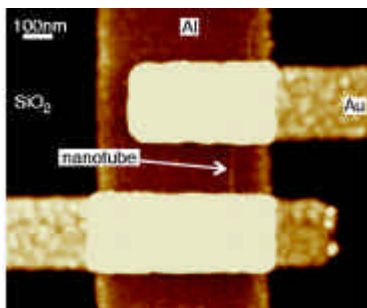
Chapter I

INTRODUCTION

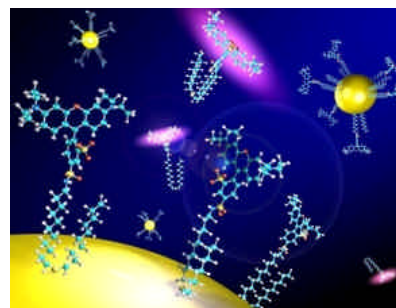
In 1959, the promise of nanotechnology was outlined by Nobel Prize laureate Richard Feynman in his famous talk, “There's Plenty of Room at the Bottom”. Since then, the concepts of molecular nanotechnology have extended to such as “molecular engineering” by Eric K. Drexler [1] and “molecular electronics” by Mark A. Ratner, [2] etc. Recently, the area of molecular nanotechnology has rapidly developed because enormous possibilities have opened to manipulate the molecular synthesis and movement. A lot of devices and applications have been demonstrated. [3] It is now not an impractical dream to fabricate molecular devices and molecular machines with atomic precision. In Figure 1, we show several highly active fields of molecular nanotechnology such as molecular electronics, carbon nanotube technology, organic electronics, self-assembly and its application, molecular machine and nano-structured materials.



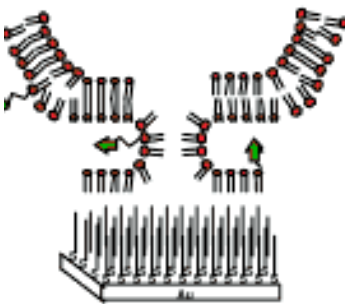
Molecular electronics



Carbon nanotube technology



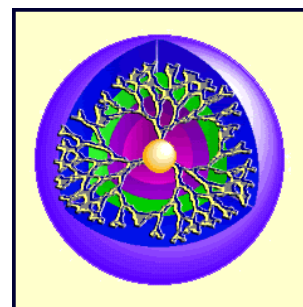
Nano Organic electronics



Self-assembly



Nano-machine



Nano-structured materials

Figure 1. Several highly active fields in nanotechnology.

Although there exists a continuing debate about the exact time frame to economically fabricate a wide range of structures with atomic precision, it is becoming acceptable that molecular nanotechnology will be the next industrial breakthrough. Most obviously a molecular manufacturing capability will be a prerequisite to the construction of molecular logic devices. It is necessary to be able to economically manufacture device at large scale with atomic precision. This capability will also require materials with expected properties that border on the limits imposed by natural law. A broad range of other nano-functionalized materials beside electronics materials will also benefit from a manufacturing process that offers atomic precision at low cost.

The promise of such remarkably high payoffs encourages people to seek the solutions, how such a system will work and how we can build such a system. Fortunately, with nowadays dramatic developing of computational technology at both hardware (computation speed) and software (parallel computation), our current understanding of chemistry and physics should be sufficient to simulate such nano systems that involves millions of atoms. It is here that the value of computational nanotechnology can be most clearly seen. We can simulate and validate thousands of designs in days even without doing any expensive experiments that may take years. With this computational nanotechnology, it becomes possible to rationally design systems at atomic precision.

Now, the challenge of computational nanotechnology is how to model a real nano system at atomistic scale and predict accurately the expected properties. To meet the challenge above, we will use the following computation aided design methodology. [4]

Figure 2 shows an overview of our computation aided design methodology. We propose three stages for designing in molecular nanotechnology.

Stage One, top-down stage: We will examine molecular devices or nano-structured materials to identify behaviors that are key to achieving desired macroscopic functionality. From this stage, we will locate the microscopic properties that dominate such macroscopic functionalities. An example is the hole or electrons mobilities. This macroscopic functionality is determined by electron transport between molecules at microscopic scale.

This may involve chemical properties of single molecules, or may involve interaction between molecules.

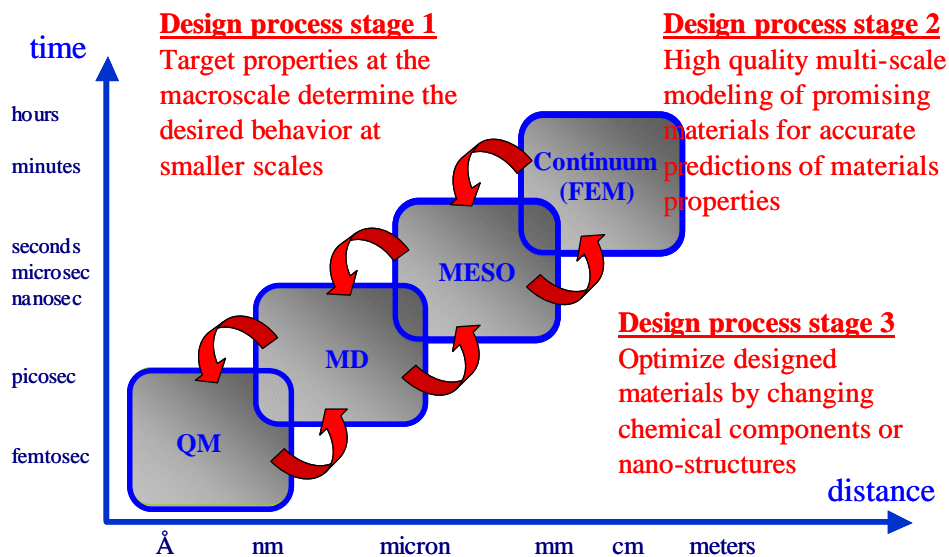


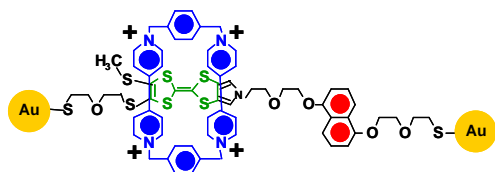
Figure 2. The multi-scale simulation strategy and design processing

Stage Two, bottom-up stage: We will seek to understand macroscopic behaviors starting from the quantum mechanics level up to the continuum level. Initially, we will investigate critical system components by using ab initio quantum mechanics (QM) simulations to examine one or one part of one molecule at a time. These small-scale simulations will give us detailed and accurate pictures of key properties without incurring enormous computational cost. We will then use data from first principle simulations to build an accurate multi-scale model without empirical parameters. Throughout the multi-scale modeling process, we will also use results of larger scale simulations as input parameters for smaller scale simulations that more accurately reflect the conditions under which molecules operate. The data from improved smaller scale simulations will then be used to build better larger scale models. In this manner, we iterate between different scales to improve the accuracy of our models.

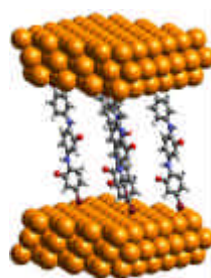
Stage Three, screening stage: We will use the methods and understanding developed in stages one and two to optimize nano-structures of devices by changing the fabrication parameters such as pressure, temperature etc, chemical components of molecules,

molecular layer alignment, electrode connection, etc. We will cooperate with the experimental side to gain quick feedback to re-design.

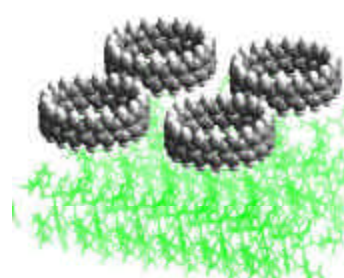
Section 1. Molecular and nano-electronics



II. Mechanism of rotaxane switch

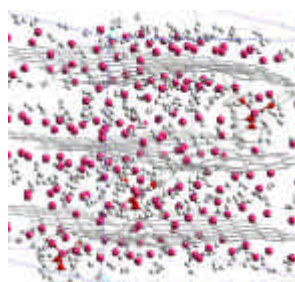


III. Proton hopping switch

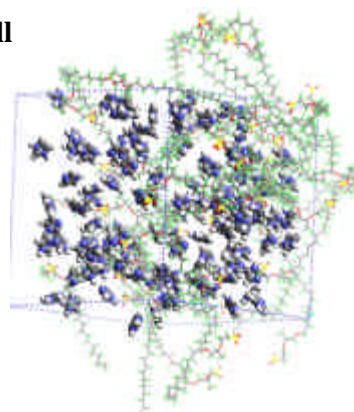


V. Nano-bracelet

Section 2. Nano-structured materials in fuel cell

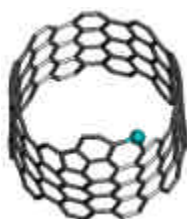


VI. Carbon based hydrogen storage



VII. Fluorinated Imidazole impregnated nafion for proton exchange membrane

Section 3. Carbon nanotube technology



VIII. Carbon nanotube growth

Figure 3. Introduction of three areas in the thesis.

Figure 3 summaries those novel designs in this thesis which we classified into three areas. They are organized as below:

Section 1 describes the understanding, improvement and rationally new design of the molecular and nano-electronics systems. This section includes Chapter II, III, IV and V.

In Chapter II, we used green functional theory combined with quantum mechanics to study rotaxane molecular switch and rationalized its switching mechanism. We found that the change in the delocalization of the MOs affected by the ring movement plays a key role in the switching mechanism. Using this mechanism we can now estimate how changes in the chemical components will change switch performance, providing a design principle for optimization.

In Chapter III, based on the principle of the configuration bistable structure switch, we presented a new design, ultrafast proton-hopping molecular switch, which is 10^6 faster than the current molecular switch. This switch may satisfy the goal of the next generation electronic device being searched by information industry.

In Chapter IV, we described the development of an incoherent kinetic model based on first principle calculation results to predict the hole mobilities of organic semiconductors. We calculated a hole mobility of $6.5 \text{ cm}^2/\text{Vs}$ for pentacene crystals at 300K. This can be compared to recent experimental results of $5 \text{ cm}^2/\text{Vs}$, suggesting that current materials are approaching the maximum for the 3D crystal. Our model might be useful to screen new materials to have a higher hole mobility.

In Chapter V, by using the developed incoherent kinetic model, we screened various designs and presented a novel material, nano-bracelet, which may have an ultra-high hole mobility, 10-600 times faster than the current ones.

Section 2 describes several novel materials designed for hydrogen proton exchange membrane fuel cell technology. Those designs are presented in Chapter VI and VII, respectively.

In Chapter VI, we discussed the topics related to hydrogen storage in nano-structured materials shown in Figure 3. We developed an accurate force field that can be used to model the weak van der waals interaction. By using this force field, we studied the hydrogen storage in carbon nanotubes and several other nano-structured materials. The best material we have obtained satisfied the requirement of DOE for hydrogen storage materials.

In Chapter VII, we discussed how we design a novel water-free proton exchange membrane that can work above 100 °C (Figure 3). Our simulation showed that fluorinated imidazole impregnated nafion has comparable proton conductivity to the unfluorinated system, however it is chemically more stable and does not poison the electrodes.

Section 3 describes the research on one of the bottleneck problems in carbon nanotube technology, i.e., how to grow carbon nanotubes efficiently. In Chapter VIII, we proposed a two-stage mechanism for bimetal catalyzed carbon nanotube growth to explain why bimetal catalyzed growth can be 100 times more efficient than monometal catalyzed growth. Based on this two-stage mechanism, we screened a number of other metals (Cr, Fe, Mo, Rh, Pd) and suggested that Mo+Ni should be the best bimetallic catalyst from combining these elements (better than Ni+Co).

Reference

- [1] Drexler, K. E. (1981) “Molecular engineering: An approach to the development of general capabilities for molecular manipulation.” Proc. Natl. Acad. Sci. U.S.A. 78:5275-5278, 1981.
- [2] Aviram A. and Ratner M. A. “Molecular rectifiers” Chem. Phys. Lett. 29: 277-283, 1974.
- [3] Heath J.R.; and Ratner M.A.; “Molecular electronics” Physics Today (5): 43-49, 2003
- [4] Goddard III, WA (2000). Materials and process simulation center (MSC).

Section 1: Molecular and Nano-electronics

Chapter II: Mechanism of the Stoddart-Heath bistable rotaxane molecular switch

Abstract	8
Content	9
Reference.....	12
Figures	14
Support Information.....	17

Chapter III: Ultrafast proton-hopping molecular switch

Abstract	34
Content	35
Reference.....	39
Figures	40
Support Information.....	44

Chapter IV: Predictions of Hole Mobilities in Oligoacene Organic Semiconductors from Quantum Mechanical Calculations

Abstract	52
Introduction	53
Theoretical Methodology.....	53
Results and Discussion	59
Reference.....	65
Figures and tables.....	68

Chapter V: The nano-bracelet, a new family of organic semiconductors

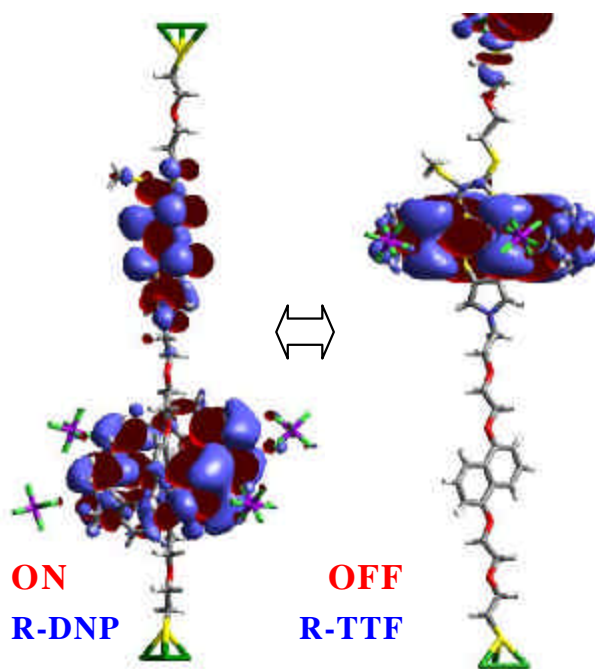
Abstract	83
Content	84
Reference.....	88
Figures	90
Support Information.....	94

*Chapter II*MECHANISM OF THE STODDART-HEATH BISTABLE ROTAXANE
MOLECULAR SWITCH *

Abstract

We use quantum mechanics to characterize the structure and current-voltage (I-V) performance of the Stoddart-Heath rotaxane-based programmable electronic switch. We find that the current when the ring is on the DNP is 37~58 times the current when the ring is on the TTF, in agreement with experiment (ratio of 10 to 100). The basis is now established for iterative experimental-theoretical efforts to optimize systems for molecule based electronics which we illustrate by predicting the effect of adding a group such as CN group to the rotaxane.

Figure for Table of Contents (LUMOs for rotaxane molecule).

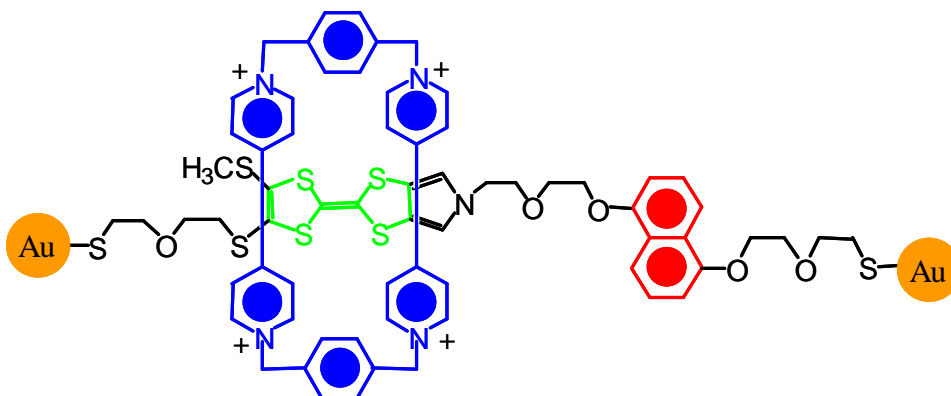


* With Richard P. Muller's assistance at initiating the interest of this system.

Molecular scale electronics is developing rapidly[1] because of advances in the synthesis of suitably tailored organic structures, bringing us closer to the ultimate miniaturization of nano-electronic devices.[2-3] A recent success by the Stoddart and Heath groups utilized rotaxanes, which have a ring component encircling the dumbbell-shaped component (Scheme 1), function as a programmable electronic switch.[4-9] The ring is a cyclobis(paraquat-p-phenylene) tetracationic macrocycle (CBPQT⁴⁺). The dumbbell is comprised of a tetrathiafulvalene (TTF) and a 1,5-dioxynaphthalene (DNP). Consequently, the ring can localize at either TTF site or DNP site along the dumbbell. The experiments showed conclusive evidence of two distinct states (one with a resistance 10 – 100 times that of the other) and that the system could be switched from one state to the other by applying two different sharp address voltages. Switching the device to an ON state is observed at the net oxidizing voltage +2 V, whereas, switching to an OFF occurs at –2V, or net reducing voltages. It is assumed that the switching behavior arises from the difference in conductivity between the two states. However, the atomistic-level mechanism of the conductivity switching is still unknown.

In order to provide the molecular level understanding necessary to design and optimize such nanoelectronic devices, we initiated theoretical studies on the mechanism of conduction for the bistable [2] rotaxane shown in scheme 1. This structure is based on a known compound [8] and for simplicity the stoppers at each end have been removed. The detailed simulation procedures are in Supportive Information (SI).

Scheme 1. The structure of the Au₃-rotaxane-Au₃ switch used in the simulation. Each Au electrode includes three Au atoms.



The calculation of electric conductivity at atomic level has been well established.[10-14] The I-V curves that were calculated by a combination of quantum mechanics [15-19] and green's function theory [12-14] for the two states of the rotaxane are shown in Figure 1. Current flow through the state with the ring on DNP group (R-DNP) increase almost linearly to 1.5 nA from 0 to 0.25 V bias and reach its maximum 1.8nA after 0.3V. However, current through the state with the ring molecule on TTF group (R-TTF) increases only to 0.05 nA at range from 0 to 0.5 V shown in the Figure 1b. The calculation results show large different conductivities between the R-DNP and R-TTF states. For applied bias from 0.01V to 0.2V, the calculated On/Off ratio increases from 37 to 58 and decreases to 39 from 0.2V to 0.5 V applied bias. This On/Off ratio is comparable to experimental values [7] of 10-100. This suggests that the simulation has captured the essence of the experimental system. In particular, we find that the switch is OFF when the ring is on the TTF group (R-TTF) and ON when the ring is on the DNP group (R-DNP). Exactly this same assignment was previously proposed. [4,8]

Next we examine the orbital basis for the switching behavior. The frontier MOs including highest occupied molecular orbital (HOMO), lowest occupied MO (LUMO), and nearby orbitals are shown in Table 1. Figure 1 shows the shapes of the HOMO and LUMO of DNP and TTF state respectively. More MOs can be found in SI. These MOs contain contributions from four groups of atoms: Au electrode atoms at each end, the TTF group, the DNP group, and the ring group: We find two states with distinct I/V differences

- R-DNP State (ON): The HOMO is delocalized over the TTF and ring groups. The LUMO and LUMO +1 (0.1 eV above the LUMO) is delocalized over the TTF and ring-DNP groups. HOMO-1 is localized near the upper Au electrode.

- R-TTF State (OFF): HOMO-2 is localized at DNP; LUMO and LUMO+1 is localized at the TTF. HOMO-1 and HOMO are mostly localized at the electrodes.

Since the transmission function determines the electrical properties of the system, we establish a correspondence between the molecular MOs with the peaks in the transmission function. The correlation is shown in Figure 3. The frontier MOs exactly match the peaks

in the transmission function (except for the MOs localized on Au, which do not contribute to conductivity). For the R-DNP/ON state, HOMO, LUMO and LUMO+1 correspond to the three peaks in Figure 3 where HOMO contributes the highest peak (blue) because it is the most delocalized MO. For the R-TTF/OFF state, the HOMO-2, LUMO and LUMO+1 lead to three peaks (pink). These MOs are localized leading to transmission peaks 10 to 1000 times smaller than the peaks of the ON state. Thus, we conclude that the characteristics of MOs around the Fermi energy determine the electrical conductivities of Au-rotaxane-Au system.

With a plausible mechanism for understanding the switch in the rotaxane system, we can now use this mechanism to design improved devices. For example chemical groups could be attached to the rotaxane molecule so as to shift the frontier orbitals to make them more localized for the OFF state and/or more delocalized for the ON state. Therefore, to optimize the rotaxane switch we are considering changes like those in scheme 2, where each component of the switch can be functionalized separately. Which group best optimizes the switch depends upon which frontier orbital is tuned. To illustrate the procedure, we added a CN group, an electron acceptor on the DNP site to shift the characteristic of that orbital and change the distribution of the frontier orbitals. The red curve in Figure 3 shows the transmission with CN modification. The CN addition makes LUMO+1 more localized leading to a smaller transmission. This suggests that we should add the CN instead to the TTF region.

Summarizing, we used quantum mechanics methods to simulate the performance of the Stoddart-Heath rotaxane switch. We find two states with a ~40 to 60 difference in conductance in good agreement with experiment. In addition we determined that the ring over DNP group is the ON state while the ring over TTF group is OFF, supporting the mechanism proposed by Stoddart. The change in the delocalization of the MOs affected by the ring movement plays a key role in the switching mechanism. Using this mechanism we can now estimate how changes in the chemical components will change switch performance, providing a design principle for optimization.

ACKNOWLEDGMENT We thank Fraser Stoddart and James Heath for helpful discussions and thank Xin Xu and Amar Flood for helpful suggestions. We thank Supriyo Datta and his group who provided details of their Huckel-IV 2.0 program. This research was supported by NSF-NIRT.

Reference

1. Tseng, G.Y.; Ellenbogen, J.C.; Science 2001 294, 1293.
2. Feynmann, R. P. In Miniaturization; Gilbert, H. D., Ed.; Reinhold: New York, 1961; p 282.
3. Aviram, A.; Ratner, M. A. Chem. Phys. Lett. 1974, 29, 277.
4. Collier C.P.; Mattersteig G.; Wong E.W.; Luo Y.; Beverly K.; Sampaio J.; Raymo F.M.; Stoddart J.F.; Heath J.R.; Science 2000, 289, 1172.
5. Wong E.W.; Collier C.P.; Behloradsky M.; Raymo F.M.; Stoddart J.F.; Heath J.R.; J. Am. Chem. Soc. 2000, 122, 5831.
6. Collier C.P.; Wong E.W.; Belohradsky M.; Raymo F.M.; Stoddart J.F.; Kuekes P.J.; Williams R.S.; Heath J.R., Science 1999, 285, 391.
7. Collier C.P.; Jeppesen J.O.; Luo Y.; Perkins J.; Wong E.W.; Heath J.R.; Stoddart J.F.; J. Am. Chem. Soc. 2001, 123, 12632.
8. Luo Y., Collier C. P., Jeppesen, J. O., Nielsen K. A., Delonno, E. and et. al Chemphyschem 2002, 3, 519
9. Pease, A. R. ; Jeppesen, J. O., Stoddart, J. F., Luo, Y., Collier C. P. and Heath, J. R. Acc. Chem. Res. 2001, 34, 433
10. Lang, N.D. Phys. Rev. B 1995, 52, 5335; Lang, N.D. Phys. Rev. Lett. 1997, 79, 1357.

11. Datta, S. *Electronic Transport in Mesoscopic Physics*; Oxford University Press: Oxford, 1997.
12. Yaliraki S.N.; Roitberg A.E.; Gonzalez C.; Mujica V.; Ratner M.A. *J. Chem. Phys* 1999, 111, 6997
13. Xue, Y.Q.; Datta S.; Ratner, M.A. *J. Chem. Phys.* 2001, 115, 4292
14. Seminario, J. M.; Zacarias, A.G.; Derosa, P.A. *J. Phys. Chem. A* 2001, 105, 791.
15. Mayo, S. L.; Olafson, B.D.; Goddard, W.A. *J. Chem. Phys.* 1990, 94, 8897
16. Mopac2000 package. Schrodinger Inc.
17. Hay, P. J. and Wadt, W.R. *J. Chem. Phys.* 1985, 82, 299.
18. Jaguar 4.0 from Schrodinger Inc, Portland Oregon
19. Papaconstantopoulos D.A. *Handbook of the band structure of Elemental Solids*; Plenum Press: New York, 1986.
20. Supporting material is available

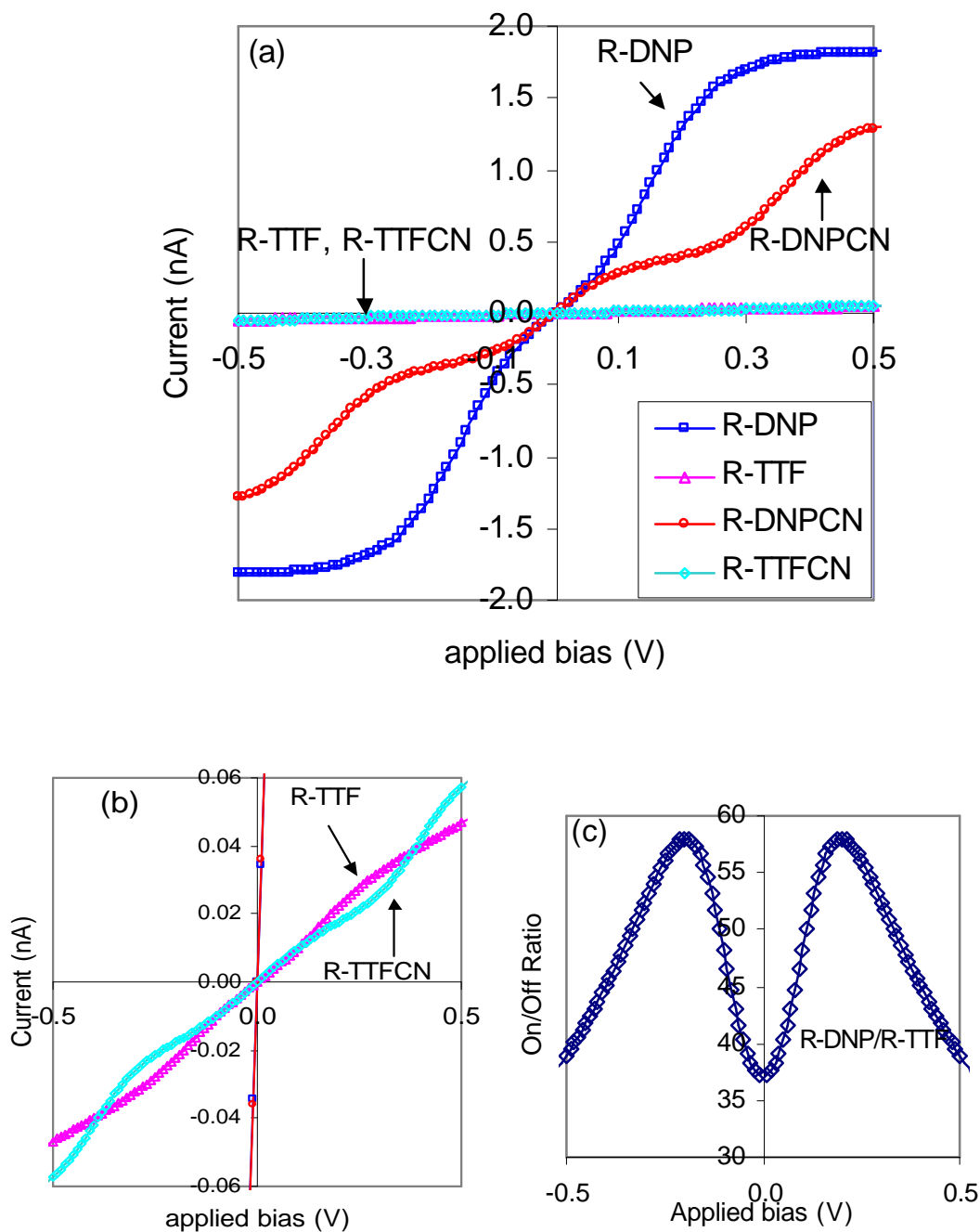


Figure 1. I-V curve of Au-rotaxane-Au switch. (a) The four I-V curves correspond to ring on DNP (R-DNP), on TTF (R-TTF) and for the modified version of the rotaxane bearing a CN group substituted on the DNP unit, R-DNPCN, and R-TTFCN states. (b) Small scale I-V curve of R-TTF and R-TTFCN. (c). The voltage dependent On/Off ratio.

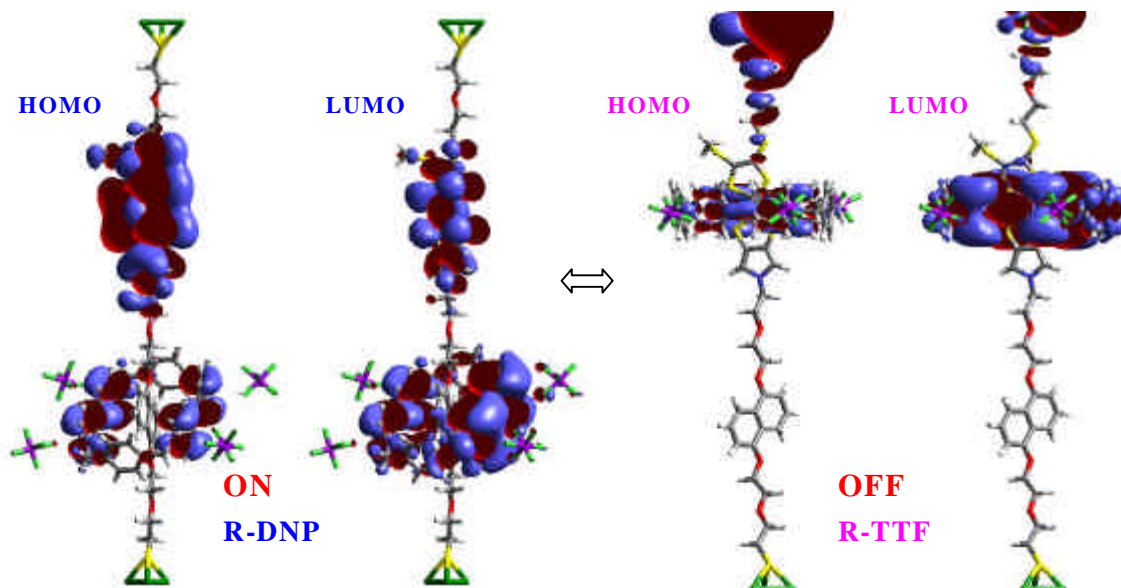
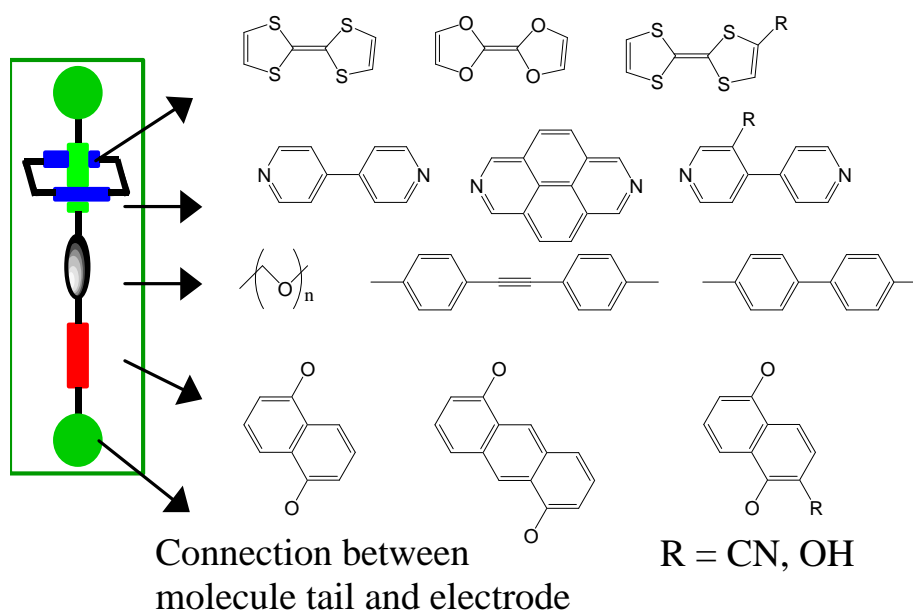


Figure 2. MOs of Au-rotaxane-Au switch. Green atoms are Au, Yellow is S, grey is C, red is oxygen and white is hydrogen. The ring is CBPQT^{4+} , with 4 PF_6^- units around. The TTF and DNP units are located at the top and bottom halves of the dumbbell, respectively. The total is 186 atoms.

Scheme 2 The strategy of the modifications for the rotaxane switch



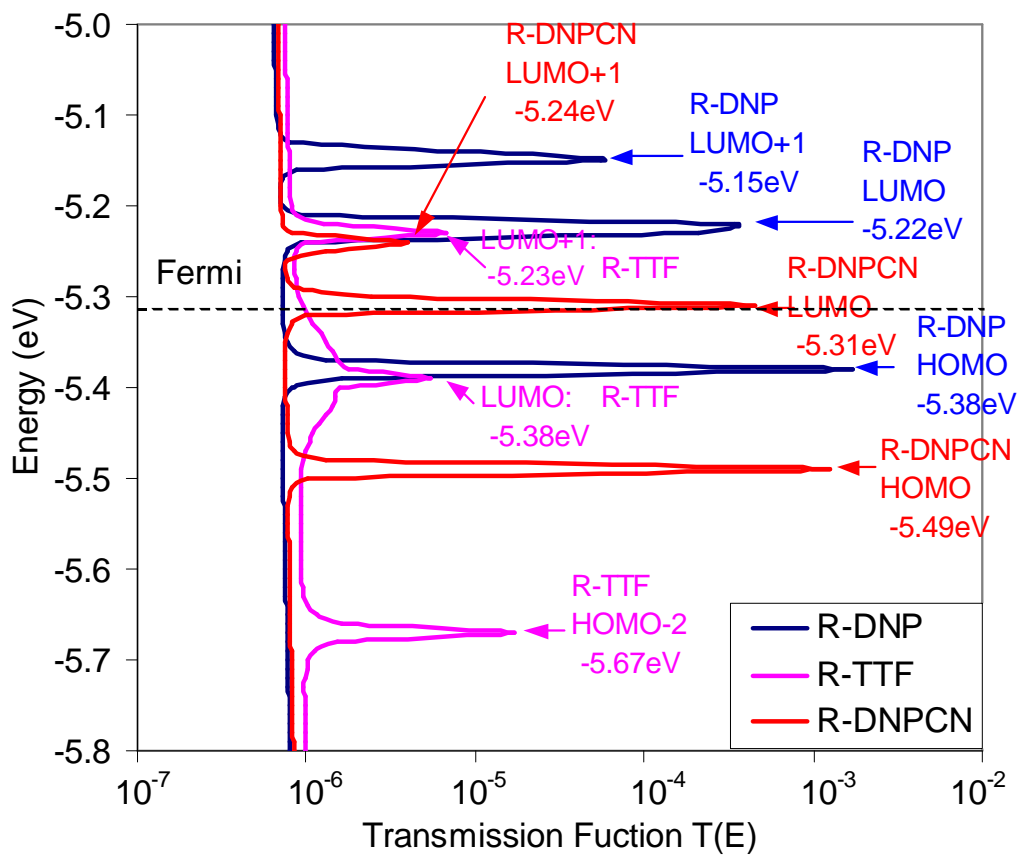


Figure 3. The transmission function of rotaxane components. Blue curve is for R-DNP, pink curve is for R-TTF and red curve is for R-DNPCN. The dash line is Fermi energy of Au electrodes, -5.31eV.

Support information:

Mechanism of the Stoddart-Heath bistable rotaxane molecular switch

Abstract

The supporting information is organized as follows:

Section S1 describes the real device and our strategy to make a minimum structure device for quantum mechanics and device simulations.

Section S2 describes the Green's Function method and procedures we use to calculate the electronic properties of the device structure described in section 1.

Section S3 shows additional detailed results from the calculations.

Section S1 Device structures and our approximation

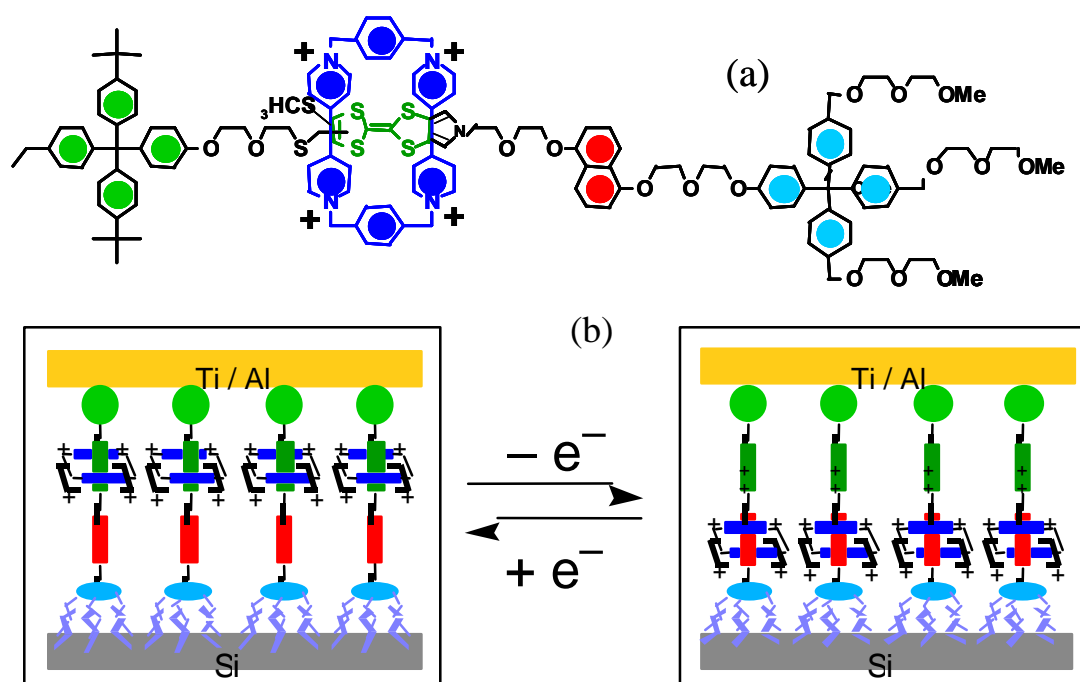


Figure S1. The scheme of Heath-Stoddart rotaxane switch

Figure S1 shows a schematic for the Heath-Stoddart rotaxane switch. The structure of the whole molecule is shown in Figure S1a. The dumbbell consists of four groups;

left green; stopper to keep ring from coming off the backbone,
TTF group green,
DNP group red, and
right blue: stopper.

The ring component can be caused to shift between the TTF and DNP group but cannot move off the dumbbell because of the left and right stoppers. Figure S1b shows the device structure, with the four components shown as colored boxes. The rotaxane was deposited on the poly-silicon surface and is expected to form a self-assembled monolayer. The second electrode, Ti/Al was deposited on the top of the monolayer.

We simplified the system as shown in Figure S2 to make the DFT calculations practical, while maintaining the essence of the rotaxane switch. From original molecule (a), we cut off the right and left stoppers and neutralize the molecule with hydrogen atoms. Then we used the Dreiding force field [15] to optimize the geometry for three structures:

ring over the TTF,
ring over the DNP, and
ring over the linker in between

In all cases the four PF_6^- counterions are included. These structures were then reoptimized using AM1 [16] quantum mechanics, leading to the result that the ring-linker structure is higher than the other two. Next we deleted the hydrogen atom at the thiol and bond the thiol to a gold trimer at each end of the rotaxane. This Au_3 was included to provide an electrode for the I/V calculations. The Au_3 was constrained to lie in the plane perpendicular to the axis and 1.9 Å from the S. At the optimum AM1 geometry, we

carried out DFT calculations (B3LYP) with the 6-31G basis on each atom except the Au atoms, where we used the Hay-Wadt core-valence effective core potential [12] (LACVP with 11 electrons per Au). We solved for the ground state Hamiltonian and orbitals for each state.[18]

To calculate the electrical conductivity, we used the Green's function formalism of Ratner and others [12-14], assuming that the coupling between the backbone of the rotaxane and the electrodes does not change as the ring moves. A DFT calculation at the B3LYP/LACVP level was performed at single point calculation to obtain the Fock Hamiltonian and Overlap matrices. These Fock and Overlap matrices were then factored into electrode (Au_3) and molecule parts. In these calculations we choose the Fermi energy as -5.31eV , just as for bulk Au metal.

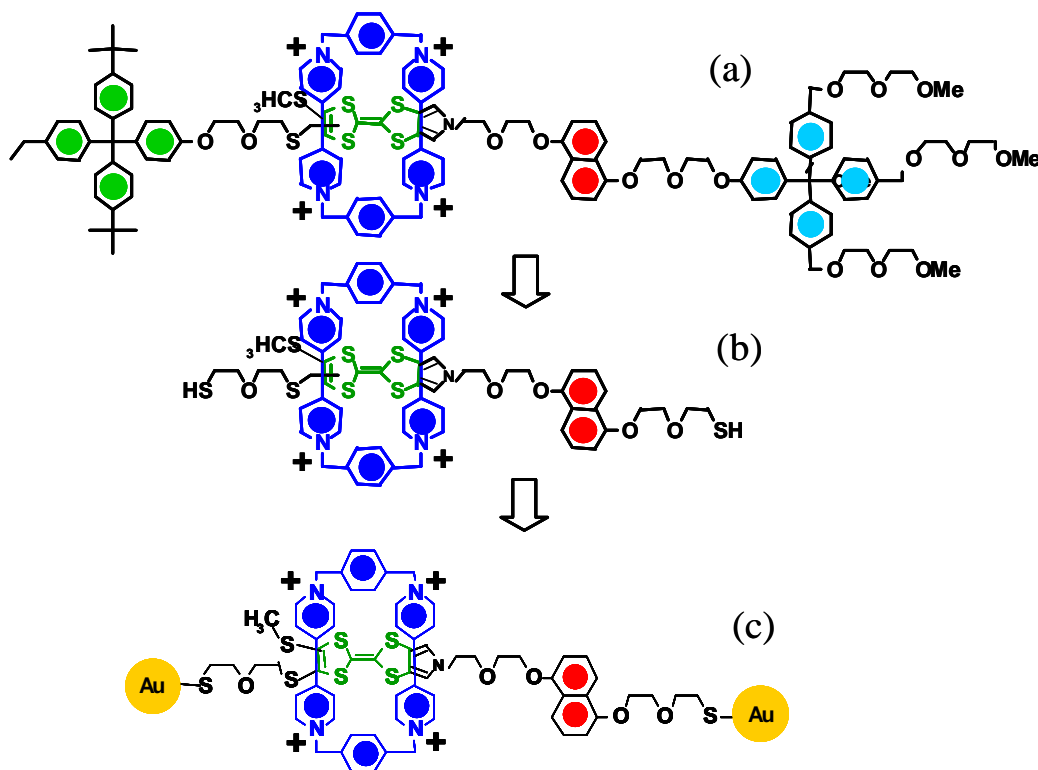


Figure S2. a) The rotaxane used in the experiments. b) The simplified rotaxane used in the calculations. c) The simplified rotaxane attached to a gold particle

Section 2. Implementation of Green's function theory for calculating I-V curves

Generally the current through molecules is expressed as; [12-14]

$$I(V) = \frac{2e}{h} \int_{-\infty}^{\infty} T(E,V)[f_1(E,V_1) - f_2(E,V_2)]dE \quad (1)$$

where f_i is the Fermi-Dirac function for a voltage V_i at electrode i (1 or 2). The transmission function, $T(E,V)$, is the sum of transmission probabilities of all channels available at energy E and is obtained through the Green function of the molecule, G_M , as affected by the electrode contacts.

$$T(E,V) = \text{Trace}[\Gamma_1(V)G_M(E,V)\Gamma_2(V)G_M^+(E,V)] \quad (2)$$

Γ_i describes the coupling at electrode i .

The Green function of the molecule in equation (2), G_M , is calculated from the molecular Hamiltonian, $H_{MM}(V)$, i.e.,

$$G(E) = \begin{bmatrix} g_1^{-1} & -\mathbf{t}_1 & 0 \\ -\mathbf{t}_1^+ & ES_{MM} - H_{MM} & -\mathbf{t}_2^+ \\ 0 & -\mathbf{t}_2 & g_2^{-1} \end{bmatrix} = \begin{bmatrix} G_1 & G_{1M} & G_{12} \\ G_{M1} & G_{MM} & G_{2M} \\ G_{21} & G_{M2} & G_2 \end{bmatrix} \quad (3)$$

The submatrixes G and g represent Green functions when interactions among subsystems are included or excluded, respectively. g_i represents the electrodes and τ_i describe the metal-molecule coupling. H_{MM} and S_{MM} are the Fock and overlap matrices of the isolated molecule, respectively and E is the electron energy. Therefore, solving eq 3 for G_M , we obtain

$$G_M = [ES_{MM} - H_{MM} - \Sigma_1 - \Sigma_2]^{-1} \quad (4)$$

where

$$\Sigma_1 = \mathbf{t}_1^+ g_1 \mathbf{t}_1 \quad \text{and} \quad \Sigma_2 = \mathbf{t}_2^+ g_2 \mathbf{t}_2 \quad (5)$$

where S_i are the self-energy terms coupling between the molecule and the electrodes.

All the needed parameters can be obtained from the Fock and Overlap matrices based on DFT calculations.

$$F = \begin{bmatrix} H_{11} & H_{1M} & H_{12} \\ H_{M1} & H_{MM} & H_{M2} \\ H_{21} & H_{2M} & H_{22} \end{bmatrix} \quad \text{and} \quad S = \begin{bmatrix} S_{11} & S_{1M} & S_{12} \\ S_{M1} & S_{MM} & S_{M2} \\ S_{21} & S_{2M} & S_{22} \end{bmatrix} \quad (6)$$

The metal-molecule coupling term τ_i can be determined by

$$\mathbf{t}_1 = ES_{M1} - H_{M1} \quad \text{and} \quad \mathbf{t}_2 = ES_{M2} - H_{M2} \quad (7)$$

H_{Mi} are the coupling matrix element between electrode and molecules.

The coupling G_i appearing in eq. 2 is given by

$$\Gamma_1 = i[\Sigma_1 - \Sigma_1^+] \quad \text{and} \quad \Gamma_2 = i[\Sigma_2 - \Sigma_2^+] \quad (8)$$

g_i are the surface green function of the electrode. For Au we approximate this as a diagonal matrix with each element proportional to their local density of states.

$$g_i = \begin{bmatrix} g_s & 0 & 0 & \dots \\ 0 & g_p & 0 & \dots \\ 0 & 0 & g_d & \dots \\ \dots & \dots & \dots & \dots \end{bmatrix} \quad (9)$$

Each orbital character s, p, d leads to different contributions, which we write as based on reference 19,

$$g_s = -0.0720\pi i$$

$$g_p = -0.0426\pi i$$

$$g_d = -0.1778\pi i$$

To carry out these calculations we used the modified Huckel-IV2.0 code provided by Supriyo Datta's group based on above equations.

Section 3. Additional Calculation results

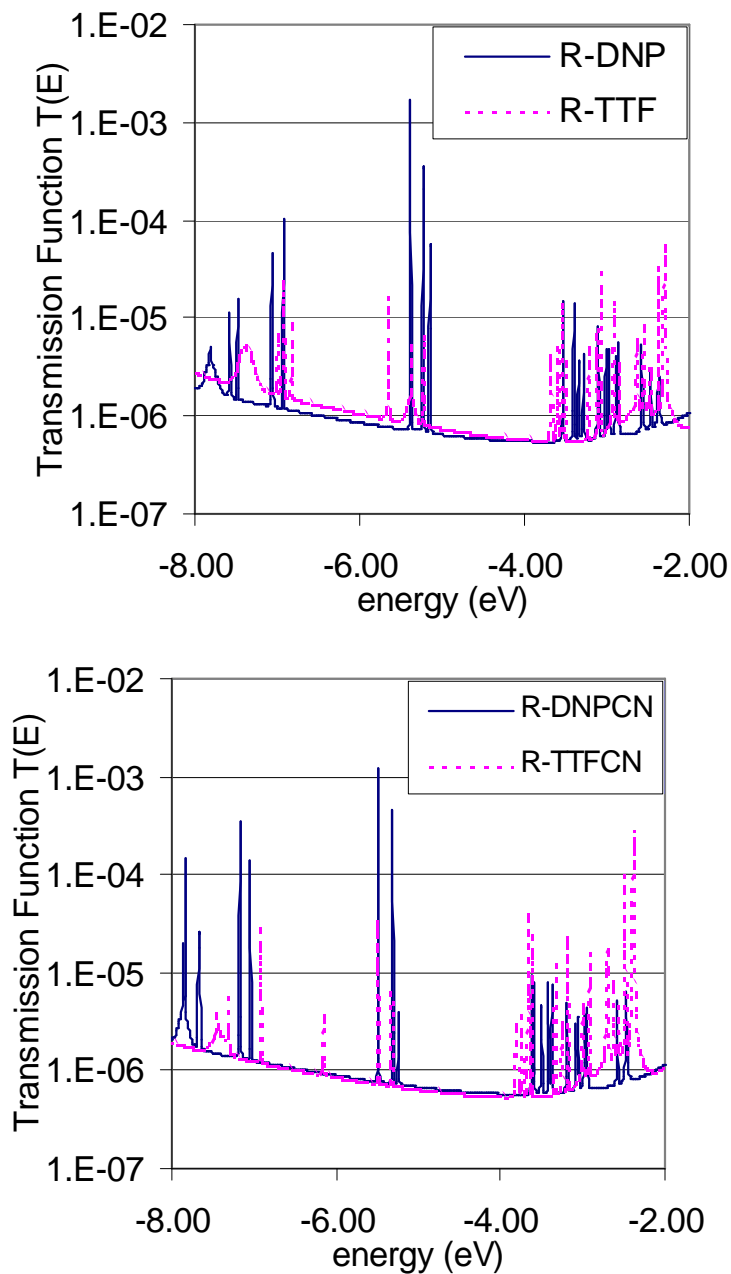


Figure S3. Transmission Function of roxataxane components. (a) R-DNP and R-TTF
(b) R-DNPCN and R-TTFCN

Figure S3 shows the transmission function $T(E)$ calculated from equation (2). Figure S3a compares the ring on the DNP group with the ring on the TTF group. Over the range

between -6.0 to -4.0 eV, the ring on DNP leads to more than 100 times the transmission of ring on TTF. This is because the ring affects the characteristics of MOs.

Figure S3b compares ring on DNP-CN group with ring on the TTF group.

Table S1. The calculated orbital energies (eV) of rotaxane components.

	DNP	TTF	DNPCN	TTFCN
HOMO-2	-5.89	-5.67	-5.86	-6.17
HOMO-1	-5.83	-5.60	-5.84	-6.00
HOMO	-5.38	-5.58	-5.49	-5.56
LUMO	-5.23	-5.38	-5.31	-5.51
LUMO+1	-5.15	-5.23	-5.24	-5.34
LUMO+2	-4.24	-4.97	-4.19	-4.22

Table S1 lists the frontier MOs of DNP, TTF, DNPCN and TTF(CN) components. The characteristics of these MOs are shown in Figure S4, S5, S6 and S7 respectively. The characteristics of those MOs explain the mechanism of the different conductivities, for each switchable state of the rotaxanes.

Figure S4, S5, S6, and S7 show the frontier MOs of R-DNP, R-TTF, R-DNPCN, and R-TTF(CN) respectively.

The HOMO, LUMO and LUMO+1 of R-DNP are all delocalized orbitals.

The HOMO, LUMO, LUMO+1 of R-TTF are localized molecular orbitals.

The HOMO and LUMO of R-DNPCN are delocalized molecular orbitals. Notice that LUMO+1 becomes localized after CN addition. This MO contributes much lower

transmission, as shown in Figure S9. LUMO and LUMO+1 are localized MOs. HOMO and HOMO-1 are localized at Au electrodes.

Figure S8 shows the I-V curves as discussed in the Text. The left I-V curve for DNP-CN shows two flat regions from contributions from two frontier MOs. The right I-V curve shows below 0.1 V DNP has a large slope comparing with the curve after 0.1 V, indicating that two different MOs contribute to this curve. Thus the modification by CN changes the ON/OFF ratio, even though the electronic conductivity does not change significantly. This means that the mechanism of the switch in conductivity is dominated by the shape of the MO instead of its MO energy level.

Figure S9 shows the transmission function of R-DNP, R-TTF, R-DNPCN and R-TTF(CN) respectively. Each MO contributes a different transmission probability.

For R-DNP, the HOMO, LUMO and LUMO+1 are delocalized MOs and thus have 10^{-2} to 10^{-4} transmission probability.

However, the HOMO-2, LUMO and LUMO+1 of R-TTF only have $\sim 10^{-5}$ transmission. The characteristic of the MOs in Figure S6 and Figure S7 clearly show the difference in localization of the MOs. The HOMO and HOMO-1 of R-TTF have small transmission probability because they are both localized Au orbitals. Similarly, the HOMO-1 of R-DNP leads to low transmission probability. The frontier orbitals of the CN modified rotaxane molecules are shown in Figure S3. We see that the LUMO+1 in R-DNP has become the LUMO in R-DNPCN leading to increased delocalization. This leads to improved conductivity.

Figure S10 shows the electric conductivity of R-DNP, R-TTF, R-DNPCN and R-TTFCN respectively. The conductivities of R-TTF and R-TTF(CN) components range

from 0.06 to 0.20 nA/V. In contrast, the conductivities of R-DNP and R-DNPCN range from 1.00 to 9.0 nA/V. The peaks at around 0.2 V of R-DNP are dominated by the HOMO of R-DNP. The peaks at 0.0V and 0.40 V of R-DNPCN conductivities are contributed from LUMO and HOMO of R-DNPCN.

Figure S11 shows the density of states (DOS) of rotaxane molecules. The DOS identifies the position of each MO, but it does not indicate the shape characteristics of the MOs.

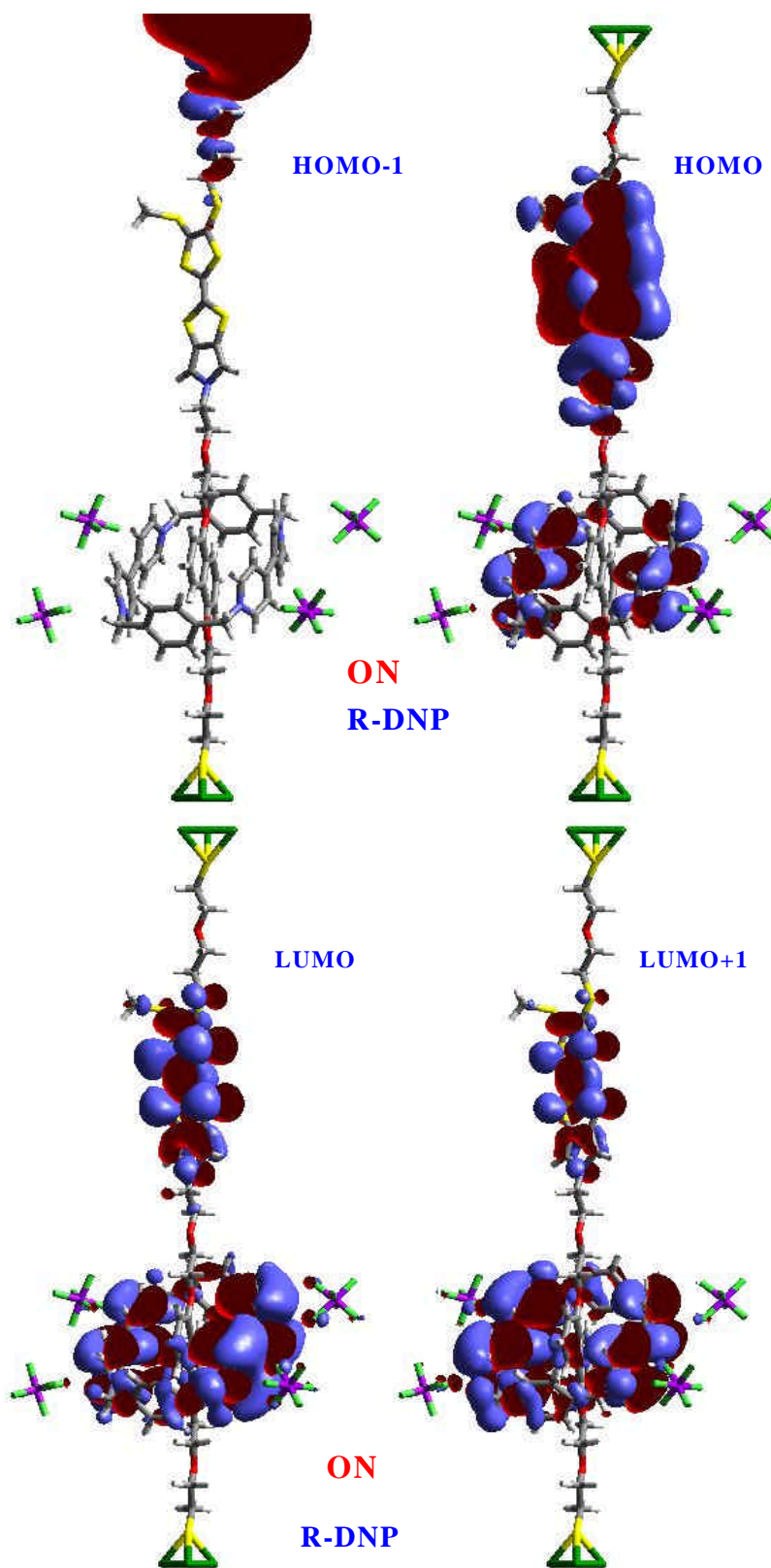


Figure S4. The characteristic MOs of R-DNP.

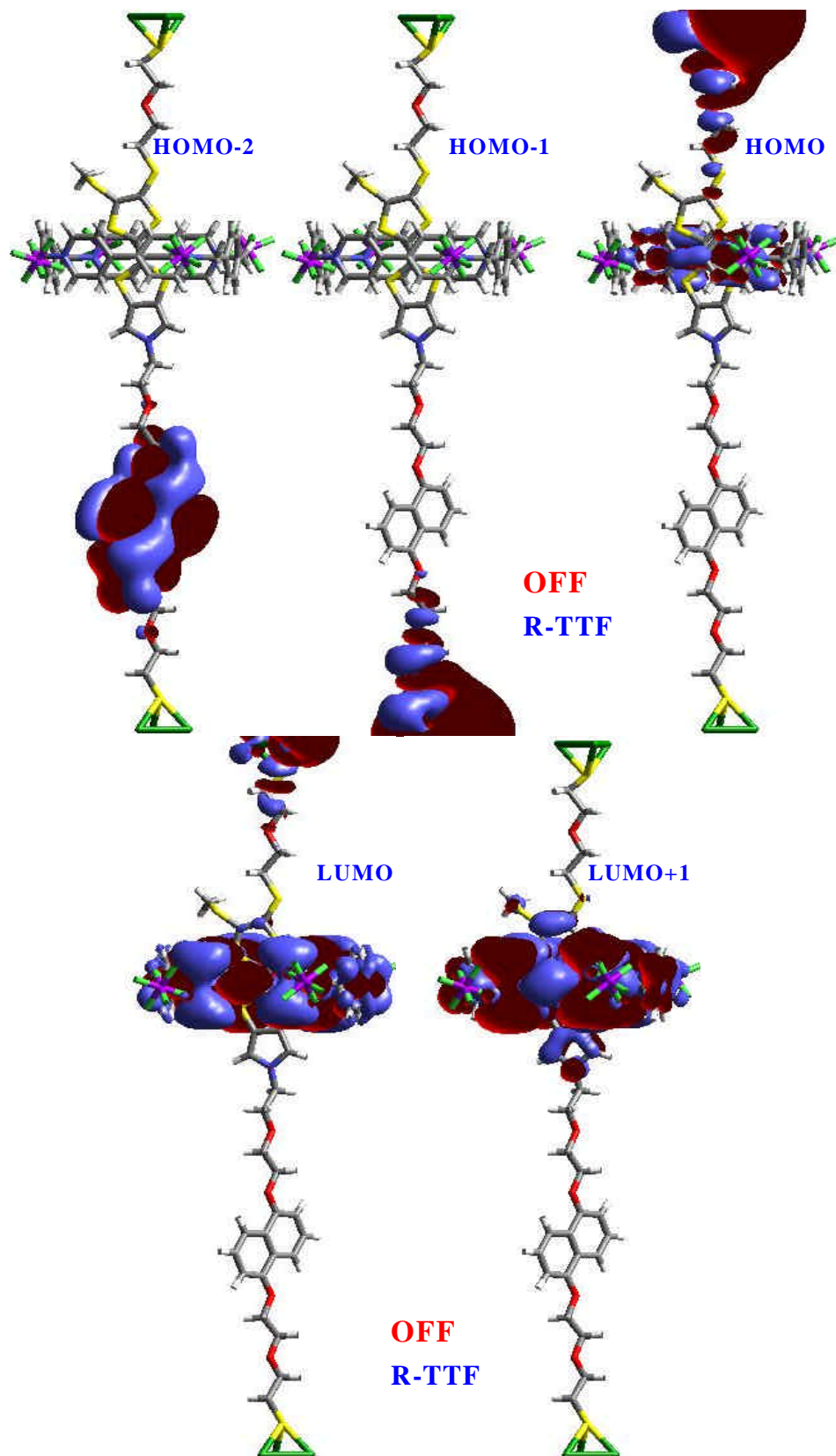


Figure S5. The characteristic MOs of R-TTF.

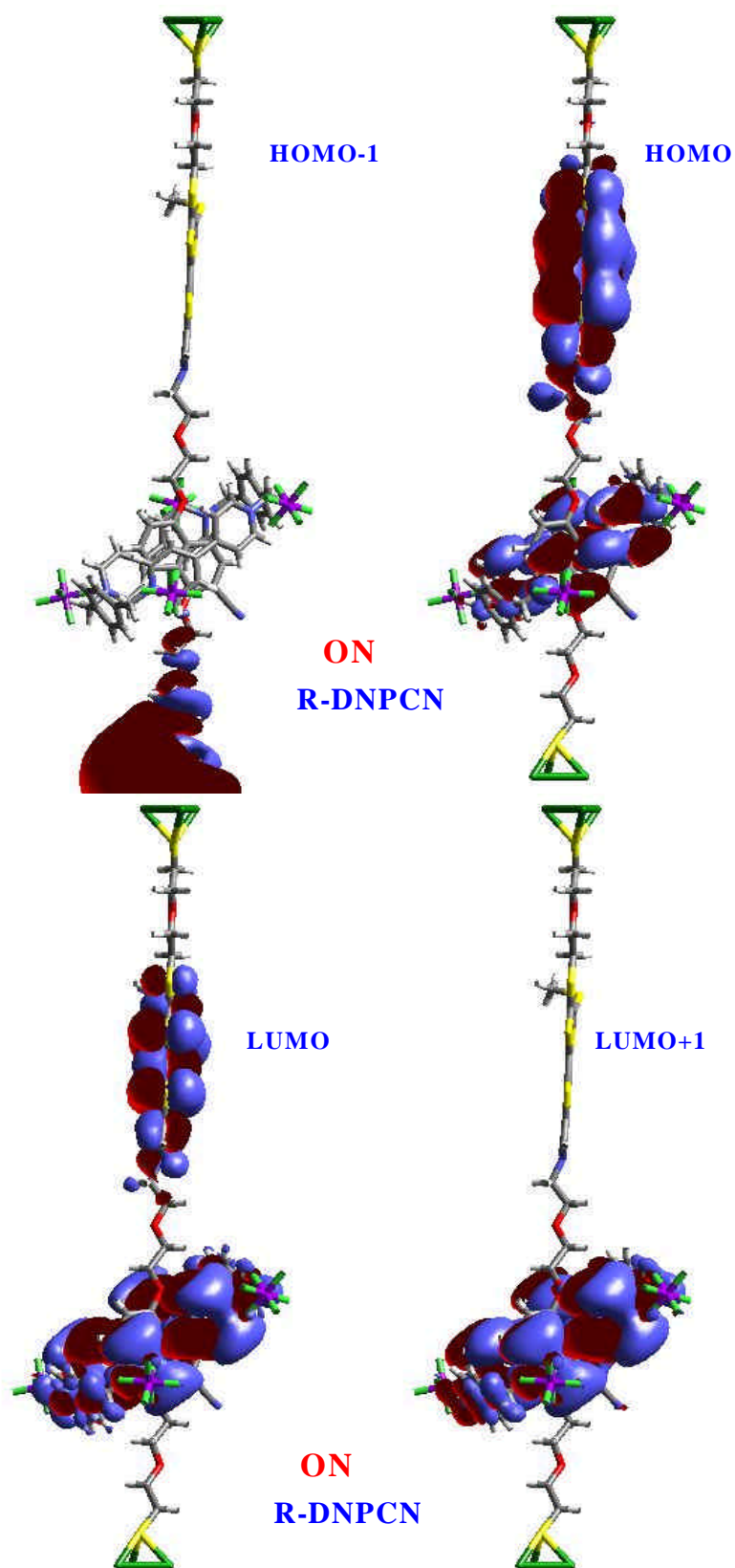


Figure S6. The characteristic MOs of R-DNPCN.

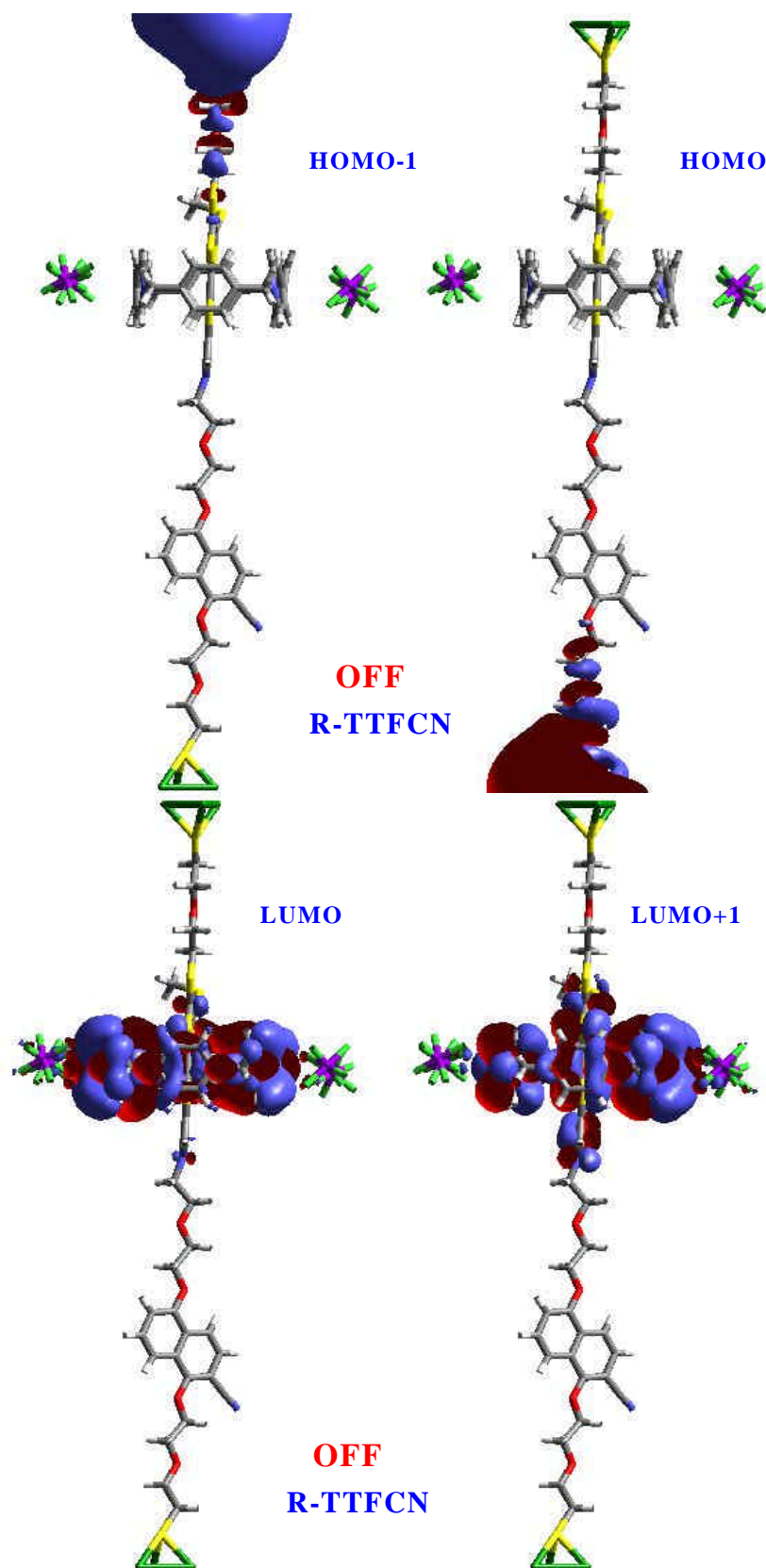


Figure S7. The characteristic MOs of R-TTFCN.

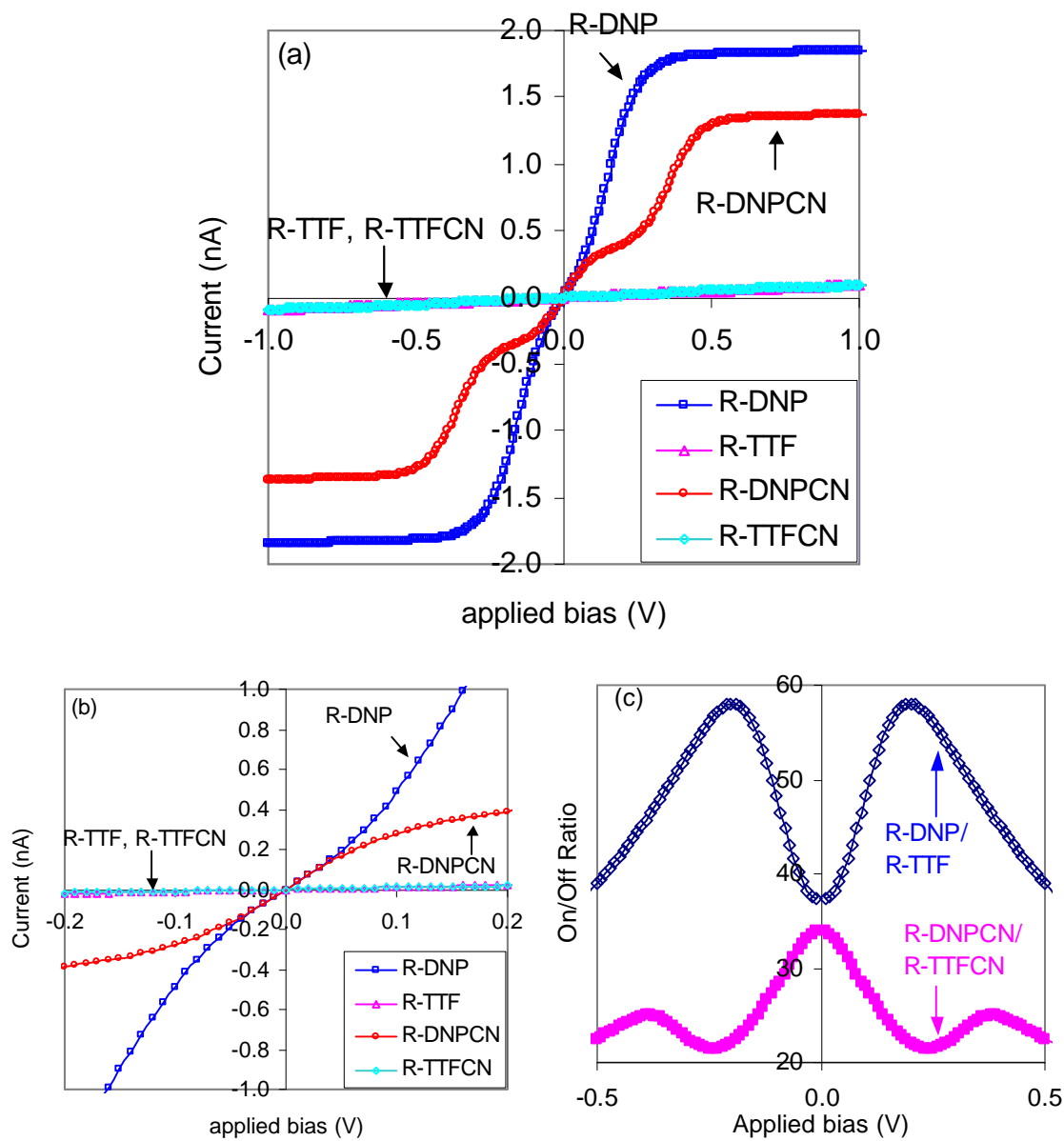


Figure S8. The I-V curves for various rotaxane systems. a). Scaling from 0-1 V bias. b) Scaling from 0-0.2 V bias. c) On/Off ratio of R-DNP/R-TTF and R-DNPCN/R-TTF.

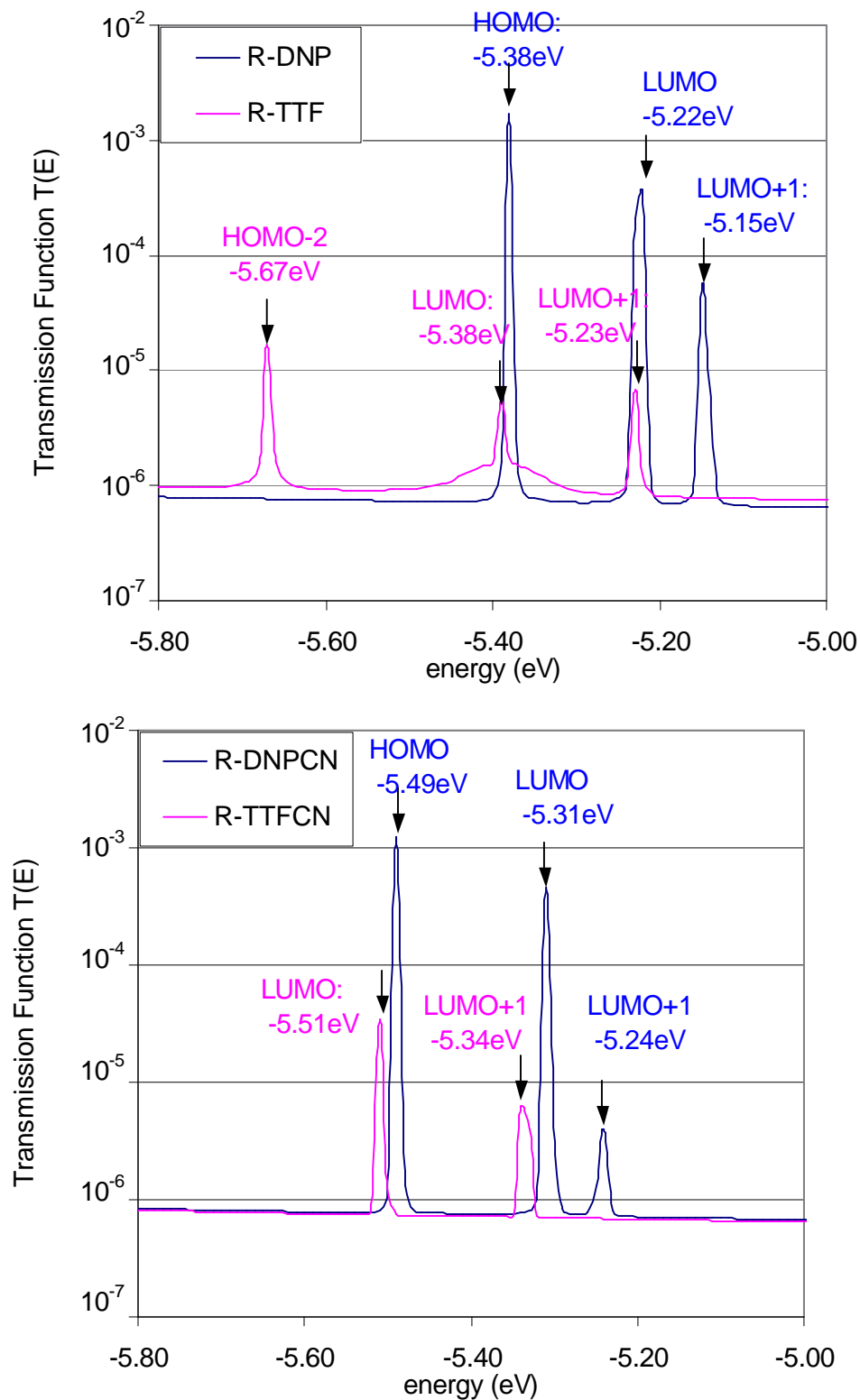


Figure S9. The contribution of each MO to the transmission function $T(E)$.

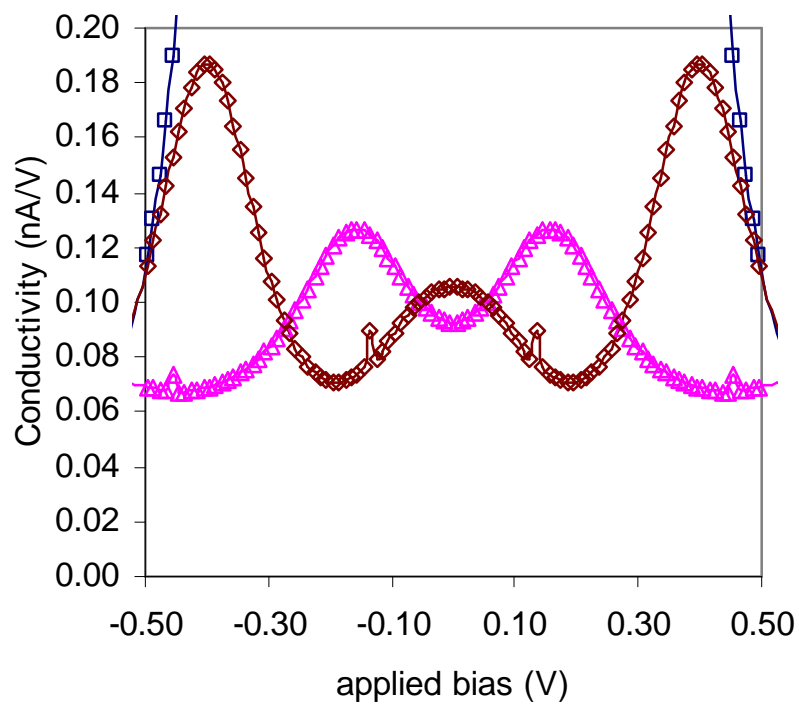
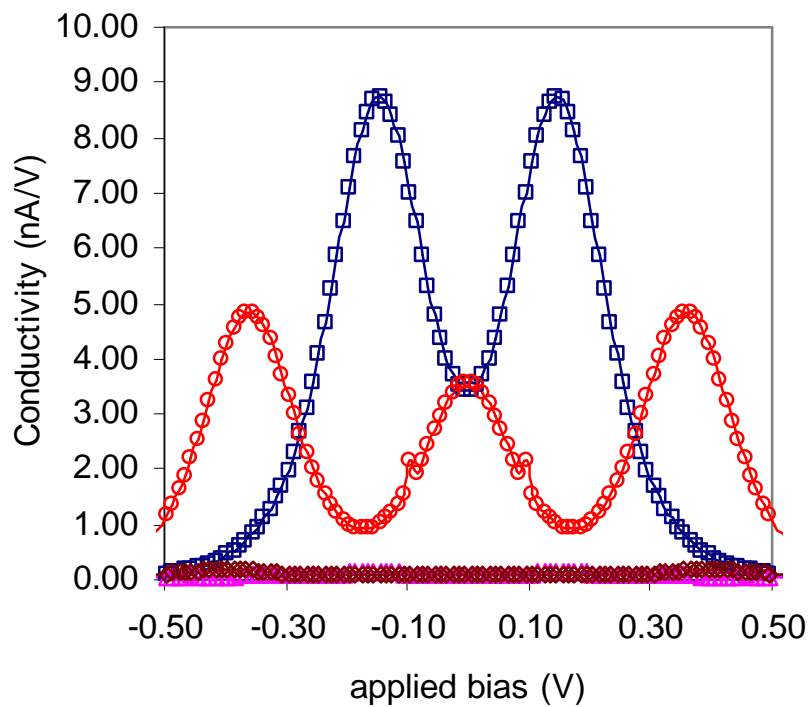


Figure S10. The conductivities of rotaxanes. Blue square is R-DNP, red circle is R-DNPCN. Pink triangle is R-TTF and brown is R-TTF(CN).

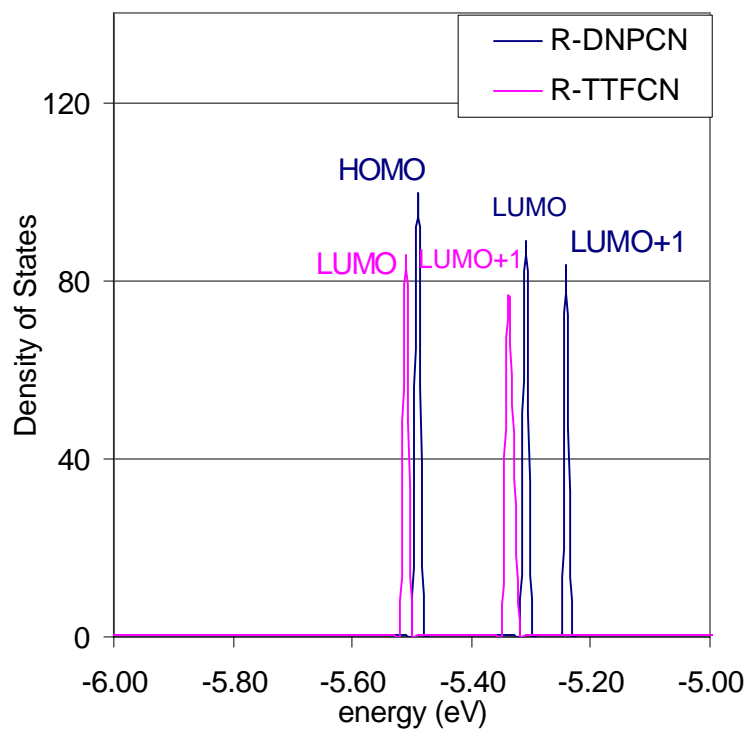
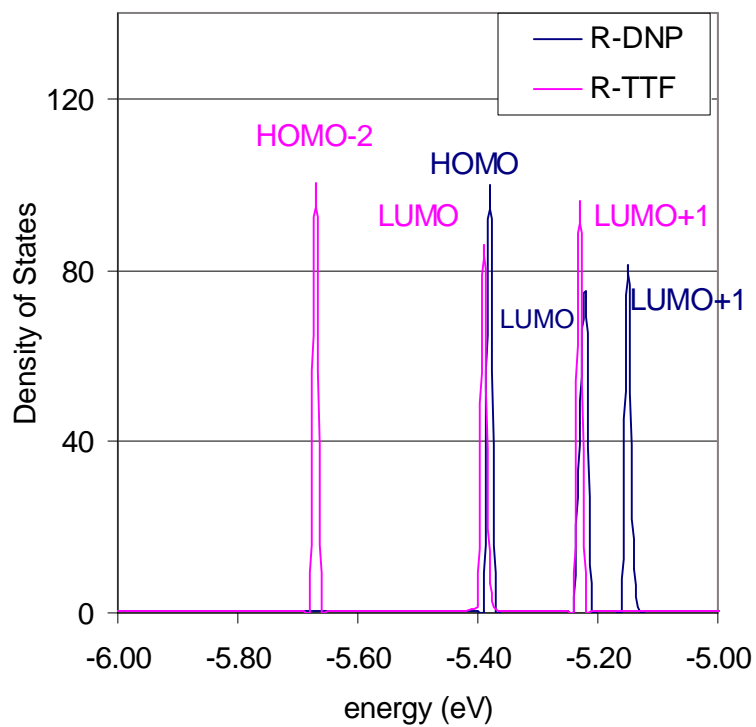


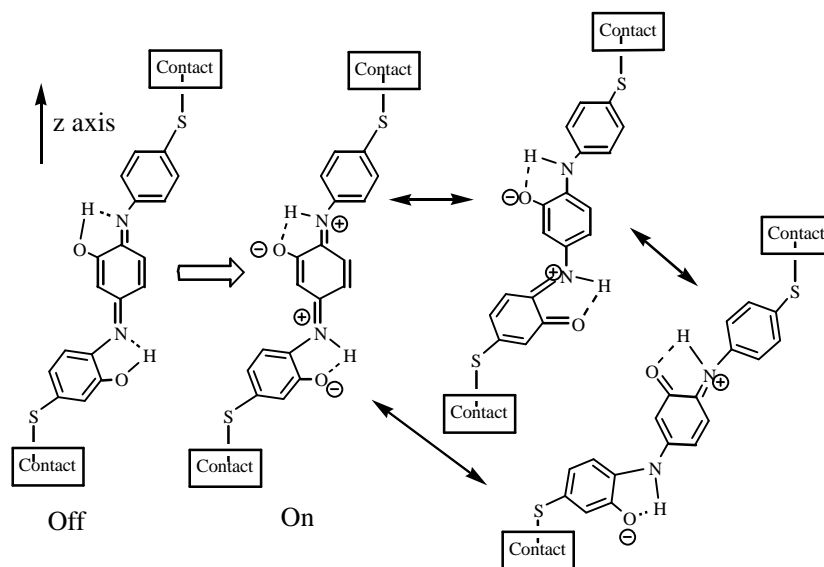
Figure S11. Density of states of frontier MOs for rotaxane molecules.

ULTRAFAST PROTON-HOPPING MOLECULAR SWITCH †

Abstract

We propose the proton-hopping concept for ultrafast switching devices and test the design using a combination of computational approaches. As a specific implementation of a proton-hopping molecular switch, we consider a benzenamine component with two OH groups. Using transition state theory with quantum mechanical energy surfaces we predict that this design will lead to an Off to On switching speed of 3.65 picosecond and an On to Off switching speed of 8.6 picosecond. We find that an electric field of $1\text{V}/\text{\AA}$ is sufficient to switch Off to On. Using Green's function theory we find an On/Off ratio of ~ 5 in the conductivities.

Figure for Table of Contents (ultrafast proton-hopping molecular switch).



† With Xin Xu's assistance at tunneling correction of proton hopping calculations

The use of molecules as the active components of electronic devices was proposed in 1974 [1]. However, it is only until recently that the manufacture of single molecule devices becomes possible with the advances in nanotechnology. Several functionalities and phenomena useful for electronic applications have been demonstrated. These include resonant tunneling, Coulomb blockade and Kondo effect, etc.[2] A molecular switch based on a bistable rotaxane consisting of a ring and a backbone component was proposed and demonstrated,[3-5] where the writing voltage triggered the ring movement along the backbone between two stable states, leading to a dramatic change in the conductivity of the system that can be ascertained under a much smaller reading voltage. Although appealing as a memory device, the response time scale of this switch is too slow, ~ microseconds, limiting its application for ultra-fast process required by information technology for its next generation electronic devices. In this chapter, we discuss a new concept for an ultra-fast molecular switch triggered by proton migration. We designed a model system based this concept and validated it by using first principles calculations.

For a rational design of a molecular switch, two issues have to be considered: an ultra-fast response time scale and a switchable conductivity with changes of voltages. It is well known that proton hopping in aqueous solutions can occur at subpicoseconds or faster;[6-7] and that the conductivity of conducting polymers can change dramatically as a function of pH (On/Off ratio can be up to 10^{11}), implying that proton motion may play an important role in changing electronic conductivity.[8] Therefore, it is possible to design an ultra-fast molecular switch triggered by proton migration.

Scheme 1 shows an example that may satisfy these two criteria. Under an applied field the proton can shift between oxygen and nitrogen atoms. When the proton is on nitrogen atom, the resonant structures allow delocalization of the electrons, leading to a higher conductivity. The proton migration potential is changed by the external electric field along the z axis of the molecule, allowing this voltage to control the On/Off of this switch.

We performed several simulations to validate this proposed concept. We used quantum mechanics (B3LYP/LACVP**) to optimize the bistable molecular structures and the transition states between these local stable states under no external electric field.[9] Single

point calculations are performed on the respective structures with the external electric field being turned on. The proton hopping rate was calculated using transition state theory (TST) based on the quantum mechanic results to estimate the vibrational frequencies and tunneling factors.[10] The electric conductivity was calculated directly from electronic wave functions using a full quantum-mechanical treatment combined with green function theory, as demonstrated by Ratner and Datta et. al.[12-15]

Figure 1 shows the potential energy surface for proton migration between the bistable sites. The Off state has two protons connecting to the oxygen atoms while the On state has both protons connecting to the nitrogen atoms. The Middle state has one proton connecting with the oxygen atom and the other connecting with the nitrogen atom. The blue curve is for zero voltage and the pink curve is the potential energy surface under an applied electric field (1V/Å). We find that this modest voltage is sufficient to change the relative stability of these three locally stable states.

Without an external field, the Off site is 12.01 kcal/mol more stable than the On site. The proton hopping barriers on the pathway are 9.33 kcal/mol from Off to Middle and 6.44 kcal/mol from Middle to On. The corresponding reverse hopping barriers are only 1.72 and 2.04 kcal/mol. After applying an electric field along the molecule axis, the potential energy surface changes. The On site is now 19.21 kcal/mol more stable than the Off state. TS1 presents no barrier from Off to Middle; while the hopping barrier for the second proton from Middle to On is only 1.67 kcal/mol.

The response time is a most important parameter for fast switching applications. The hopping rate can be estimated by using Transition State Theory with tunneling corrections. [10]

$$k = \mathbf{k}(T) \frac{k_B T}{h} \exp\left(-\frac{\Delta G^\ddagger}{RT}\right)$$

where tunneling factor is given by[10-11]

$$k(T) = 1 + \frac{1}{24} \left(\frac{h\nu^\ddagger}{k_B T} \right)^2$$

With the voltage (1V/Å) applied to the molecule, the protons hop from Off to the On state, following the pink curve in Figure 1. The calculated hopping rate is $2.74 \times 10^{11} \text{ s}^{-1}$, corresponding to a 3.65 ps switching speed. This is 10^6 faster than the rotaxane molecular switch. When the voltage is turned off, the switch goes from On to the Off state, as indicated in the blue curve of Figure 1. The calculated switching speed is $\sim 8.60 \text{ ps}$. Therefore; this molecular switch exhibits an ultrafast switching speed needed in many application areas.

Figure 2A shows a prototype for a proton-hopping switch. The self-assembly monolayer forms between two Au thin films. The writing voltage controls proton migration while the reading voltage is used to detect the status of the switch. Our simulations used a simplified device with a dithiolate-benzenamine molecule with additional OH groups placed between the gold electrodes. The electrodes were modeled using clusters with three gold atoms. B3LYP/LACVP**[9] was used to calculate the Fock matrix and overlap matrix. Then Green's function theory was used to calculate the transmission function and current. The current/voltage diagrams for the On and Off states were shown in Figure 2B, from which we see that under 0.5 V bias, the On/Off ratio can reach 5.

Because the coupling between the gold electrodes and the molecules are essentially the same for the On and Off states, this large On/Off ratio can only be attributed to the structural differences due to the proton migration. Since the proton migration is an ultrafast process and can be triggered easily by external electric field, we believe that our mechanism works well as a molecular switching device. There are many ways to improve this prototype design to reduce the writing voltage, to decrease power consumption, and to increase the On/Off conductivity ratio. To increase the ratio of the On/Off conductivity, we may want to change the relative delocalization of the LUMOs of the two states.[16] This might be done by attaching an electron donor to the phenyl group. Another possibility for a larger On/Off ratio is to arrange the system so that it switches between planar and twisted

conjugated structures. We could use the present methodology to screen the choices for these to improve the performance.

Summary, we present a rational design strategy for ultra-fast molecular switches modulated by proton migration. This design was validated with first principles simulations, proving the good performances. Such switches should be useful for achieving the high switching speeds required by information technology for its next generation electronics.

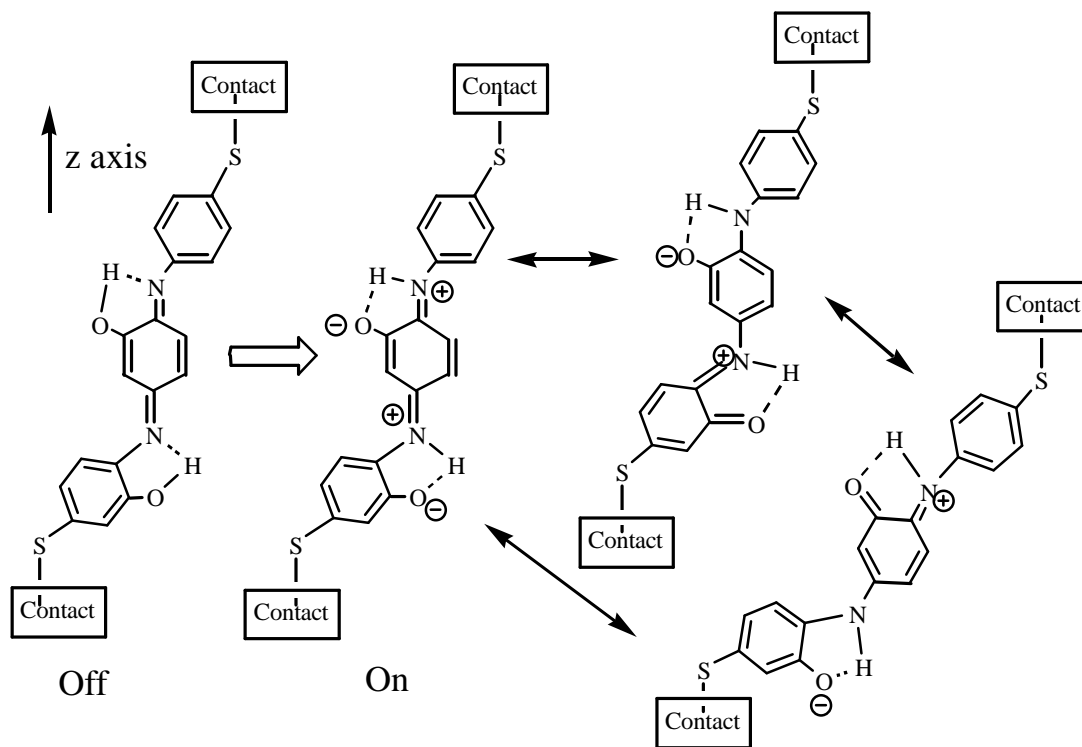
ACKNOWLEDGMENT We thank Fraser Stoddart at UCLA for helpful discussions. This research was supported by the MARCO project at UCLA.

Reference

1. Aviram, A.; Ratner, M. A. *Chem. Phys. Lett.* 1974, 29, 277.
2. Aviram A.; Ratner, M.A. and Mujica, V. *Molecular Electronics II* NY Academy of Sciences, New York, 2002.
3. Collier C.P.; Wong E.W.; Belohradsky M.; Raymo F.M.; Stoddart J.F.; Kuekes P.J.; Williams R.S.; Heath J.R., *Science* 1999, 285, 391.
4. Collier C.P.; Jeppesen J.O.; Luo Y.; Perkins J.; Wong E.W.; Heath J.R.; Stoddart J.F.; J. *Am. Chem. Soc.* 2001, 123, 12632.
5. Luo Y., Collier C. P., Jeppesen, J. O., Nielsen K. A., Delonno, E. and et. al *Chemphyschem* 2002, 3, 519
6. Mauerhofer, E. and Roßsch, F. *Phys. Chem. Chem. Phys.*, 2003, 5, 117–126. 0.69ps reported.
7. Horsewill, J.; Jones, N. H. and Caciuffo, R. *Science* 2000, 291, 100
8. Miller, L.L.; Bankers, J. S.; Schmidt, A. J. and Boyd, D. C. J. *Phys. Org. Chem.* 2000; 13, 808–815.

9. The quantum calculations are performed by using Jaguar 5.0, from Schodinger Inc., Portland, Oregon.
10. Gonzalez, C. A.; Allison, T. C. and Louis, F.; J. Phys. Chem. A 2001, 105, 11034-11040.
11. Damle, P.; Ghosh, A.W. and Datta, S. Chem. Phys. 2002,281, 171–187
12. Datta, S. Electronic Transport in Mesoscopic Physics; Oxford University Press: Oxford, 1997.
13. Mujica, V.; Kemp, M.; Ratner, M.A. J. Chem. Phys. 1994, 101, 6849
14. Xue, Y.Q.; Datta S.; Ratner, M.A. J. Chem. Phys. 2001, 115, 4292
15. Seeing supporting materials, which include structural information, energetics, calculation method and details.

Scheme 1. Design strategy for proton-induced molecular switch. Proton hopping from Oxygen to Nitrogen under electric field leads to the change of conductivity. The product structure involves resonance among three valence structures.



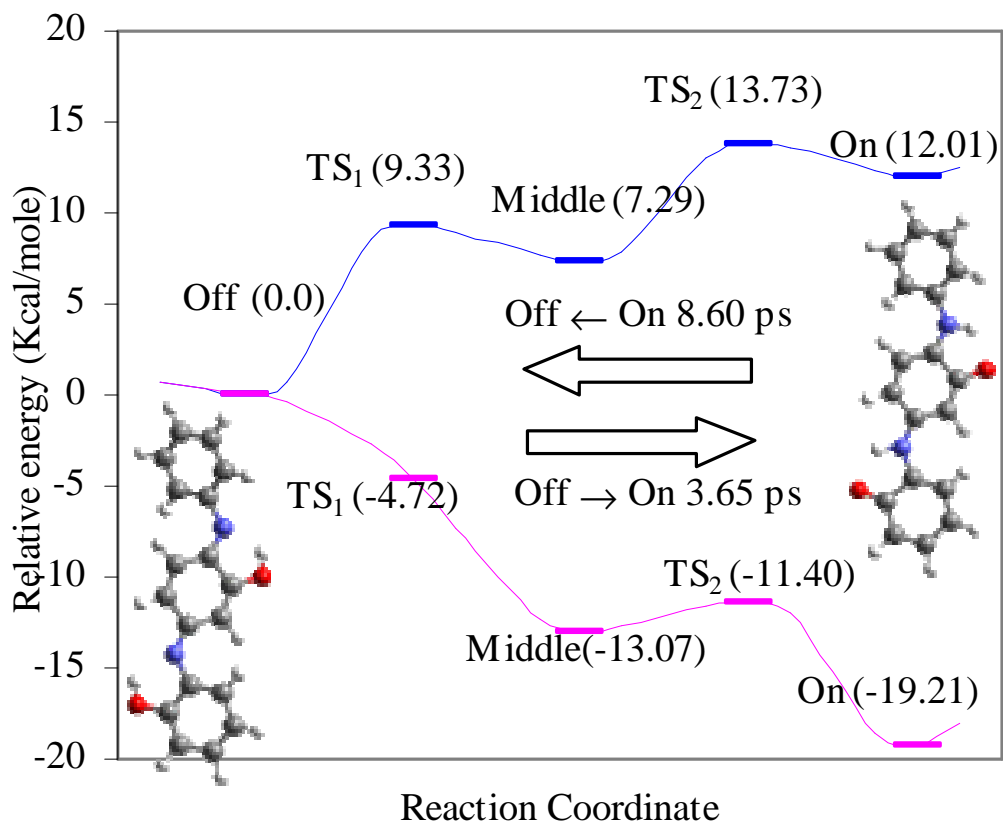


Figure 1. The potential energy surface for the proton-hopping switch as a function of external field. The blue curve is the proton hopping energy surface without external field and pink curve is the proton hopping energy surface with $1\text{V}/\text{\AA}$ (15.0 V) across the molecule). The switching speed is calculated by transition state theory.

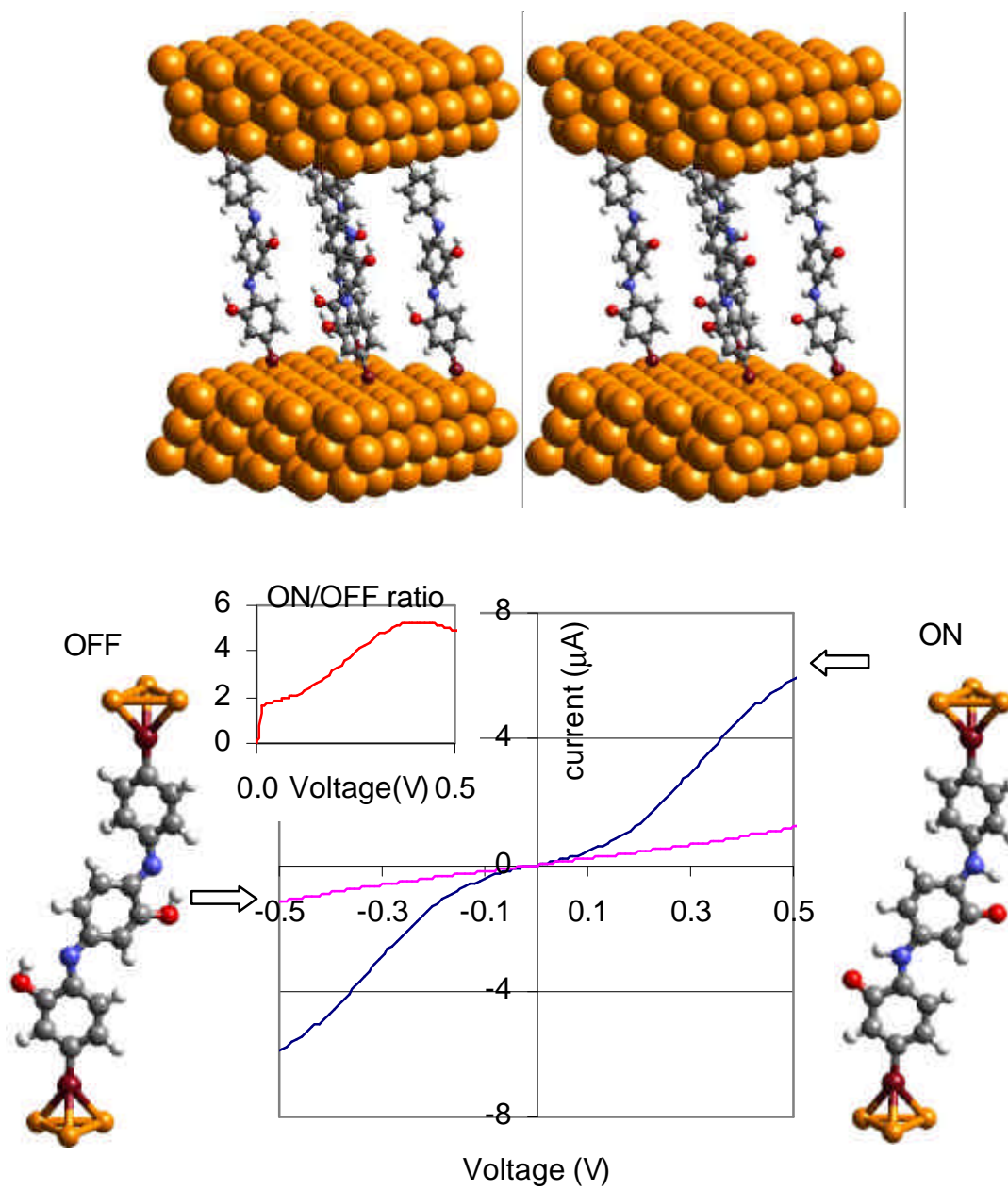


Figure 2. A) Diagram for the proton-hopping switch SAM. B) I-V curve of proton switch for ON and OFF states. The read voltage is along the abscissa.

Support information:

Ultrafast proton-hopping molecular switch

Abstract

We organize this supportive information into three sections. Section 1 describes the structural information and energetics; Section 2 describes the estimation method of proton hopping speed; Section 3 describes the Green Function Theory to estimate the I-V characteristic of such device.

Section 1. Optimized structural information and energetics of proposed structures.

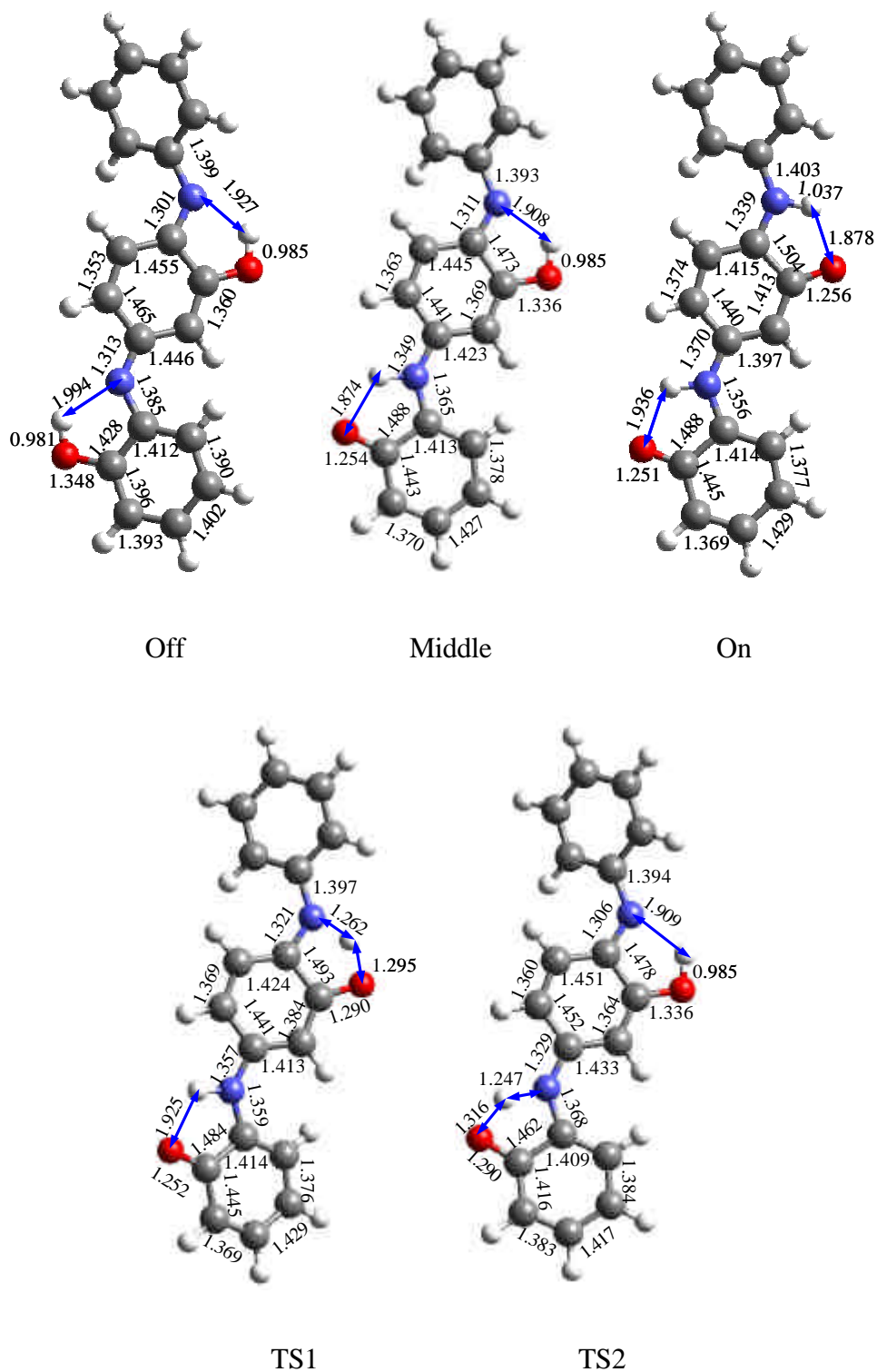


Figure 1. The optimized structures at B3LYP/6-31G**.

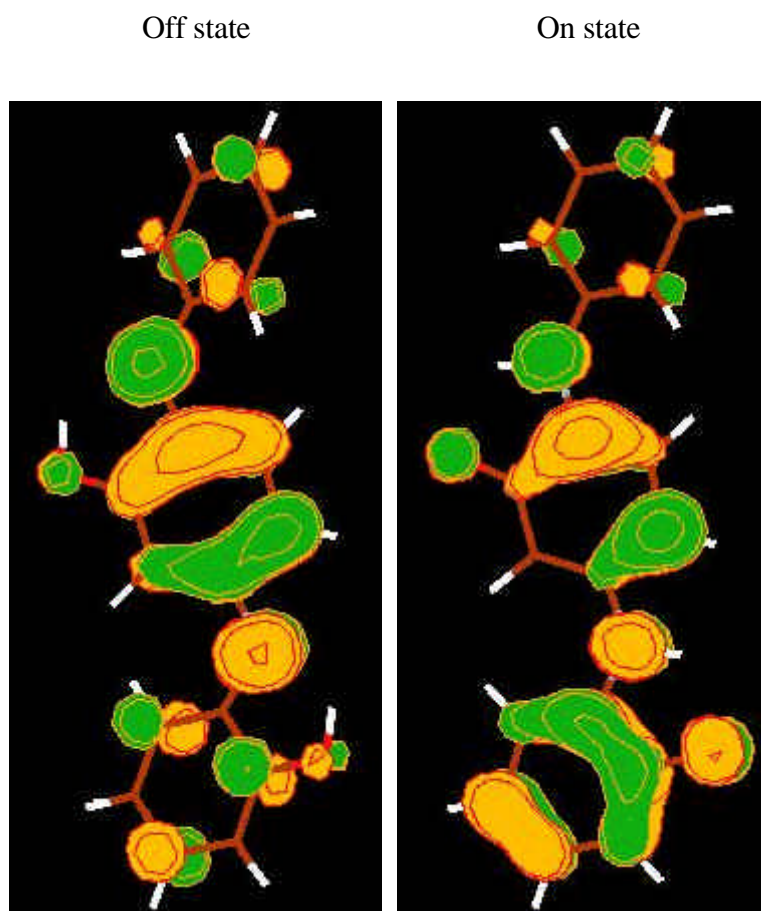


Figure 2. The LUMO of Off and On state of molecules. Slight different localizations at the bottom phenyl ring lead to different conductivity. A proper additional group on such group should improve the On/Off ratio of conductivity.

Table 1. The energetic of quantum mechanics results.

	Off(H-O)	TS ₁	Middle	TS ₂	On(H-N)
Energy E ⁰ (under zero field) (Hartree)	-954.2940	-954.2748	-954.2833	-954.2691	-954.2787
ZPE (kcal/mole)	184.894	182.146	185.449	182.965	187.321
Relative energy ΔE ⁰ without field (kcal/mole)	0	9.330	7.287	13.730	12.009
Gibbs Free Energy G (kcal/mole)	-28.360	-28.262	-28.513	-28.219	-28.252
Imaginary Frequency of TS (cm ⁻¹)		-2105.36		-1836.69	
Energy E ^f (under 1V/Å field) (Hartree)	-954.4452	-954.4483	-954.4669	-954.4603	-954.4797
Relative energy ΔE ^f under field (kcal/mole)	0	-4.717	-13.073	-11.402	-19.214

*Energetic of structures above under external field (0.02 atomic unit along z axis) are performed by single point calculations.

Section 2. The estimation of Proton hopping rate constant

The proton hopping rate constant is calculated by $k = \kappa(T) \frac{k_B T}{h} \exp\left(-\frac{\Delta G^\ddagger}{RT}\right)$

Where $\kappa(T)$ is the tunneling effect determined by $\kappa(T) = 1 + \frac{1}{24} \left(\frac{h\nu^\ddagger}{k_B T}\right)^2$ k_B is Boltzmann constant, h is plank constant and ν^\ddagger is imaginary frequency of TS.

The ΔG^\ddagger without field is calculated by $\Delta G^\ddagger_{ij} = E_i^0 + G_i + ZPE_i - E_j^0 - G_j - ZPE_j$ where E^0 is the energy without field, G is the Gibbs free energy and ZPE is zero point energy. Those parameters are listed in Table 1.

The ΔG^\ddagger under field is calculated by $\Delta G^\ddagger_{ij} = E_i^f + G_i + ZPE_i - E_j^f - G_j - ZPE_j$ where E^f is the energy under field. Here we assume the electric field does not change the vibrational frequencies of molecules and TSs.

Table 2. The parameters for calculate rate constant of each step

	TS	ΔG^\ddagger (kcal/mole)	Freq (cm^{-1})	Tunneling effect	Rate constant (s^{-1})	Hopping speed (ps)
Under 1V/Å field						
Off → Middle	TS ₁ *	-4.620	-2105.36	—	—	—
Middle → On	TS ₂	1.965	-1836.69	1.184	2.74×10^{11}	3.65
Without field						
On → Middle	TS ₂	1.753	-1836.69	1.184	3.91×10^{11}	2.56
Middle → Off	TS ₁	2.294	-2105.36	1.242	1.65×10^{11}	6.04

* The TS₁ under electric field is not a real Transition State anymore. Thus we did not calculate the hop rate of Off. → Middle under electric field. The data is listed there for comparison.

Section 3. IV characteristic calculated by Green Function theory

Generally the current through molecules at is expressed as:[11-14]

$$I(V) = \frac{2e}{h} \int_{-\infty}^{\infty} T(E,V)[f_1(E,V_1) - f_2(E,V_2)]dE \quad (1)$$

where f_i is the Fermi-Dirac function for a voltage V_i at electrode i (1 or 2). The transmission function, $T(E,V)$, is the sum of transmission probabilities of all channels available at energy E and is obtained through the Green function of molecule, G_M , affected by electrode contacts.

$$T(E,V) = \text{Trace}[\Gamma_1(V)G_M(E,V)\Gamma_2(V)G_M^+(E,V)] \quad (2)$$

Γ_i describes the coupling at electrode i .

The Green function of molecule in equation (2), G_M , will be calculated from the molecular Hamiltonian, $H_{MM}(V)$, i.e.,

$$G(E) = \begin{bmatrix} g_1^{-1} & -\mathbf{t}_1 & 0 \\ -\mathbf{t}_1^+ & ES_{MM} - H_{MM} & -\mathbf{t}_2^+ \\ 0 & -\mathbf{t}_2 & g_2^{-1} \end{bmatrix} = \begin{bmatrix} G_1 & G_{1M} & G_{12} \\ G_{M1} & G_{MM} & G_{2M} \\ G_{21} & G_{M2} & G_2 \end{bmatrix} \quad (3)$$

The submatrixes G and g represent Green functions when interactions among subsystems are included or excluded, respectively. g_i represents the electrodes and \mathbf{t}_i describe the metal-molecule coupling. H_{MM} and S_{MM} are the Fock and overlap matrices of the isolated molecule, respectively and E is the electron energy. Therefore, solving eq 3 for G_M , we obtain

$$G_M = [ES_{MM} - H_{MM} - \Sigma_1 - \Sigma_2]^{-1} \quad (4)$$

where

$$\Sigma_1 = \mathbf{t}_1^\dagger g_1 \mathbf{t}_1 \quad \text{and} \quad \Sigma_2 = \mathbf{t}_2^\dagger g_2 \mathbf{t}_2 \quad (5)$$

where Σ_i are the self-energy terms coupling between the molecule and the electrodes.

All the needed parameters can be obtained from the Fock and Overlap matrices based on DFT calculations.

$$F = \begin{bmatrix} H_{11} & H_{1M} & H_{12} \\ H_{M1} & H_{MM} & H_{M2} \\ H_{21} & H_{2M} & H_{22} \end{bmatrix} \quad \text{and} \quad S = \begin{bmatrix} S_{11} & S_{1M} & S_{12} \\ S_{M1} & S_{MM} & S_{M2} \\ S_{21} & S_{2M} & S_{22} \end{bmatrix} \quad (6)$$

The metal-molecule coupling term τ_i can be determined by

$$\mathbf{t}_1 = ES_{M1} - H_{M1} \quad \text{and} \quad \mathbf{t}_2 = ES_{M2} - H_{M2} \quad (7)$$

H_{Mi} are the coupling matrix element between electrode and molecules.

The coupling Γ_i appeared eq. 2 is given by

$$\Gamma_1 = i[\Sigma_1 - \Sigma_1^\dagger] \quad \text{and} \quad \Gamma_2 = i[\Sigma_2 - \Sigma_2^\dagger] \quad (8)$$

g_i are surface green function of electrode. For Au it can be approximated as a diagonal matrix with each element proportional to their local density of states.

$$g_i = \begin{bmatrix} g_s & 0 & 0 & \dots \\ 0 & g_p & 0 & \dots \\ 0 & 0 & g_d & \dots \\ \dots & \dots & \dots & \dots \end{bmatrix} \quad (9)$$

Different orbital characters such as s, p, d have different contribution, based on Papaopoulos' "Handbook of the Band Structure", we can write them as

$$g_s = -0.0720\pi i$$

$$g_p = -0.0426\pi i$$

$$g_d = -0.1778\pi i$$

The program referred Huckel-IV2.0 code provided by Supriyo Datta's group.

Conductivity G is define by: $G = dI / dV$

Figure 3 shows the calculated conductivity. For On state, the peak at 0.3 V responds to the contribution of HOMO of the molecules.

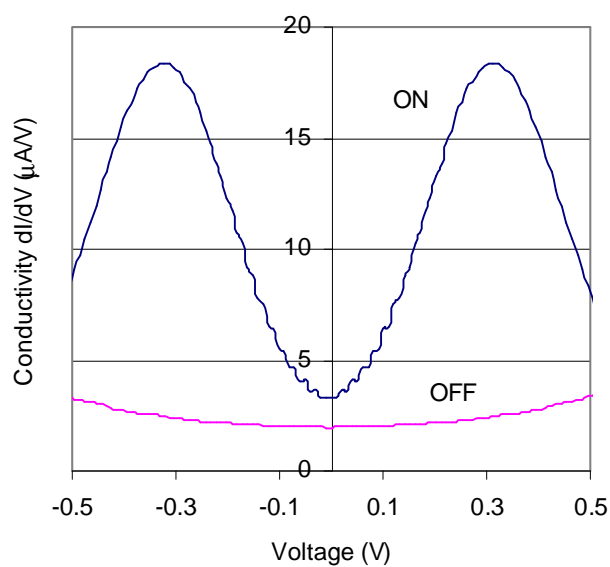
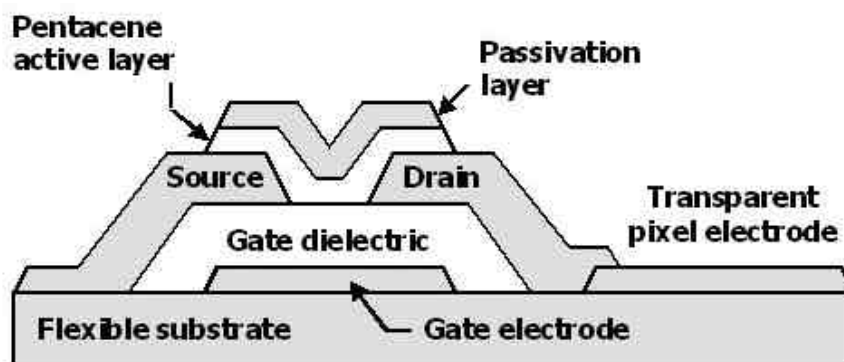


Figure 3 Conductivity vs Voltage.

*Chapter IV***PREDICTIONS OF HOLE MOBILITIES IN OLIGOACENE ORGANIC SEMICONDUCTORS FROM QUANTUM MECHANICAL CALCULATIONS****Abstract**

We estimate the hole mobility for oligoacene crystals using quantum mechanics (QM) to calculate the reorganization energy and electron transfer coupling matrix elements and molecular dynamics (MD) to do the thermal averaging. Using an incoherent transport model we calculate a hole mobility of $6.5 \text{ cm}^2/\text{Vs}$ for pentacene crystals at 300K. This can be compared to recent experimental results of $5 \text{ cm}^2/\text{Vs}$. However we find that an alternative packing into the crystal could lead to a hole mobility of $15.2 \text{ cm}^2/\text{Vs}$. This suggests that current materials might still be improved by a factor of ~ 3 . Such calculations might be useful for finding solid state structures that would increase the hole mobility for use in high performance molecular devices.

Figure for Table of Contents (Pentacene as semiconductor layer in the flexible transistor)



IV-1. Introduction

There is a great deal of interest in developing materials suitable for cheap, flexible electronic devices (e.g., Smart Card, flexible displays). A critical problem here is achieving the $\sim 10 \text{ cm}^2/\text{Vs}$ hole mobility required for integrated circuits based on organics. [4] Amorphous Si is sufficient but too expensive. Organic semiconductors could ultimately be cheap enough, but the mobilities are low ($10^{-2} \text{ cm}^2/\text{Vs}$ for amorphous pentacene and up to $5 \text{ cm}^2/\text{Vs}$ in thin films) [1,-3]. Moreover, many display and memory applications require much faster devices and hence higher mobilities. This raises the question of whether additional modifications in the engineering design of organic semiconductors could improve performance by the factors required [3].

In order to investigate this issue we developed a quantum mechanical (QM) protocol to estimate the mobilities for organic crystals as a function of temperature and pressure and applied it to four oligoacenes (pentacene, tetracene, anthracene, and naphthalene) with structures shown in Figure 1. Our estimates suggest that for the bulk crystal the limiting mobility at 300K is $\sim 6.5 \text{ cm}^2/\text{Vs}$ for atmospheric pressure, indicating that the current materials are close to the optimum. We suggest that these approaches to computational estimates may be useful for virtual screening to find new lead materials likely to provide the improved properties required for increased transport efficiency (for increased device speed), reduced power and avoidance of excessive heating in the promising new applications.

Section IV-2 describes the theoretical methodology, including calculations of reorganization energy, coupling matrix elements, and the incoherent transport model. Section IV-3 discusses the results calculated for the four oligoacenes. The conclusions are presented in Sec. IV-4.

IV-2. Theoretical Methodology

The charge carrier mobility provides the figure of merit for applications of organics in electronic devices. For p-type oligoacene derivatives the conductivity is dominated by transport of positive charges (holes) with mobilities (μ) in the range 10^{-2} – $10 \text{ cm}^2/\text{Vs}$

reported for the thin film and crystalline phases of pentacene.[1-4] Unfortunately there remain conflicts between experimental measurements [6,7], making it essential to develop a solid theoretical basis for understanding the mechanisms dominating hole mobility.

Electronic band structure calculations have previously been used to predict charge transport in perfect crystals of pentacene. Cheng *et al* carried out band calculations for oligoacenes, which assuming a coherent model they used to predict thermal-averaged velocity–velocity tensors. Comparing these tensors to recent experimental data they concluded that the simple band model is unable to explain the temperature dependence of the charge carrier mobility in oligoacene crystal systems for temperatures higher than 150 K. [5] This suggests that dynamic structure disorder may invalidate the band transport model for temperature above 150K suggesting that hopping may be the dominant mechanism at room temperature.

Structural disorder decreases the charge carrier mobility, giving rise to photocurrent transients and frequency dependence in the charge carrier mobility. The disorder leads to a non-periodic structure that may cause the transport mechanism to switch from band-like transport at low temperature (little disorder) to a hopping mechanism at higher temperature. Here structural fluctuations resulting from twisting and sliding of the molecules could play a prominent role.

In order to obtain quantitative insight into the role of structural disorder on the mobility of charge carriers in pentacene, we use an incoherent hopping model to describe the hole mobilities of oligoacenes at room or higher temperatures. Our aims are

- to provide a simple way to predict accurate values of the coupling matrix elements and reorganization energies involved in hole transport and
- to obtain a dynamical model useful for predicting absolute hole mobilities based on first principles results.

Incoherent and partially coherent processes including effects of dynamic or static structural fluctuations have been used to estimate hole mobilities in liquid crystals.[8,9] However, such approaches have not been applied to oligoacene systems.

2.1. Transport properties

To describe charge transport in oligoacenes, we consider an incoherent hopping model in which charge can transfer only between adjacent molecules. A similar approach was used successfully to describe the conduction properties of Organic Superconductors.[27]

Figure 2 shows the several different types of dimers in the pentacene crystal:

- Transverse dimers at distances of $T_1 = 4.75 \text{ \AA}$ (two) and $T_2 = 5.25 \text{ \AA}$ (two)
- Parallel dimers at distance of $P = 6.253 \text{ \AA}$ (two)
- Longitudinal dimers at $L = 14.51 \text{ \AA}$ (two).

Viewing each hopping event as a nonadiabatic electron-transfer reaction, we use standard Marcus theory to express the rate of charge motion between neighboring molecules, W , in terms of the reorganization energy λ and the coupling matrix element V . Assuming that the temperature is sufficiently high that vibrational modes can be treated classically, we obtain [10]

$$W = \frac{V^2}{\hbar} \left(\frac{\mathbf{p}}{Ik_B T} \right)^{1/2} \exp\left(-\frac{\mathbf{l}}{4k_B T} \right) \quad (1)$$

where k_B is the Boltzmann constant and T is the temperature. Given the hopping rate between two neighbors, the diffusion coefficient can be evaluated from the hopping rates as

$$D = \frac{1}{2n} \sum_i r^2 W_i P_i \quad (2)$$

where $n = 3$ is the dimensionality, W_i is the hopping rate due to charge carrier to the i th neighbor, r_i is the distance to neighbor i , P is the relative probability for charge carrier to a particular i th neighbor,

$$P_i = W_i / \sum_i W_i \quad (3)$$

Summing over all possible hops leads to the diffusion coefficient in equation (2). The drift mobility of hopping, μ , is then evaluated from the Einstein relation,

$$\mathbf{m} = \frac{e}{k_B T} D \quad (4)$$

where e is the electronic charge.

Considering now the structural disorder present at higher temperature, the coupling matrix element V becomes a function of distance between two adjacent molecules, leading to

$$W(r) = \frac{V(r)^2}{\hbar} \left(\frac{\mathbf{p}}{\mathbf{1}k_B T} \right)^{1/2} \exp\left(-\frac{\mathbf{1}}{4k_B T} \right) \quad (5)$$

Here we neglect the angular changes between the dimers. The relative probability in equation (3) becomes

$$P(r) = N(r)W(r) / \int_0^{\infty} N(r)W(r)dr \quad (6)$$

where the $N(r)$ is the number of near neighbors at r

$$N(r) = \mathbf{r}g(r)4\mathbf{p}r^2 dr \quad (7)$$

and $g(r)$ is the probability density of having this type of neighbor at a distance r .

The resulting diffusion coefficient becomes

$$D = \frac{1}{2n} \int_0^r r^2 W(r) P(r) dr \quad (8)$$

The hole mobility is still be evaluated by equation (4)

2.2 Reorganization energy I

Assuming that the “hole-containing” (charged) molecule M is at its equilibrium geometry, M_e^+ , and that the neutral molecule P is at its equilibrium geometry, P_e then after the charge transfer the now neutral molecule would relax to the equilibrium geometry M_e while the now charged molecule would relax to P_e^+ . This *reorganization energy* [11], λ , can be partitioned into two parts:

- *fast changes* due to relaxation in the molecular geometry (*inner sphere* contribution) and
- *slow changes* due to repolarization of the surrounding solvent medium (*outer sphere* contribution).

We will neglect the outer sphere contributions to focus on the structural differences between the equilibrium configurations of π -conjugated units. [12] We expect to provide absolute values of hole mobility in such system that can catch the major contributions and be comparable to experimental measurement.

Figure 3 illustrates the calculation of the reorganization energy. For each oligoacene molecule, the geometry was optimized using quantum mechanics (QM) for both neutral and ionic states as shown in Figure 3. Accordingly, the elementary hopping step in molecular wires is characterized by four energies: E (neutral in neutral geometry) and E^*

(neutral in ion geometry) E_+ (ion in ion geometry) and E_+^* (ion in neutral geometry). By definition,[11,12]

$$I = I_1 + I_2 = (E_+^* - E_+) + (E^* - E) \quad (9)$$

In addition to reorganization energy, the vertical ionization potential (VIP) is also determined by Figure 3. [11]

$$VIP = E_+^* - E \quad (10)$$

The QM calculations to determine these quantities used the B3LYP flavor of Density functional Theory (DFT) with the 6-311G** triple zeta-single polarization basis set.[13] All calculations on open shell (ionized) states used the unrestricted formalism (UB3LYP), but spin contamination was minimal (less than 0.01).

2.3 The coupling matrix element V

We calculated the electron transfer coupling matrix element, V, between adjacent molecules within the framework of the Marcus-Hush two-state model.[11,14], as sketched in Figure 4. Thus the coupling matrix element for a given electronic level is related to the energetic splitting of that level in the dimer as compared to the isolated neutral molecule. For these organics the highest occupied molecular orbital (HOMO) of the isolated molecule is a π orbital delocalized over the molecule (with energy ϵ), which for the neutral dimer splits into two levels denoted as HOMO and HOMO-1. The coupling matrix element, V, is given by

$$V = \frac{1}{2} \sqrt{(E_{HOMO} - E_{HOMO-1})^2 - (\mathbf{e}_2 - \mathbf{e}_1)^2} \quad (11)$$

In this case the isolated molecules are identical (and in equivalent sites in the crystal), so that equation (11) becomes:

$$V = \frac{1}{2} (E_{HOMO} - E_{HOMO-1}) \quad (12)$$

The quantities used in (9) and (12) were obtained from QM calculations as indicated in section 2.2

2.4 Molecular dynamics

To obtain the thermal fluctuations in the hopping matrix elements for a given Temperature and pressure, we carried out MD simulations (using Cerius2 [15]). Here we considered a 3x3x2 supercell with 36 pentacene molecules. We used the Dreiding force field (FF) [16] (reported to be effective for pentacene [17]) with the Lennard-Jones 12-6 description of vdW interactions and (Mulliken) charges from QM populations (shown in Figure 5). The simulations were carried out in the canonical ensemble (NPT), using the Nose-Hoover thermostat (Relaxation Time constant 0.1 ps) to maintain the temperature T and the Rahman-Parrinello barostat (mass factor 1.0) to maintain the pressure P. The electrostatic interactions were calculated using the ABCA formalism for Ewald summations [18].

The cell parameters from minimization and from MD at 300K are compared with the 300K experimental values [19] in Table 1. The densities at 300K differ by 2.4%.

We carried out two series of simulations.

To obtain the temperature dependence we considered 250 K, 300 K, 350 K, and 400 K all at 0.0001 GPa (\sim 1atm) pressure.

To obtain the pressure dependence we considered pressures of 0.0001 GPa, 0.1 GPa, 0.5 GPa and 1.0 GPa all at 300 K.

Each simulation was 100 ps with the measurements over the last 50 ps.

IV-3. Results and Discussion

3.1. Reorganization Energy and Coupling matrix Element

The QM optimized structures for the neutral and oxidized forms of naphthalene, anthracene, tetracene, and pentacene are presented in Figure 6. All neutral and oxidized molecules stay planar [for pentacene the lowest frequency (out-of-plane) is 46.75 cm⁻¹] We see a consistent trend in the alternation of the bond lengths and bond angles due to ionizing the HOMO, Naphthalene shows the largest geometry relaxations, with changes in C–C bond lengths on the order of 0.030 Å, leading to the largest reorganization energy of 0.1893 eV. Pentacene has smallest geometry relaxations, with changes in C–C bond lengths on the order of 0.01 Å, leading to the smallest reorganization energy of $\lambda = 0.0993$ eV. This is in excellent agreement with the value of $\lambda = 0.0992$ eV [20] deduced from experiment. As summarized in Table 2 and Fig. 7, the increased charge delocalization with increased number of conjugated phenyl rings, N , leads to a reorganization energy that decreases uniformly as

$$I = 0.0395 - 0.3024/N(\text{eV}) \quad (13)$$

The calculated vertical ionization potentials (Table 2) are 2 to 6 % lower than experimental results [21].

The crystal structure leads to the four types of dimers; T1, T2, P and L shown in Figure 2. The T1 dimer is closest at 4.7 Å with a cross angle of $\sim 51.90^\circ$ as shown in Figure 8a. The T2 dimer is at ~ 5.13 Å with a cross angle of 52° but with a slide shift of 2.46 Å as shown in Figure 8b. The P dimer has adjacent molecules at 6.25 Å distance and parallel, but this displacement is at an angle of 53° from the normal to the molecular plane as in Figure 8c. The L dimer has neighbors at 14.10 Å and almost parallel as in Figure 8d. The geometries of the dimer structures were optimized (B3LYP/6-311G**) with the center mass distance and cross-angle plane fixed.

For pentacene dimer, the coupling in the T1 dimer ($V=0.137$ eV) and T2 (0.120 eV) are far larger than for P (0.006 eV) and L (0.0008 eV). Thus P and L dimers contribute little to hole mobility. This indicates that the hole mobility is quite anisotropic and dominated by hole transfer within the layers, which is consistent with experiment. [22] Of course the coupling depends on the distance between the dimers as shown in Figure 9 for the T1 and P dimers. Even at the same distance, the P dimer has a much smaller coupling than the T1 dimer. For example, the coupling in T1 dimer with 4.734 Å (and a cross angle of $\sim 51.90^\circ$) is 0.137 eV, but it decreases to 0.105 when the two phenyl rings are parallel to each other with the same CM distance of 4.734 Å. This is because the orbitals of the T1 dimer can couple through the hydrogen atoms which penetrate close to the pentacene face of the dimer partner. On the other hand, P dimer becomes much more stable than T1 dimer when the CM is less than 4.9 Å and the coupling of P dimer becomes larger than T1 dimer while the CM is less than 3.9 Å. Indeed at the optimum distance of 3.6 Å the coupling is 0.30 eV.

Considering all four oligocenes, the largest coupling matrix elements V are all in the range from 0.10 eV to 0.13 eV. Since the observed mobilities differ by over a factor of 10, the coupling matrix element term may not be the only important factor in determining hole transport.

3.2. Transport properties

The diffusion coefficient and the drift mobility of holes in oligoacene were estimated from eqn 1-4 using the internal reorganization energies and the coupling matrix elements based on QM.

3.2.1 Mobility Estimate based on minimized crystal structures

First we ignore structural disorder at ambient conditions. For pentacene this leads to $\mu = 5.37 \text{ cm}^2/\text{Vs}$, which compares well with the experimental values of 3-7 cm^2/Vs .^[4] However, for tetracene we find $\mu = 4.24 \text{ cm}^2/\text{Vs}$, which is much larger than current experiments 0.15~0.4 cm^2/Vs .^[23,24] Since the reorganization energies (both experimental and theoretical) and coupling matrix elements of tetracene and pentacene are similar, we conclude that *the current experimentally mobility of tetracene is only 1/10 of its optimum value so that further effort could likely improve the hole mobility by a factor of 10.*

3.2.2 Estimate based on Molecular Dynamics

As the temperature increases, structural disorder modifies the matrix elements, changing the hole mobility for the system. To predict these changes, we use equation (5)-(8) to calculate the hole mobilities as a function of temperature.

We carried out NPT MD simulations for pentacene at temperatures of 250K, 300K, 350K, and 400K (with 1 atm pressure). These calculations require the radial distribution function as a function of temperature as shown in Figure 10. As the temperature increases, the population of T_1 and T_2 dimers decrease, leading to reduced hole mobilities as shown in Figure 11. The calculated hole mobility behaves as: $\mu \sim T^{-0.57}$.

We also carried out MD simulations at pressures of 1 atm, 0.1 GPa, 0.5 GPa and 1 GPa all at 300K. As the pressure increases we find that the T_1 type dimer distance decreases while the T_2 type distance increases. The calculated distribution functions are shown in Figure 12. This leads to the calculated hole mobilities shown in Figure 13, indicating that the hole mobilities increase with increased external pressure. However, change is less than a factor of 1.4 times, suggesting that merely changing the pressure will not dramatically increase hole mobilities of pentacene.^[25]

3.3 Toward higher hole mobilities

Many efforts are being made to improve the hole mobility of pentacene by using different substrates, different deposition methods etc. These efforts are generally directed toward changing the crystal packing to obtain a phase with higher mobility. Here we will use our simple transport model (with the hole mobilities governed by just two parameters: coupling matrix element and reorganization energy) to discuss several possibilities for improving mobilities via modified crystal packing of oligoacene.

Since the T_1 and T_2 dimers have similar coupling elements (0.137 and 0.120 eV) despite larger differences in distances (4.7 and 5.2 Å), we propose that a packing structure containing increased numbers of T_2 dimers might lead to a higher hole mobility. Figure 14a shows this type of structure. Each unit cell has two molecules, the center molecule overlaps half of the side molecules. This structure allows hole hopping between layers, which might dramatically improve mobility.

Because P dimer will be more stable than T_1 dimer at short distance (less than 4.9 Å), we propose that another packing structure only containing P dimers might also have an even higher hole mobility. Figure 14b shows this type of structure. The structure was minimized by Dreiding Force Field. The optimum CM of P dimers in the crystal is 3.6 Å, leading to a coupling is 0.30 eV. Based on same method presented in section 3.2.1, the hole mobility of this structure will be 15.2 cm²/Vs, 2.8 times larger than the value of 5.37 cm²/Vs for the normal crystal.

Based on equation 1 the second parameter, reorganization energy, depends exponentially on the hole mobility. Since smaller reorganization energies lead to larger hole mobilities, the design of new organic systems should consider adding groups that

can delocalize the charges on the oligoacenes to help reduce the reorganization energy. Clearly adding additional aromatic groups to form hexacene and heptacene would lead to decreased reorganization energies as in equation (13) and hence larger mobilities.

IV-4. Conclusions

We present here a simple transport model to predict the drift mobility of oligoacenes from parameters deduced from QM calculations. In this model the drift mobility (μ) depends mainly on the monomer reorganization energy (λ) and the coupling matrix element (V) between dimers. Our results for pentacene ($\mu = 6.5 \text{ cm}^2/\text{Vs}$) is close to the best experiments ($\mu = 3\text{-}7 \text{ cm}^2/\text{Vs}$), validating our model.

We find that the drift mobility decreases around 9% (8.3% from 250K to 300K, 9.2 % from 300K to 350K) with a 50K increase in temperature due to reduced the electron coupling matrix elements. We find that an increased pressure of 1 GPa leads to only a 3.4% increase in the mobility. However repacking the monomers to form a crystal dominated by P type dimers could lead to hole mobilities as high as $15.2 \text{ cm}^2/\text{Vs}$.

We suggest that this simple model might be useful for determining new solid state structures that could lead to the higher hole mobility desired for high performance molecular devices, and we suggest some alternative solid state structures for such studies.

Acknowledgement

We thank Dr. Terry Smith (3M corporation) for suggesting this as an interesting problem and we thank 3M for a gift that helped support this work. This research was also supported partly by funds from the NSF S&T Center for Photonics (Larry Dalton, U. Washington).

The computational facilities were provided by DURIP grants from ARO and ONR. The facilities of the Materials and Process Simulation Center are also supported by ONR, DOE

(ASC, FETL), NSF, MURI-ARO, MURI-ONR, General Motors, ChevronTexaco, Seiko-Epson, Beckman Institute, and Asahi Kasei.

Reference

- [1] Ye, J.; Chen, H.Z.; Shi, M.M.; Wang, M.; *Progress in Natural Science* **2003**, 13, 81-87 and references therein.
- [2] Dimitrakopoulos, C. D. and Malenfant, P. R. L.; *Adv. Mater.* **2002**, 14, 99-117 and references therein.
- [3] Dimitrakopoulos, C. D. and Mascaro, D. J. *IBM J Res. Dev.* **2001**, 45, 11-27 and references therein.
- [4] (a) Kelley, T. W.; Muyres, D. V.; Baude, P. F.; Smith, T. P. and Jones, T. D. *Mat. Res. Soc. Symp. Proc.* **2003**, 771, L.6.5.1 (b) Klauk, H.; Halik, M.; Zschieschang, U.; Schmid, G.; Radlik, W.; Weber, W. *J. Appl. Phys.* **2002**, 92, 5259.
- [5] Cheng, Y. C.; Silbey, R.J.; da Silva Filho, D. A.; Calbert, J. P.; Cornil, J. and Bre´das J. L.; *J. Chem. Phys.* **2003**, 118, 3764-3774.
- [6] Karl, N.; *Synthetic Metals* **2003**, 133–134, 649–657.
- [7] Silinsh E.A. and Capek V. “Organic Molecular crystals: interaction, localization and transport phenomena”. " AIP Press, **1994**, New York. page 332-333
- [8] Senthilkumar, K.; Grozema, F. C. ; Bickelhaupt, F. M. and Siebbeles, L. D. A.; *J. Chem. Phys.* **2003**, 119, 9809
- [9] Wegewijs, B. R. and Siebbeles, L. D. A.; *Phys. Rev. B*, **2002**, 65, 245112
- [10] Berlin, Y. A.; Hutchison, G. R.; Rempala P.; Ratner, M. A. and Michl, J.; *J. Phys. Chem. A*, **2003**, 107, 3970-3980.

- [11] (a) Marcus, R. *Ann. Rev. Phys. Chem.* **1964**, 15, 155. (b) Bixon M.; Jortner J. *Adv. Chem. Phys.* **1999**, 106, 35-208. (c) Bolton, J. R.; Mataga, N.; McLendon, G. In *Electron Transfer in Inorganic, Organic, and Biological Systems*; Bolton, J. R., Mataga, N., McLendon, G., Eds.; *Advances in Chemistry* Series No. 228; American Chemical Society: Washington, DC, **1991**; (d) Bixon M. and Jortner J. *Adv. Chem. Phys.* **1999**, 106, 35-208.
- [12] (a) Burin, A. L.; Berlin, Y. A.; Ratner, M. A. *J. Phys. Chem. A* **2001**, 105. (b) D. Raineri, F. O.; Friedman, H. L. *Adv. Chem. Phys.* **1999**, 107, 81. (c) Matyushov, D. V.; Voth, G. A. *J. Phys. Chem.* **1999**, 103, 10981. (d) Tavernier, H. L.; Kalashnikov, M. M.; Fayer, M. D. *J. Chem. Phys.* **2000**, 113, 10191. (e) Matyushov, D. V.; Voth, G. A. *J. Phys. Chem. A* **2000**, 104, 6470. (f) Tavernier, H. L.; Fayer, M. D. *J. Chem. Phys.* **2001**, 114, 4552.
- [13] Jaguar 4.0 quantum mechanics program.. Schodinger Inc., Portland Ore. See B. H. Greeley, T. V. Russo, D. T. Mainz, R. A. Friesner, J-M. Langlois, W. A. Goddard III, R. E. Donnelly, and M. N. Ringnalda; *J. Chem. Phys.* **101**, 4028 (1994)
- [14] (a) Marcus, R. *J. Chem. Phys.* **1956**, 24, 966. (b) Hush, N. S. *J. Chem. Phys.* **1958**, 28, 962. (c) Hush, N. S. *Trans. Faraday Soc.* **1961**, 57, 577.
- [15] Cerius2 molecular dynamics software. Accelrys Inc., San Diego CA.
- [16] Mayo, S. L.; Olafson, B. D.; Goddard, W. A., III. *J. Phys. Chem.* **1990**, 94, 8897.
- [17] Mattheus, C.C.; de Wijs, G. A.; de Groot, R. A. and Palstra, T. T. M.; *J. Am. Chem. Soc.* **2003**, 125, 6323-6330
- [18] Karasawa N. and Goddard W.A. III. *J. Phys. Chem.* **1989**, 93, 7320.
- [19] Cambridge Structural Database a). Naphthalene: Brock, C.P. and Dunitz, J.D. *Acta Crystallogr., Sect. B: Struct. Sci.* **1982**, 38, 2218 b) Anthracene: Brock, C. P. and Dunitz, J. D. *Acta Crystallogr., Sect. B: Struct. Sci.* **1990**, 46, 795; c) Tetracene and

- Pentacene: Holmes, D.; Kumaraswamy, S.; Matzger, A.J. and Vollhardt, K.P.C.
Chem. Eur. J., **1999**, 5, 3399. <http://www.ccdc.cam.ac.uk/products/csd/>
- [20] (a) Coropceanu, V.; Malagoli, M.; da Silva Filho, D. A.; Gruhn, N. E.; Bill, T.G. and Bre´das J. L.; *Phys. Rev. Lett.* **2002**, 89, 275503. (b) Gruhn, N.E.; da Silva Filho, D.A.; Bill, T.G.; Malagoli, M.; Coropceanu, V.; Kahn, A. and Bre´das, J. L.; *J. Am. Chem. Soc.* **2002**, 124, 7918-7919.
- [21] Ion Energetics Data in NIST Chemistry Webbook, NIST Standard Reference Database Number 69, edited by P. J. Linstrom and W. G. Mallard National Institute of Standards and Technology, Gaithersburg, MD, **2001** <http://webbook.nist.gov>
- [22] Chen, X. L.; Lovinger, A. J.; Bao, Z. and Sapjeta J.; *Chem. Mater.* **2001**, 13, 1341-1348.
- [23] Butko, V.Y.; Chi, X. and Ramirez, A. P.; *Solid State Communications* **2003**, 128, 431–434
- [24] de Boer, R. W. I. ; Klapwijk, T. M. and Morpurgo, A. F. *Appl. Phys. Lett.* **2003**, 83, 4345.
- [25] Farina, L.; Brillante, A.; Della Valle, R.G.; Venuti, E.; Amboage, M. and Syassen, K.; *Chem. Phys. Lett.* **2003**, 375, 490–494
- [26] (a) Podzorov, V.; Sysoev, S. E.; Loginova, E.; Pudalov, V. M. and Gershenson, M. E.; *Appl. Phys. Lett.* **2003**, 83, 3504. (b) Podzorov, V.; Pudalov, V.M.; Gershenson, E. *Appl. Phys. Lett.* **2003**, 82, 1739.
- [27] E. Demiralp and W. A. Goddard III; *Phys. Rev. B* **56**, 907 (1997)

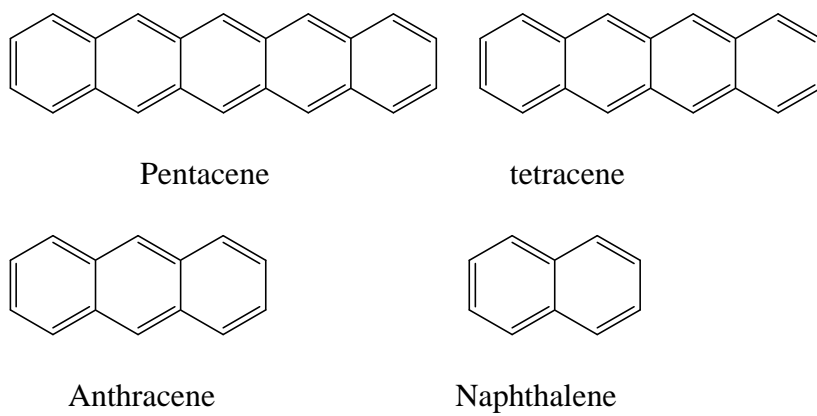


Figure 1. Chemical structure of several oligoacenes

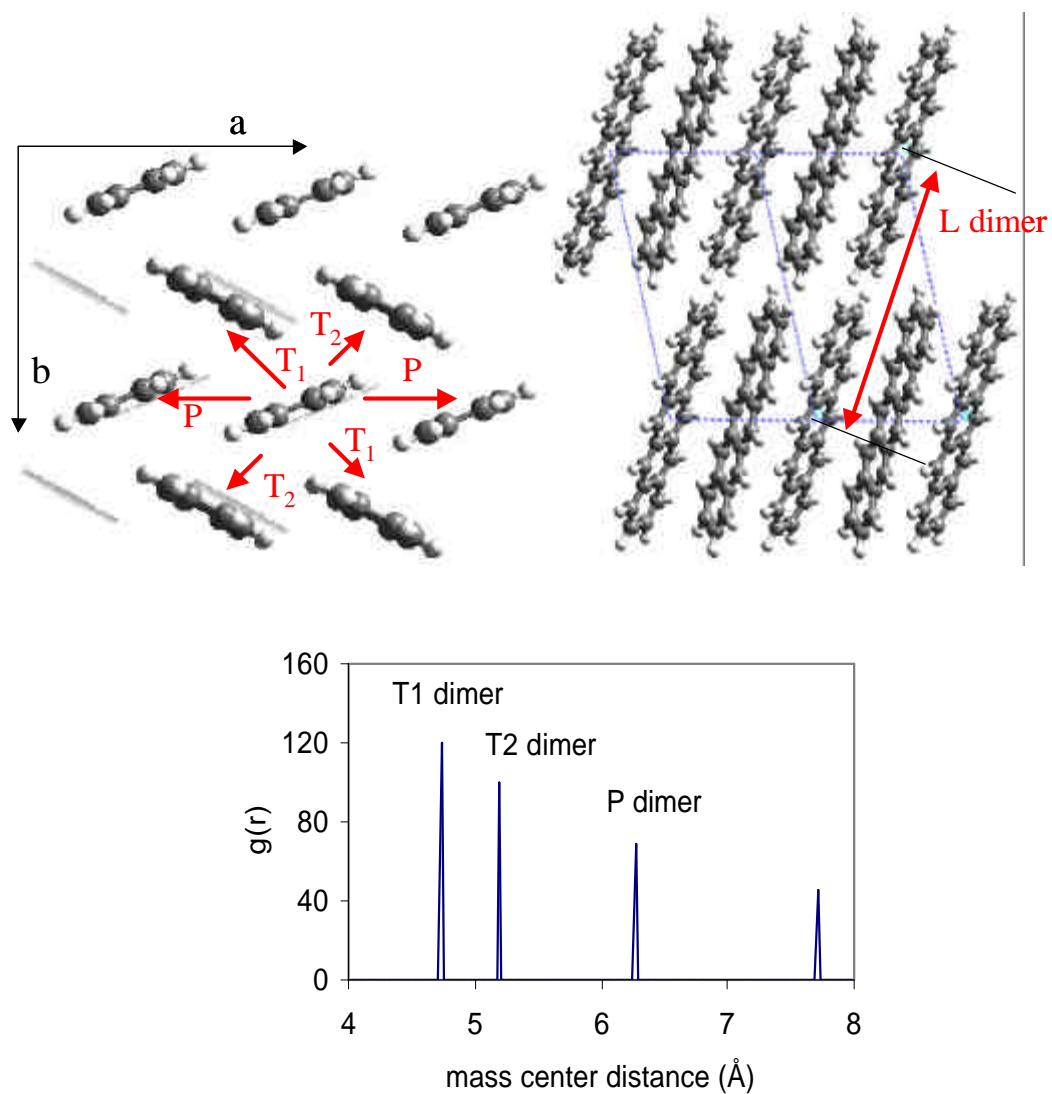


Figure 2. The crystal structure of pentacene crystal, a typical oligacene. A) The dimers types neighbors in the crystal. B) radial distribution function for the different dimer types.

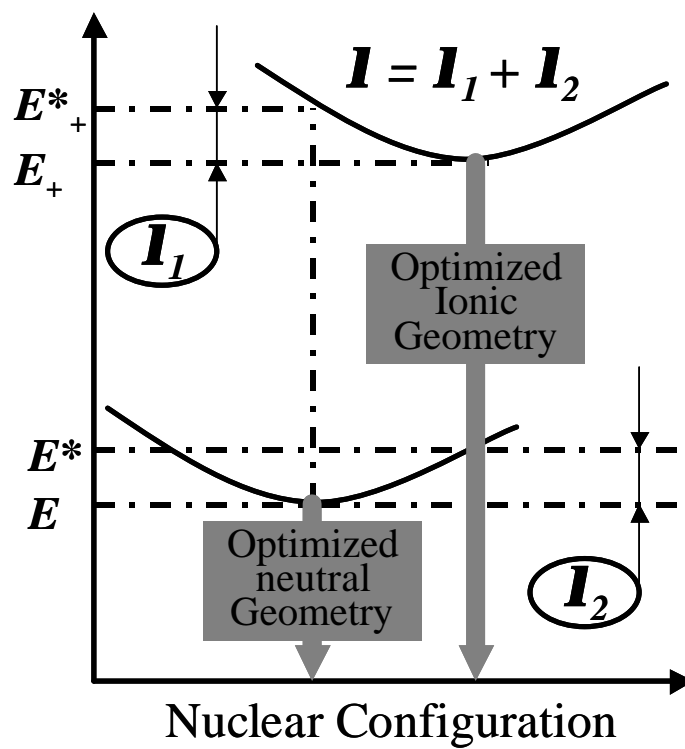


Figure 3. Schematic diagram for the Marcus-Hush calculation of Reorganization energy.

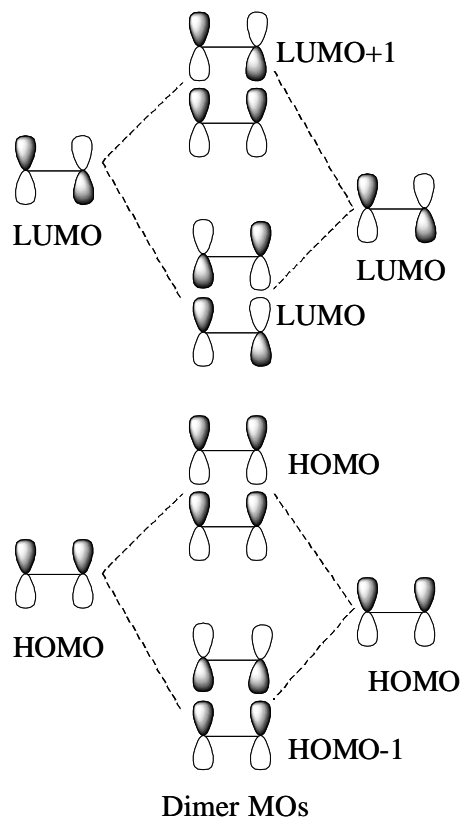


Figure 4. Diagram for the estimate of coupling matrix elements in the neutral dimer.

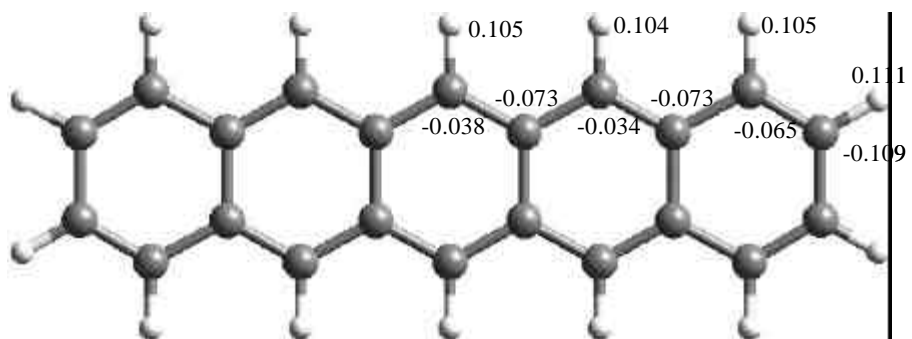


Figure 5. QM charges for neutral pentacene molecule.

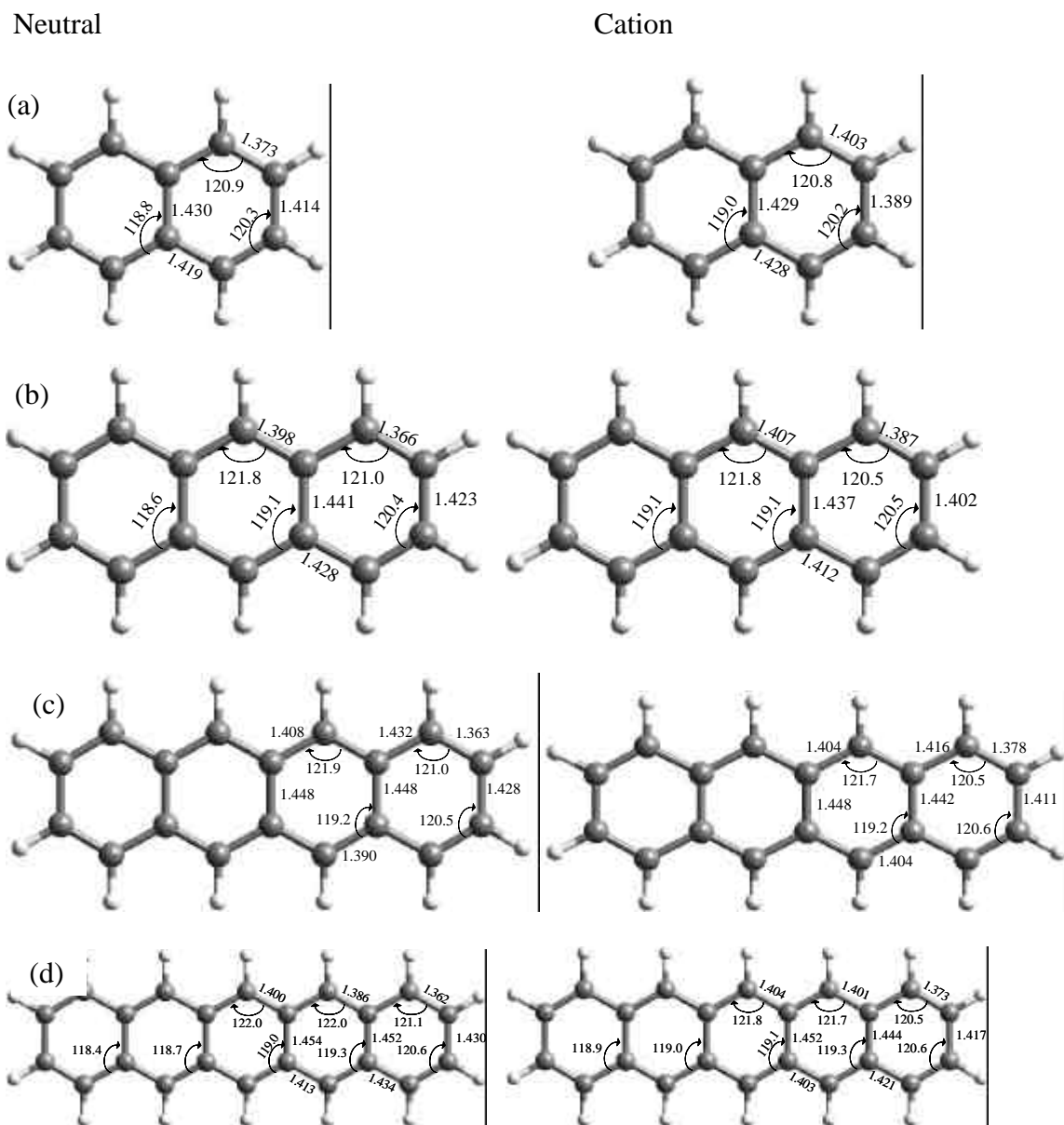


Figure 6. Structural data from QM calculations of the neutral and cation states of oligoacenes. a). Naphthalene; b) Anthracene; c) Tetracene; d) Pentacene.

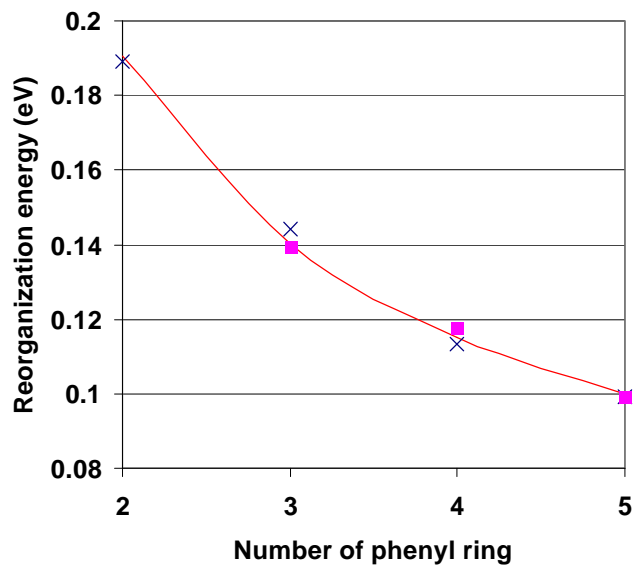


Figure 7. The reorganization energy versus the number of phenyl rings. The calculated values are indicated by cross while the experimental numbers are indicated by square. The line is based on fitting equation $I = 0.0395 - 0.3024/N(eV)$.

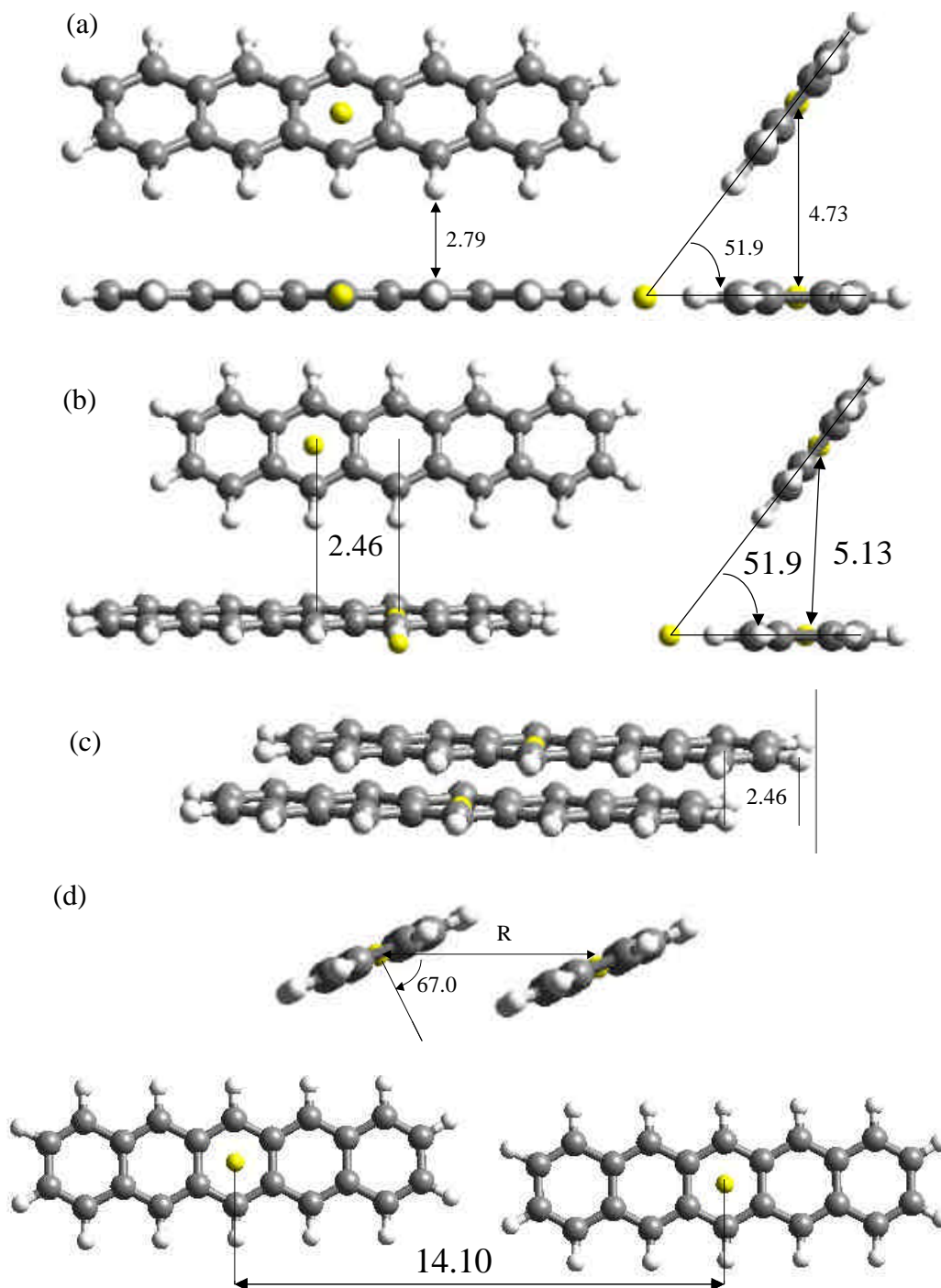


Figure 8. The QM structures for various dimers. a) Front view and side view of T₁ dimer. The yellow atoms are dummy atoms for convenience in defining angles and distances. The structure was optimized by fixing the planar angle at 51.9° and the center of mass (CM) distance at 4.73 Å. b) Front view and side view of T₂ dimer. The CM is slid away by 2.46 Å and the CM distance is 5.13 Å. c) Front view and side view of P dimer. The mass center distance is 6.25 Å., which is at an angle of 67° from the normal to the molecule d) Front view of L dimer. The CM distance is 14.10 Å.

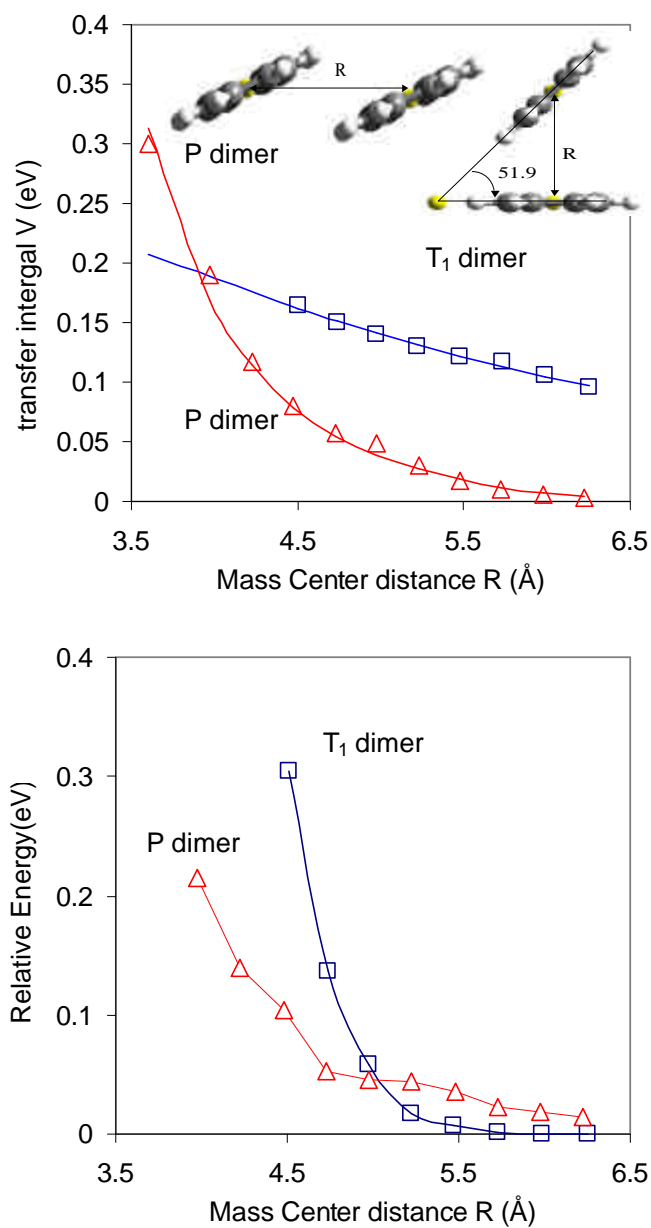


Figure 9. Dependence of coupling matrix elements (calculated using B3LYP/6-311G**) on the CM distance. For the T_1 dimer the 51.9° angle is kept fixed while the R is varied (squares are quantum mechanic data, the curve is based on fitting equation as $|V(r)| = 0.4708 - 0.0912r + 0.0050r^2$). For the P dimer the two molecules are kept parallel while the R is varied (triangles are QM data, the curve is based on fitting equation $|V(r)| = -0.0078 + 697.0/r^6 + 0.3252/r^{12}$).

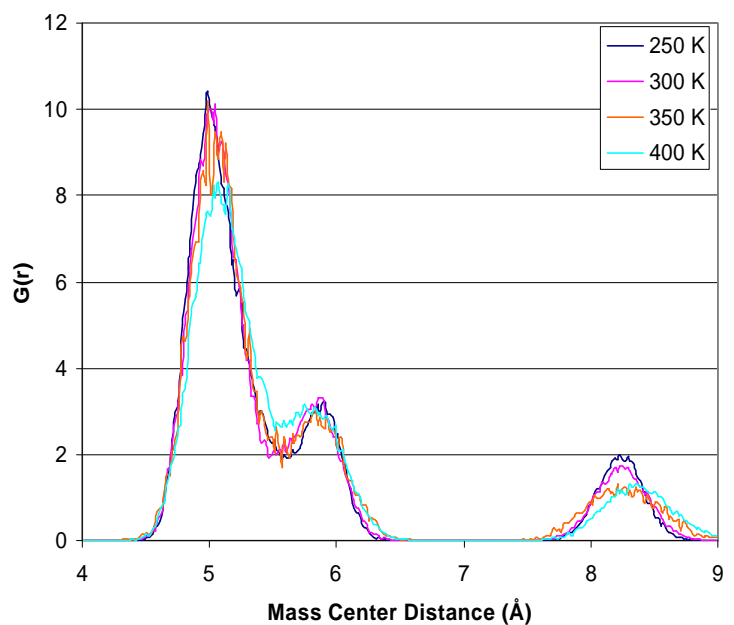


Figure 10. Radial distribution $g(r)$ of pentacene calculated from MD simulations as a function of temperature. (1 atm)

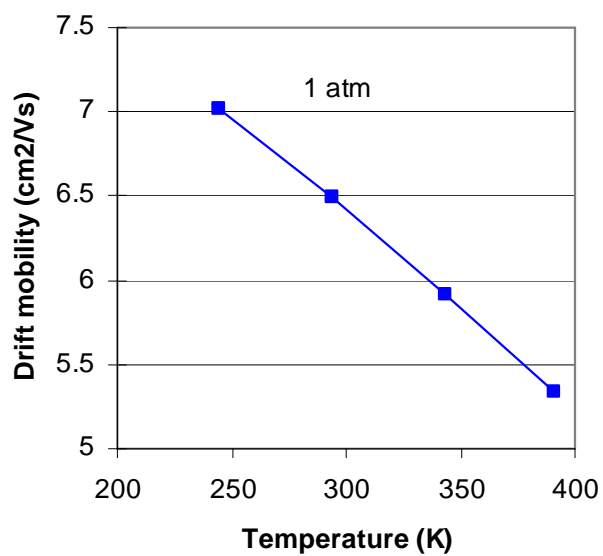


Figure 11. The drift mobility calculated for pentacene as a function of temperature.

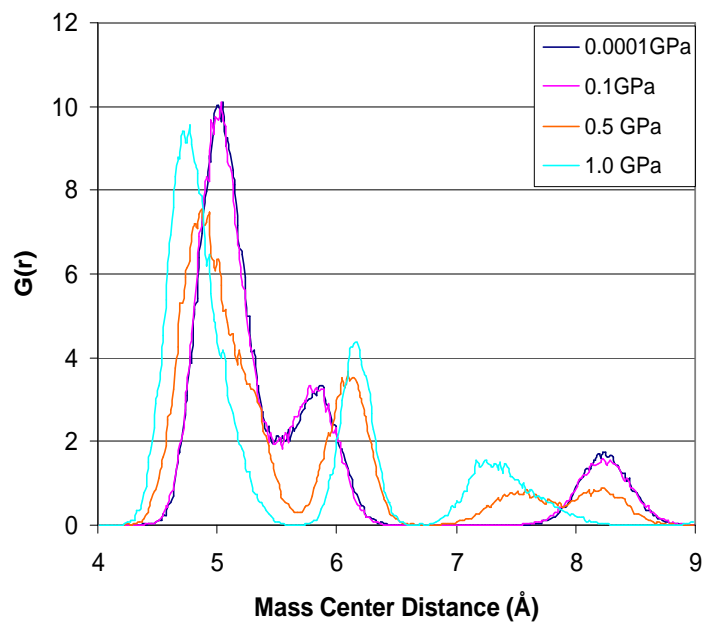


Figure 12. Radial distribution $g(r)$ of pentacene calculated from MD simulation at different pressures. (300K)

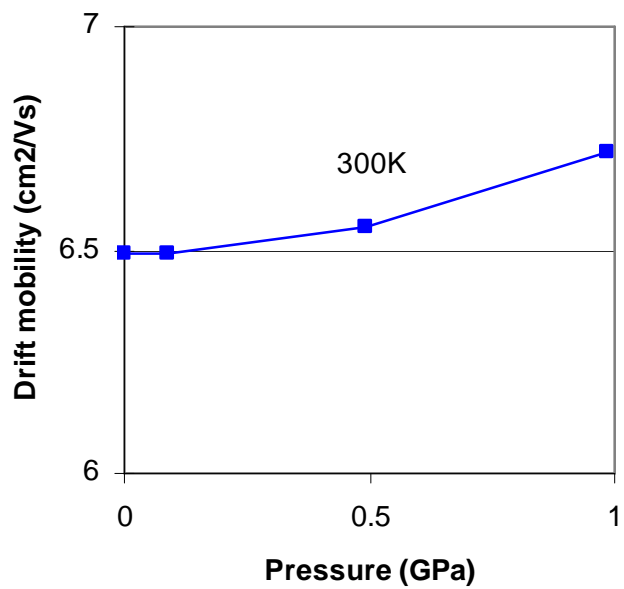


Figure 13. The drift mobility calculated for pentacene as a function of pressure.

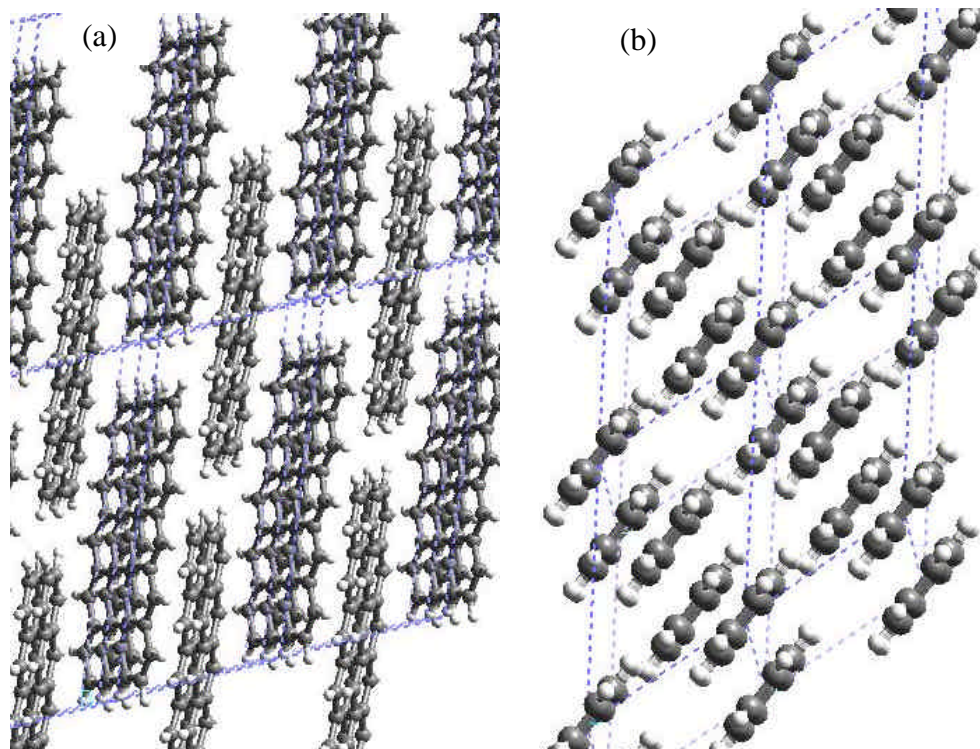


Figure 14. a) The proposed cross layer crystal packing. b) The proposed pure P type package crystal. Dreiding force field minimization gives the crystal structure with 1.343 g/cm³ density and cell parameters ($a=6.43 \text{ \AA}$, $b= 8.89 \text{ \AA}$, $c=15.90 \text{ \AA}$, $\alpha=73.33^\circ$, $\beta=75.13^\circ$, $\gamma=52.64^\circ$).

Table 1. The optimum crystal cell parameters for pentacene from experiment (ref 19), MD at 300K and from minimization.

	Experiment (300K)	MD (300K)	minimized
A (Å)	6.275	5.950	6.243
B (Å)	7.714	8.423	7.485
C (Å)	14.442	17.445	16.052
α	76.75°	94.76	69.3°
β (°)	88.01°	112.57	81.68°
γ (°)	84.52°	91.24	86.16°
Cell Density (g/cm ³)	1.3649	1.2348	1.3317

Table 2. The QM energies (hartree) for each structure calculated from QM (UB3LYP/6-311G**). The vertical Ionization Potential (VIP) and reorganization energy (λ) are in eV.

		naphthalene	Anthracene	tetracene	pentacene
E (Hartree)		-385.98524	-539.65551	-693.32308	-846.98975
E* (Hartree)		-385.98185	-539.65299	-693.32099	-846.98774
E ₊ (Hartree)		-385.69769	-539.39689	-693.08378	-846.76430
E* ₊ (Hartree)		-385.69413	-539.39413	-693.08171	-846.76267
VIP(eV)	This work	7.9286	7.1190	6.5740	6.1845
	Experiment	8.144 ^a	7.202 ^a	6.97 ^a	6.63 ^a
λ (eV)	This work	0.1893	0.1441	0.1135	0.0993
	Experiment		0.1394 ^b	0.1176 ^b	0.0992 ^b

(a). NIST database Ref. 21 (b). Podzorov, V.; et al. Ref. 26

Table 3. Calculated properties of oligoacenes

		Naphthalene	Anthracene	Tetracene	Pentacene
T ₁ dimer CM distance (Å)		5.078	5.188	4.774	4.734
V _{T1} (eV)		0.114	0.0986	0.136	0.137
T ₂ dimer CM distance (Å)		5.078	5.188	5.126	5.199
V _{T2} (eV)		0.114	0.0986	0.118	0.120
P dimer CM distance (Å)		5.973	6.000	6.030	6.253
V _p (eV)		0.006
L dimer CM distance (Å)		8.675	11.12	13.53	14.10
V _L (eV)		0.0008
Diffusion coefficient, D (cm ² /s)		0.0342	0.0477	0.1096	0.1387
Drift mobility, μ (cm ² /Vs)	This work	1.32	1.84	4.24	5.37
	Experiment	0.4~1 ^a	0.57~2.07 ^b	0.14 ^c 0.4 ^d	3 ^e ; 5~7 ^f

(a) Karl, N.; et al. Ref. 6. (b) Silinsh E.A.; et al. Ref. 7a (c) Butko, V.Y.; et al. Ref. 23.

(d).de Boer, R. W. I. ; et. al. Ref. 24. (e) Klauk, H.; et al. Ref. 4b. (f).Kelley, T.W.; et al

Ref. 4a.

Table 4. Experimental cell parameters used in matrix element calculations. Ref. 19

	Naphthalen ^a	Anthracene ^b	Tetracene ^c	Pentacene ^d
Space group	P _{21/a}	P _{21/a}	P ₋₁	P ₋₁
A (Å)	8.213	8.467	6.057	6.275
B (Å)	5.973	5.999	7.838	7.714
C (Å)	8.675	11.124	13.010	14.442
α	90.00 ⁰	90.00 ⁰	77.13 ⁰	76.75 ⁰
β	123.39 ⁰	125.06 ⁰	72.12 ⁰	88.01 ⁰
γ	90.00 ⁰	90.00 ⁰	85.79 ⁰	84.52 ⁰
Cross angle	52.3 ⁰	51.1 ⁰	51.3 ⁰	51.9 ⁰

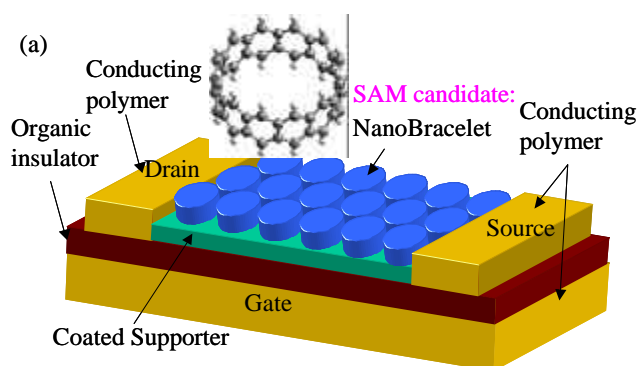
Chapter V

THE NANO-BRACELET, A NEW FAMILY OF ORGANIC SEMICONDUCTORS

Abstract

Organic π -conjugated materials offer remarkable potential for making soft electronic devices, e.g., all-plastic integrated circuits for low-end electronics. Unfortunately, the relatively low mobility of these materials has restricted the applications of organic semiconductors to low switching speed devices, such as active matrix LCDs and smart card data storage. Currently, the largest hole mobility for a p type organic semiconductor, is $\sim 5 \text{ cm}^2/\text{Vs}$ for pentacene thin films. This approaches the hole mobility of amorphous silicon, which is $\sim 10 \text{ cm}^2/\text{Vs}$, [1]. However, it is far too low for CPU or memory applications. In contrast, semi-conducting single wall carbon nanotubes have hole mobilities at room temperature [2] of up to $7.9 \times 10^4 \text{ cm}^2/\text{Vs}$. This indicates that there may be organic semiconductor materials with ultra-high hole mobilities. To find such new materials, we used quantum mechanics and molecular dynamics to simulate the properties of various material designs. This led to the new nano-bracelet family of organic semiconductors, which we predict to have an ultra-high hole mobility ~ 10 -600 times higher than that of pentacene.

Figure for Table of Contents (A design of the flexible transistor by using nano-bracelet)



To explore the dependence of hole mobility on the structure and the character of organic materials, we calculated the hole mobilities of molecules related to oligoacenes by using a combination of quantum mechanical calculations and the transport model in reference [3]. For organic semiconductors, the incoherent transport model can describe hole mobility better than the coherent band-like transport model.[4] The hole mobility μ

can be written as $\mathbf{m} = \frac{e}{k_B T} D = \frac{e}{k_B T} \frac{1}{2n} \sum_i r_i^2 W_i P_i$ where $n = 3$ is the dimensionality, D is

the charge diffusion coefficient, W_i is the hopping rate of the charge carrier to the i th neighbor, r_i is the distance to i th neighbor, and P_i is the hopping probability for charge to transfer the i th neighbor, $P_i = W_i / \sum_i W_i$. The hopping rate W is determined by

$W = \frac{V^2}{\hbar} \left(\frac{\mathbf{p}}{k_B T} \right)^{1/2} \exp\left(-\frac{I}{4k_B T} \right)$ [5], where V is the electronic coupling matrix element

between donor and acceptor, k is the Boltzman constant, h is the Planck constant and λ is the reorganization energy. The reorganization energy λ and coupling matrix element V are the parameters calculated based on the quantum mechanics of the organic semiconductor monomer structure and the various dimer configurations from crystal structures. [6]

After examining the trend of hole mobilities in oligoacene,[7] we investigated a circular aromatic system by connecting the head and tail of oligoacene molecules. We expect that this structure will have ultra-high hole mobility because it is a minimum semiconducting single wall carbon nanotube, which could possess highly delocalized charges and thus, a small reorganization energy. Figure 1a shows the structure of such a system, which we name the nano-bracelet. We have evaluated the hole mobilities of nano-bracelets by using the model above. The blue curve in Figure 2a shows the predicted reorganization energy of the nano-bracelet. The reorganization energy of the bracelet is proportional $1/N^2$ to the number of rings along p conjugated, $I(N) = 7.279/N^2$ eV. The convergence of reorganization energy at infinite diameter bracelet is zero. The C-C bond length changes from neutral to cation are near zero (less than 0.001 Å). However, this decreased the diameter of the nano-bracelet by approximately 0.04 Å, which contributes to the reorganization energy. We can see the

structural changes between the neutral and the cation forms of the nano-bracelet are much smaller than between the neutral and the cation forms of oligoacenes. This leads to smaller reorganization energies. In fact, 10, 12, 14 and 16 nanobracelets have reorganization energies at 0.0679, 0.0460, 0.0357 and 0.0217 eV, respectively. The dimer structures of nanobracelets have been determined from the bracelet crystal optimized by the Dreiding force field. The intermolecular distances are between 3.3 Å to 3.4 Å. The couplings of dimer structures give good inverse proportion relation with the center of mass (CM) distance, $V(r) = 0.609/r + 0.042$ eV. The convergence of the coupling matrix element is zero at infinite center of mass distance. The blue curve in Figure 2b shows the dependence of coupling versus the CM distance of bracelet. Based on same model, we predicted the hole mobilities of nano-bracelet systems. The mobilities are shown as blue squares in Figure 2c. The 10, 12 and 14 bracelets have hole mobilities of 23.0, 38.5 and 57.2 cm²/Vs, respectively. For tbracelet-14, the hole mobility is already 10 times higher than best known organic semiconductor, pentacene.

To predict the hole mobilities of larger bracelet systems, we used the above fitting equations for the reorganization energy $\lambda(N)$ and the coupling element $V(r)$. The predicted results are shown as the light blue squares in Figure 2c. We find that hole mobility increases as the size of the bracelet increases. Bracelet-90 reaches a hole mobility of 4.9×10^3 cm²/Vs at room temperature. This hole mobility is 600 times higher than pentacene [1] and 10 times higher than silicon, 480cm²/Vs [10]. This ultra-high hole mobility implies an important potential improvement for soft electronic device applications.

We also evaluated the band gap versus the size of the bracelet by using the method in Reference [11]. (Details are shown in Supportive information SI). The evaluated band gaps are shown as blue squares in Figure 2d. The blue curve in Figure 2d is a fitting to the results calculated by assuming inverse dependence of band gap on the size of the bracelets. Bracelet 14 has a calculated band gap of 0.532eV and bracelet 90 has an estimated band gap of 0.31 eV. Those number are close to the band gap of semiconducting carbon nanotubes which has been used in nanoscale transistors.[12] A small band gap can usually lead to power savings in devices, which brings advantages for applications in portable devices.

For comparison, we study the properties of cyclic-polyacetylene (c-PA) system. Figure 1b shows the c-PA structures in which the ring is consisted of CH=CH-CH monomers instead of aromatic rings. The reorganization energy of c-PA is also proportional to $1/N^2$ the number of double bonds; $I(N) = 8.782/N^2 + 0.192$ eV, but it is almost three times larger than the bracelet system. Because the ring of c-PA consists only of double bonds instead of aromatic bonds, it does not have a resonant structure. The C-C bond lengths in c-PA are 1.46 and 1.38 Å for double and single bonds, respectively. From neutral to cation, c-PAs have much larger structural changes. For example, c-PA 12 C=C double bond increases by 0.02 Å and C-C single bond decreases by 0.02 Å. The pink curve in Figure 2b shows the dependence of coupling versus CM distance of the dimers. The coupling of c-PA dimer also has a coupling energy that varies inversely with CM distance, $V(r) = 0.509/r + 0.013$ eV. However, its coupling is much weaker, around 1/10 of the coupling bracelet dimers. The hole mobilities of c-PA family are shown as pink triangles in Figure 2c. Compared to a nanobracelet of the same size, the c-PA system only has around 1/600 of the nanobracelet's hole mobility. Moreover, the hole mobility of c-PA may be overestimated because the c-PA's relatively greater flexibility could lead to worse coupling structures. To predict the properties of large sized c-PA systems, we used same method as for the nanobracelet. The bright pink triangle points in Figure 2c show the predicted hole mobilities for c-PA system. For c-PA-90, the mobility goes up to $8\text{cm}^2/\text{Vs}$ at the end of curve. Figure 2d shows the predicted band gap for c-PA system. For infinite c-PA, the band gap decrease down to 0.93eV, which is in agreement with the value of the linear PA band gap.[13]

It may be difficult to synthesize the nanobracelet because bracelet rings should have high strain energies. We evaluated the strain energies of the bracelet systems to estimate the difficulty in synthesis. The calculated strain energies are shown in Figure 3a.[19]. These energies obey the relation $E \propto A/R^2$, which is quite similar to Gao's findings for the carbon nanotube. [14] Comparing with the c-PAs, bracelets have larger strain because aromatic rings are more resistant to twisting. Considering that c-PA-8 has been made, [15] we conclude that the synthesis of bracelets larger than bracelet-10 may be feasible.

Another factor affecting the crystal packing is the rigidity of the molecules. While the ring diameter becomes larger, the structure of ring molecule will change to a flat shape.

Figure 3b shows the energy difference of two structures versus the diameters. Diameter larger than bracelet 90 will favor the flat structure. The geometry change thus leads to defects in crystal or monolayer structures and leads to lower mobility. Therefore, based on Figure 3a and 3b, we conclude that bracelets with sizes ranging from 12-90 are the best candidates for practical applications.

For making fully organic transistors, we propose a scheme shown in Figure 4a. The gate, source and drain consist of a conducting polymer. The coated surface is to provide good surface pattern on which to deposit a Self-Assembling Monolayer (SAM) of organic semiconductor. Indeed, in such a scheme, the most important part is finding a suitable candidate for the organic semiconductor. We propose the usage of the nanobracelet. Figure 4 (b) (c) (d) shows MD simulations of pentacene, c-PA and bracelet SAM on poly-styrene surfaces. The SAM of pentacene will depend on the roughness of the surface and c-PA cannot achieve good crystal packing. However, the bracelet systems can make a better SAM, which leads directly to higher hole mobilities.

Although SWNT transistors may be extremely interesting for next generation electronics based on their small sizes and ultra-high hole mobilities, the alignment and assembly of SWNT on a large scale is still a large barrier. [16] The nanobracelet system, has several advantages over SWNT or any other organic semiconductors.

- 1). Being a relatively small molecule, the nanobracelet is much easier self-assemble than larger molecules like SWNTs. It should be possible to create SAM using mature technologies such as printing or vapor deposition.

- 2) The nanobracelet has comparable hole mobility to the SWNT. We can consider it a short SWNT.

- 3). Nanobracelets have much smaller band gaps than pentacene. The band gaps are comparable to those SWNTs, enabling lower power consumption in devices.

- 4) We can manipulate the additional groups on the bracelet during synthesis. Those additional groups can be chosen to have better alignment with certain coated surfaces.

In summary, we propose the nanobracelet as a new family of organic semiconductors that has the largest hole mobilities among all known organic semiconductors. It has most advantages of SWNTs without some of their technical drawbacks such as difficulties with

large scale assembly. If synthesized, this material may start a new era of soft device fabrication.

Acknowledge: We thank Diego Benitez (Robert H. Grubbs' group) for helpful discussion at cyclic-polyacetylene system and thank Si-Ping Han for helpful suggestion. This project is funded by MARCO at UCLA.

Reference

1. W.K. Tommie, D.V. Muyres, P. F. Baude, T. P. Smith and T. D. Jones; *Mat. Res. Soc. Symp. Proc.* 771, L6.5.1 (2003).
2. T. Du1rkop, S. A. Getty, Enrique Cobas, and M. S. Fuhrer, *Nano. Lett.* 4, 35 (2004).
3. W.-Q. Deng and W.A. Goddard III "Predictions of Hole Mobilities in Oligoacene Organic Semiconductors from Quantum Mechanical Calculations" submitted and reference in.
4. Y. C. Cheng, R. J. Silbey, D. A. da Silva Filho, J. P. Calbert, J. Cornil, and J. L. Bre´das, *J. Chem. Phys.* 118, 3764 (2003)
5. (a) Burin, A. L.; Berlin, Y. A.; Ratner, M. A. *J. Phys. Chem. A* 2001, 105. (b) D. Raineri, F. O.; Friedman, H. L. *Adv. Chem. Phys.* **1999**, 107, 81. (c) Matyushov, D. V.; Voth, G. A. *J. Phys. Chem.* **1999**, 103, 10981. (d) Tavernier, H. L.; Kalashnikov, M. M.; Fayer, M. D. *J. Chem. Phys.* **2000**, 113, 10191. (e) Matyushov, D. V.; Voth, G. A. *J. Phys. Chem. A* **2000**, 104, 6470. (f) Tavernier, H. L.; Fayer, M. D. *J. Chem. Phys.* **2001**, 114, 4552.
6. J. L. Bredas, J. P. Calbert, D. A. da Silva Filho, and J. Cornil, *Proc. Nat. Aca. Sci.* 99, 5804 (2002).
7. A. Devos and M. Lannoo, *Phys. Rev.* 58, 8236 (1998).
8. V. Coropceanu¹, J.M. Andre, M. Malagoli and J.L. Bredas, *Theor. Chem. Acc.* 110, 59 (2003).
9. C. C. Mattheus, G. A. de Wijs, R. A. de Groot, and T. T. M. Palstra, *J. Am. Soc. Chem.* 125, 6323, (2003)
10. Kittel C. *Introduction to solid state physics* 7th edition
11. Ohyun Kwon and Michael L. McKee, *J. Phys. Chem. A* 104, 7106 (2000).
Bachtold A, Hadley P, Nakanishi T, Dekker C. *Science*, 294, 1317 (2001)

- Oyaizu K, Iwasaki T, Tsukahara Y, Tsuchida E *Macromolecules* 37, 1257-1270 (2004).
14. Gao, G.H.; Cagin, T.; and Goddard W.A.; *Nanotechnology*, 9, 184-191 (1998).
 15. Y. Kojima, T. Matsuoka, H. Takahashi, *J. Appl. Poly. Sci.*, 72, 1539, (1998)
 16. Kolmogorov AN, Crespi VH, Schleier-Smith MH, et al *Phys. Rev. Lett.* 92, art. no. 085503 (2004).
 17. B. R. Wegewijs and L. D. A. Siebbeles. *Phys. Rev.* 65, 245112 (2002).
 18. Jaguar 4.0 quantum mechanics program.. Schodinger Inc., Portland Ore.
 19. Supportive materials are available. It includes that structural information of all structures based on quantum calculation and force field calculation.

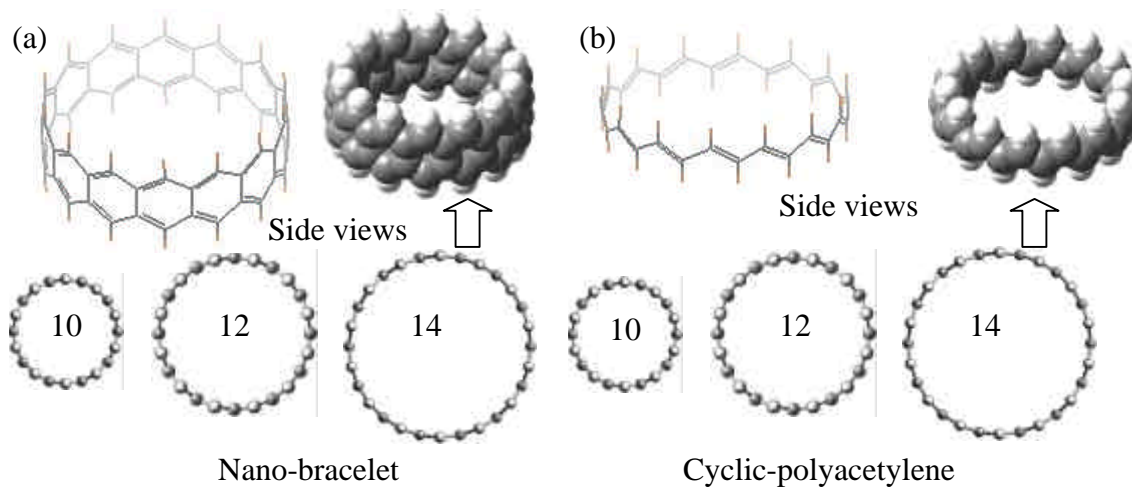


Figure 1. Proposed structures for seeking an ultra high hole mobilities. (a). The structures of nano-bracelet. (b). The structure of cyclic-polyacetylene, c-PA.

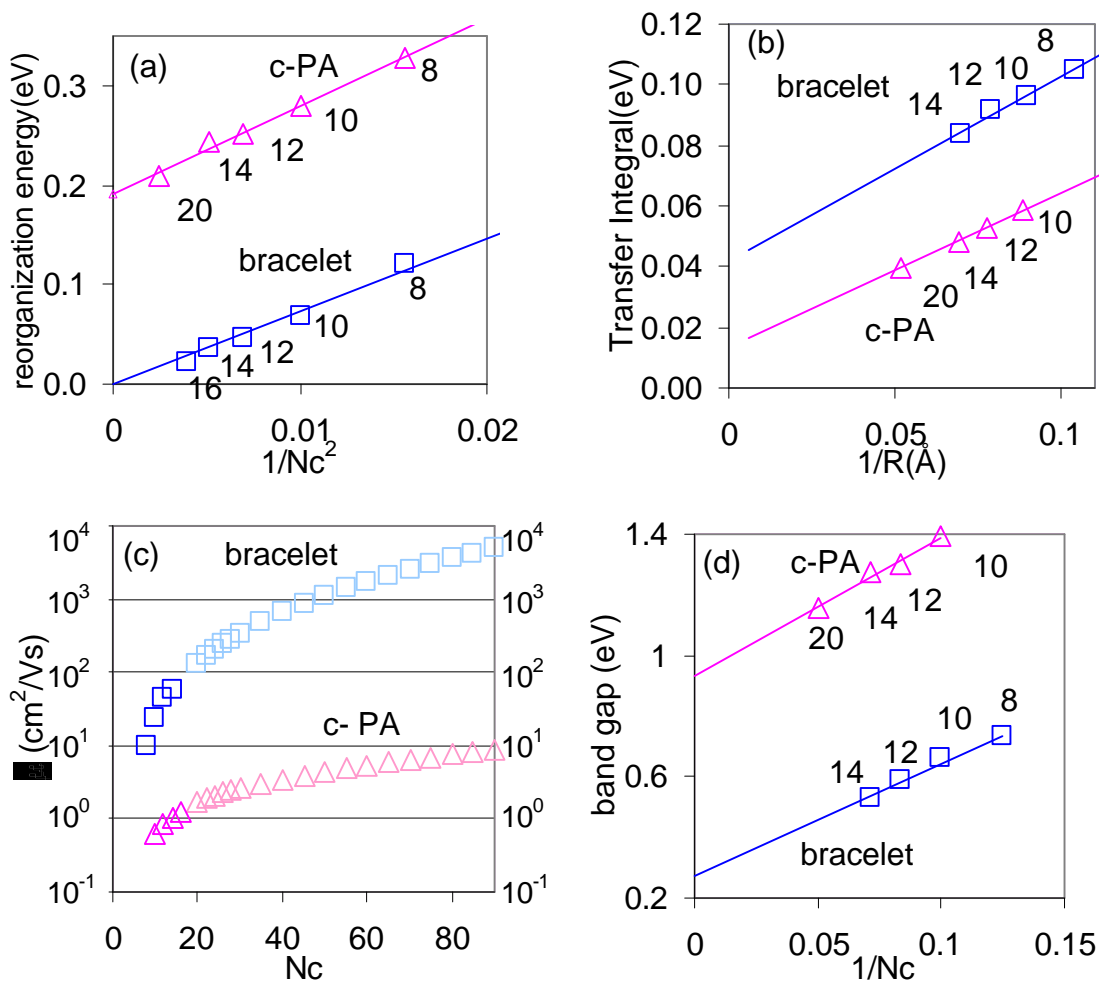


Figure 2. Predictions for nano-bracelets and c-PA. N_c is the number monomers of cyclic structures. The monomer is an aromatic ring C_4H_2 for bracelet system and C_2H_2 for c-PA. (a). The reorganization energy for bracelet system [$I(N) = 7.279/N^2$ (eV)] and for c-PA system [$I(N) = 8.782/N^2 + 0.192$ (eV)]. (b). The hole transfer integral for the bracelet system [$V(r) = 0.609/r + 0.042$ (eV)] and for the c-PA system [$V(r) = 0.509/r + 0.013$ (eV)]. Where R is the center mass distance between two adjacent molecules in 3D crystal structure. (c) The hole mobility for the bracelet and the c-PA system calculated from the fitted equations in (a) and (b). (d) Band gaps of the bracelet [$E_{band} = 3.712/N_c + 0.272$ (eV)] and the c-PA [$E_{band} = 4.573/N_c + 0.931$ (eV)].

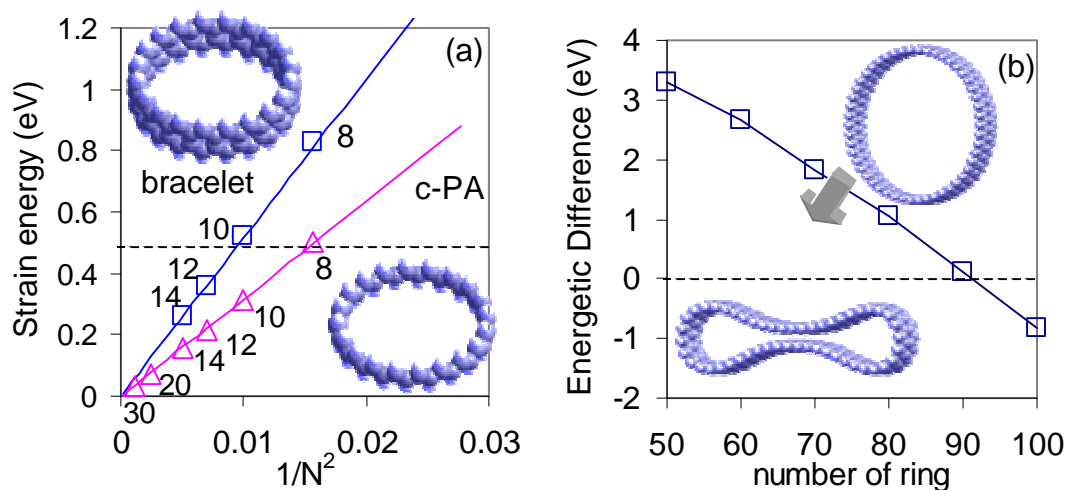


Figure 3. The strain energies and flexibilities of proposed nano-bracelets. (a). The strain energy of cyclic structures for bracelet and c-PA systems. The dashed line in picture shows the strain energy of a practical system c-PA with 8 monomers.[14] We conclude that with it is possible to make a bracelet with 12 or more monomer with less strain energy. (b). The energetic difference for converting the cyclic structures to flat structures of bracelet systems. The dashed line in picture shows that the bracelets with above 90 monomers prefer a flat structure.

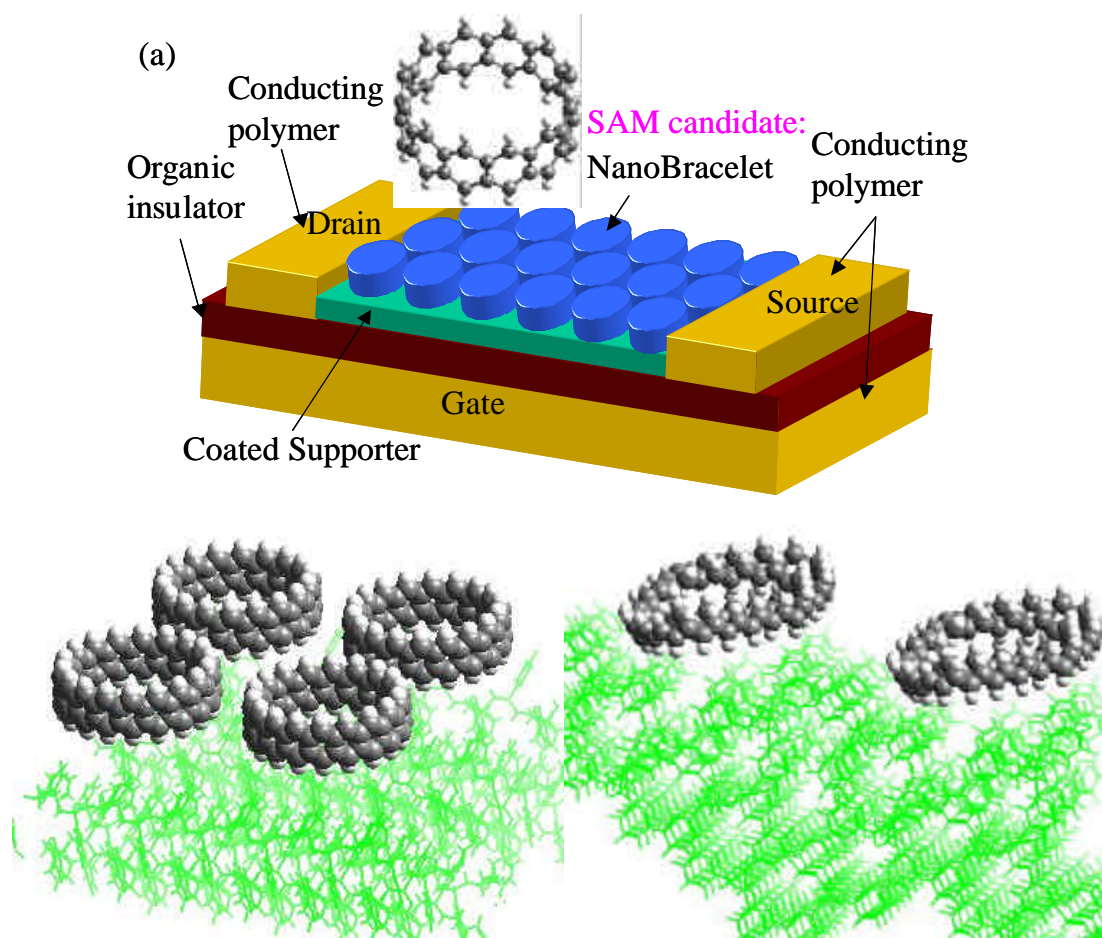


Figure 4. The scheme of soft organic transistor and the comparison of different candidates of the self-assembly monolayer (SAM). (a). Proposed fully organic transistor structures. (b). MD simulation of nano-bracelet SAM on the surface. (c). MD simulation of the c-PA SAM on the surface.

Supportive information

Calculation data of nanobracelet and related materials

Abstract Here we provide more details of calculation results in order to give reader more view of the materials mentioned in paper. Some results have not been discussed in text. We organize the supportive materials as below:

First section we list the quantum data calculated at B3LYP/6-31G** for all structures. Those data include energies, structural information and Mulliken charges. Second section, we list the crystal structure optimized by dreiding force field and the comparison with available experimental data. Third section, we gave more details at calculation of the band gap. Fourth section, we gave more details at calculating strain energy of bracelet and cyclic polyacetylene.

Section 1. Quantum calculation result of the structures

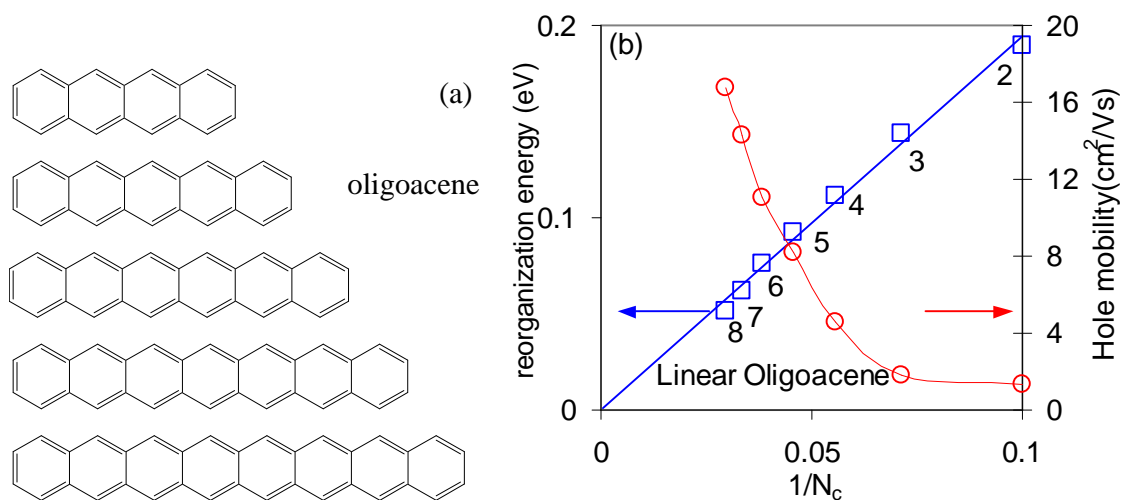


Figure S1. (a). The structures of oligoacenes. (b). The predicted reorganization energy and hole mobilities based on our model. The reorganization energy of oligoacene has been shown as inversely proportional to number of aromatic ring, obeying equation:

$$I = 1.946 / N \text{ (eV)}.$$

Table S1. The hole mobility of oligoacene and nano-bracelet. λ is the reorganization energy (eV), V is the coupling matrix element (eV), D is hole diffusion coefficient (cm²/s) and μ is the hole drift mobility (cm²/Vs).

	λ (eV)	T dimer CM	T dimer V (eV)	D (cm ² /s)	μ (cm ² /Vs)
Pentacene	0.0927	4.73	0.137	0.158	6.10 ^a
Hexacene	0.0764	4.88	0.170	0.3204	12.82
Heptacene	0.0623	4.89	0.151	0.3081	12.88
Octacene	0.0512	4.83	0.115	0.2105	8.99
Bracelet-8	0.1210	9.6	0.105	0.2528	9.78
Bracelet-10	0.0679	11.1	0.0960	0.6322	24.45
Bracelet-12	0.0460	12.7	0.0914	1.121	43.36
Bracelet-14	0.0357	14.3	0.0834	1.493	57.76

a. Experimental value: 5 cm²/Vs. refer.1

Table S2. Calculated energy of oligoacenes. VIP is Vertical Ionization Potential, λ is the reorganization energy (eV)

	Pentacene	hexacene	heptacene	8-acene
E ₀ (Hartree)	-846.8209	-1000.4571	-1154.0931	-1307.7295
E* (Hartree)	-846.8192	-1000.4557	-1154.0920	-1307.7286
E ₊ (Hartree)	-846.6040	-1000.2508	-1153.8949	-1307.5376
E ₊ * (Hartree)	-846.6024	-1000.2494	-1153.8937	-1307.5365
VIP(eV)	5.9073	5.6580	5.4316	5.2540
λ (eV)	0.0927	0.0764	0.0623	0.0512

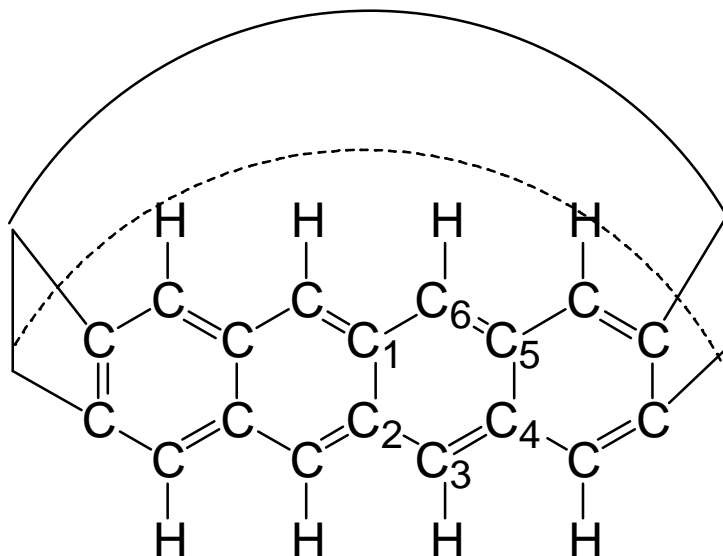
Table S3. Energetic of nanobracelet. VIP is vertical ionization energy. λ is reorganization energy (eV).

	8	10	12	14	16
E_0 (Hartree)	-1228.8469	-1536.1724	-1843.4795	-2150.7747	-2458.0633
E^* (Hartree)	-1228.8440	-1536.1713	-1843.4791	-2150.7745	-2458.0631
E_+ (Hartree)	-1228.6580	-1535.9875	-1843.2981	-2150.5964	-2457.8870
E_+^* (Hartree)	-1228.6565	-1535.9861	-1843.2968	-2150.5953	-2457.8863
VIP(eV)	5.1870	5.0730	4.9416	4.8849	4.8184
λ (eV)	0.1210	0.0679	0.0460	0.0357	0.0217

Table S4 Energy of c-PA. VIP is Vertical Ionization Potential, λ is the reorganization energy (eV)

	10	12	14	18	20
E_0 (Hartree)	-773.9940	-928.8366	-1083.6731	-1393.3365	-1548.1649
E^* (Hartree)	-773.9889	-928.8321	-1083.6691	-1393.3327	-1548.1612
E_+ (Hartree)	-773.8004	-928.6474	-1083.4879	-1393.1571	-1547.9879
E_+^* (Hartree)	-773.7952	-928.6427	-1083.4830	-1393.1528	-1547.9838
VIP(eV)	5.4151	5.1527	5.1767	5.0028	4.8220
λ (eV)	0.2803	0.2515	0.2433	0.2199	0.2094

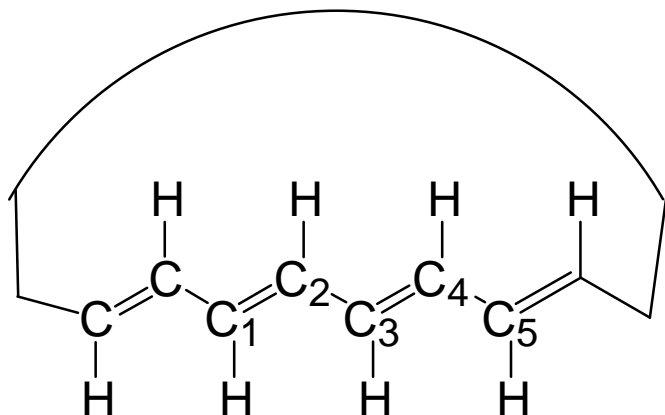
Table S5. Structural information at nano-bracelet



Each structures of nano-bracelet has typical three bonds; C_1-C_2 , C_2-C_3 and C_3-H .

Bracelet		Ring8	Ring10	Ring12	Ring14	Ring16
Point group		D_{8h}	D_{2h}	D_{6h}	D_{2h}	D_{8h}
Diameter (Å)	Neutral	6.368	7.912	9.471	11.033	12.594
	Cation	6.327	7.885	9.445	11.009	12.574
C_1-C_2 (Å)	Neutral	1.461	1.464	1.466	1.468	1.468
	Cation	1.461	1.464	1.466	1.468	1.468
C_2-C_3 (Å)	Neutral	1.412	1.410	1.409	1.408	1.408
	Cation	1.412	1.410	1.409	1.408	1.408
C_3-H (Å)	Neutral	1.088	1.088	1.088	1.088	1.088
	Cation	1.087	1.087	1.087	1.087	1.087

Table S6. Structural information of c-PA.



Each structure has three typical bonds: C₁-C₂, C₂-C₃ and C₂-H

c-PA		Ring10	Ring12	Ring14	Ring18	Ring20
Point group		D ₅	D ₆	D ₇	D _{6d} ^a	D _{4d}
Diameter ^b (Å)	Neutral	7.947	9.509	11.079	14.216	15.780
	Cation	7.900	9.464	11.030	14.166	15.732
C ₁ -C ₂ (Å)	Neutral	1.365	1.367	1.367	1.369	1.369
	Cation	1.382	1.382	1.382	1.381	1.382
C ₂ -C ₃ (Å)	Neutral	1.443	1.438	1.435	1.431	1.430
	Cation	1.422	1.419	1.417	1.415	1.414
C ₂ -H (Å)	Neutral	1.090	1.090	1.091	1.091	1.090
	Cation	1.089	1.089	1.090	1.090	1.090

a. D₂ for cation. b. average number

Section 2. Crystal structure minimized by dreiding force field with Mulliken charges.

Table S7. Crystal structures of linear oligoacenes by force field

oligoacene	5	5 exp	6	7	8
a	6.179	6.266	6.232	6.234	6.234
b	7.695	7.775	7.534	7.546	7.580
c	15.816	14.530	18.164	20.573	22.993
α	66.83	76.475	70.03	70.30	70.040
β	80.23	87.682	80.39	80.03	79.68
γ	86.18	84.684	86.38	86.36	86.23
Density	1.3566	1.3493	1.3800	1.4007	1.4165

Table S8. Crystal structures of nanobracelet by force field

bracelet	8	10	12	14
a	9.446	10.906	12.452	13.955
b	9.588	10.977	12.452	14.026
c	7.099	7.126	7.346	7.131
α	108.12	90.45	90.00	76.14
β	72.55	106.11	90.00	88.64
γ	121.40	120.17	120.00	120.06
Density	1.2939	1.1922	1.0113	1.0072

Table S9. Crystal structures of nanobracelet by force field

bracelet	10	12	14	18	20
a	10.60	12.413	13.601	16.934	18.788
b	11.21	12.202	14.132	16.761	18.094
c	5.11	5.109	5.116	5.118	5.122
α	90.00	102.08	90.00	98.78	98.13
β	76.05	90.00	79.16	90.00	90.00
γ	121.94	120.57	121.30	120.34	121.28
Density	0.8758	0.8029	0.7385	0.6308	0.5892

Section 3. The estimation of band gap

The band gap is estimated by the neighbor affection at the HOMO-LUMO splitting.

The method is described in Reference 15.

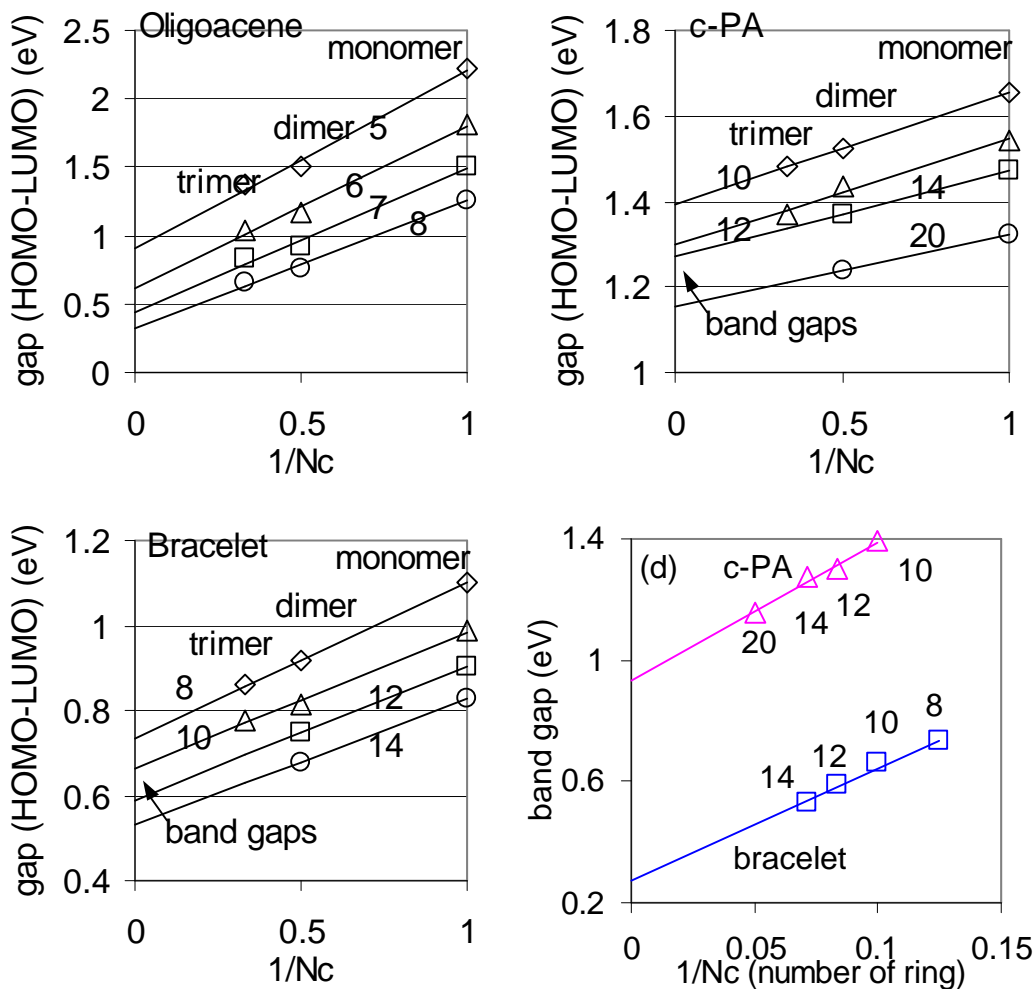


Figure S1. a) The band gap of oligoacenes, b) The band gap of cyclic poly-acetylene, c) the band of bracelet system. d) The figure shown in paper.

Figure S1 shows the method to estimate the band gap. The points in Figure 1a, 1b and 1c are QM calculation results. The curves are fitting results. The band gaps are estimated from the limited values of each curve. For example, from Figure 1c, the band gaps of bracelets are estimated as 0.54, 0.58, 0.64 and 0.73 eV for bracelet 14, 12, 10 and 8 respectively. Those data are shown as blue squares in Figure 1d.

Section 4. The calculation for the strain energy of c-PA and bracelet

If we assume that the energetic increasing from n to $n+1$ is $\Delta E_L = E_{n+1} - E_n$ for linear structure, thus the strain energy $E_{strain} = \frac{E_N}{N} - \Delta E_L$ where E_N is the energy of cyclic structure with N units. Table 10 and 11 listed the process how we calculated band gaps.

Table S10. The energetic of linear structures. (Hartree)

	Tetracene	Pentacene	Hexacene	Heptacene	Heptacene
Energetic	-693.1840	-846.8209	-1000.4571	-1154.0931	-1307.7295
$E_{n+1} - E_n$		-153.6369	-153.6362	-153.6360	-153.6363
ΔE_L Average	-153.6364				
Actylene	6	8	10	12	
Energetic	-465.6430	-620.4648	-775.2868	-930.1087	
$E_{n+1} - E_n$		-154.8218	-154.8220	-154.8219	
ΔE_L Average	-154.8219				

Table S11. The strain energy per monomer of cyclic structures.

Bracelet	8	10	12	14	
Energetic(Hartree)	-1228.8470	-1536.1724	-1843.4795	-2150.7747	
Strain(eV)	0.830	0.521	0.356	0.261	
c-PA	8	10	12	14	20
Energetic(Hartree)	-619.1408	-773.9940	-928.8366	-1083.6731	-1548.1649
Strain(eV)	0.500	0.314	0.215	0.156	0.074

Section 2: Nano-structured materials in Fuel Cell technology

Chapter VI: Simulation of Li-doped pillared carbon based materials for reversible hydrogen storage

Abstract	105
Introduction	106
Computational Details	107
Results and Discussions	108
Conclusion.....	115
Reference.....	115
Figures	118

Chapter VII: Fluorinated imidazoles as proton carriers for water-free fuel cell membranes

Abstract	132
Content	133
Reference.....	134
Figure.....	138
Support Information.....	140

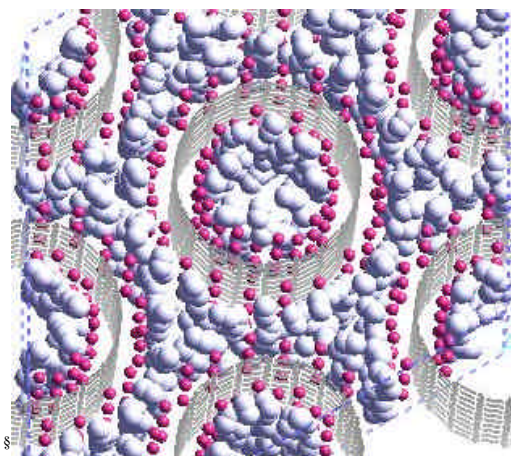
Chapter VI

SIMULATION OF LI-DOPED PILLARED CARBON BASED MATERIALS FOR REVERSIBLE HYDROGEN STORAGE ‡

Abstract

Based on grand canonical Monte Carlo (GCMC) simulation using a first principles-derived force field, we studied graphite and nanotube related systems to store hydrogen. Our investigation showed that Li doped pillared graphite or nanotube systems are good candidates to store large amount of hydrogen close to or even exceeding the DOE (Department of Energy) target of hydrogen storage. With an interlayer space of 10Å, the Li 1:3 doped graphite achieves its best performance for hydrogen storage. The method to modify the interlayers of graphite and nanotube are also discussed.

Figure for Table of Contents (Hydrogen storage in Li doped pillared nanotube).



‡ With Xin Xu's assistance at quantum mechanic calculations

I. Introduction

Nanostructured carbon materials, in the form of tubes [1-5], fibers [6-7] and mechanically milled graphite [8] have attracted considerable interest as a candidate for hydrogen storage. For example, Heben et al. found that single wall carbon nanotube (SWNT) soots can absorb about 6 to 8 mass % of H_2 at 133K [5]. Ye et al. used high-purity SWNTs and obtained 8.25 mass % of H_2 adsorption at 80K and 100 atm [3]. Browning et al. reported that 6.5 mass % hydrogen can be stored in carbon nanofibers under conditions of 12 MPa pressure and ambient temperature [7]. These H_2 uptake systems require either high pressure or very low temperature or both that limit the applicability for mobile applications that require working condition of roughly 1-10 bar and ambient temperature.

Chen et al. reported remarkable hydrogen-storage capacities of 20 mass % for Li-doped nanotubes at 653 K and 14 mass % for K-doped nanotubes at room temperature [9]. They also reported smaller but still significant absorptions in alkali-doped graphite (14 mass % for Li and 5 mass % for K) [9]. Unfortunately, later studies revealed that these high H_2 -uptakes were due to the impurity water gain/loss present in the hydrogen feedstream rather than to H_2 itself [10,11].

In this paper, we report here the simulation detail for proposing a new class of materials for reversible hydrogen storage designed to meet the criteria for transportation applications [12]. To validate our design we use a multiscale computational strategy, in which quantum mechanics (QM) at the X3LYP level of Density Functional Theory (DFT) [13] developed to accurately treat van der Waals interactions is used to determine an accurate force field (FF). We then use this FF with grand canonical Monte Carlo (GCMC) to determine the H_2 uptake as a function of pressure and temperature [14].

We organize this paper as follows: In section II, we describe the calculation methods. In section III we discuss the simulation results, which include several discussion topics such as hydrogen storage in carbon nanotube, Li ion interaction with hydrogen molecule, hydrogen storage in Li-doped materials and a strategy to synthesis the proposed materials. Section IV is a summary.

II. Computational Details

Classical pair potentials were used to model the van der Waals interactions in the Li dopant, carbon materials and hydrogen systems. To model the pair interaction, we used the familiar Morse potential

$$U_{ij}(r_{ij}) = D \left\{ \exp\left[\alpha\left(1 - \frac{r_{ij}}{r_o}\right)\right] - 2 \cdot \exp\left[\frac{\alpha}{2}\left(1 - \frac{r_{ij}}{r_o}\right)\right] \right\}$$

where r is the internuclear distance; the parameters D , r_0 and α are fitted to the accurate ab initio calculation results. For weak van der Waals interactions like H-H, C-H and C-C, the potential energies of clusters made up by two molecules were scanned by changing the internuclear distance. For H-H term, CCSD(T)/aug-cc-pVQZ was used to calculate the potential curve between two H_2 molecules [15]. The fitting force field was shown in Figure 1. For C-H cross term, MP4/aug-cc-pVTZ was used to calculate the interaction between H_2 and C_2 molecules, while a small basis set of bond functions was centered at the mid point between the molecules. The mid point basis function is well used to describe the weak van der waals interactions [16]. For strong van der Waals interactions between doped Li ion and hydrogen atoms, a large cluster $Li_2(C_{32}) + H_2$, representing the graphite and hydrogen molecule system, was scanned by X3LYP method. [13]

We used grand canonical Monte Carlo (GCMC) [14] to simulate the hydrogen storage process in our proposed materials to design a reasonable nanostructure to get the maximum hydrogen storage amount. In these simulations, the quantum effect was neglected because of the ambient conditions under consideration and the polarization effect is not expected to affect the results [17-18]. Thus, the classical force field was used to optimize the designed system for hydrogen storage. The nanotube's configuration was minimized by the force field developed for the carbon system [19]. The newly developed force field was used to replace van der waals interaction in the system. In order to obtain an accurate measure of H_2 loading, 1,000,000 configurations were used to compute the average loading for each condition. A finite three-dimensional cell that has 648 carbon atoms for the graphite cases

and 1140 carbon atoms for the carbon nanotube cases was used in the simulations where periodic boundary conditions were applied in order to minimize undesirable surface effects.

III. Results and Discussion

Graphite and nanotube hydrogen storage

Accurate determination of the hydrogen storage amount in carbon based materials depends upon H_2 - H_2 and carbon - H_2 interactions. To validate the first principles derived force field, we performed several simulation cases to show the accuracy of the force field. To test the H-H interactions we simulated H_2 density by GCMC where a vacuum 3D box is used to contain hydrogen molecules. The comparison between the fitting Morse and the accurate ab initio potential [15] is shown in Figure 1. Different configurations of $(H_2)_2$ give different potential curves. The global minimum is reproduced reasonably well by the Morse potential; while the results for configuration (60,60,0) or (0, 0, 0), where (q_1, q_2, j) are defined in Figure 1a, are less satisfactory. However, the Morse potential gives an overall accurate H_2 density as compared to the experimental result. Figure 2a and 2b show that these simulation results are in good agreement with experiment values [20] at 10M Pa and 0.1M Pa.

To test the C-H term we simulated hydrogen storage in a pure nanotube bundle. Figure 3 shows a comparison of the ab initio calculation to the force field fitting. Then the fitting parameters are employed to describe hydrogen storage in a 7-nanotube bundle shown in Figure 4a, which is created to model Ye's experimental system [3]. Experimental nanotube materials have 285 m^2/g Brunauer-Emmett-Teller (BET) surface; while, comparably, the model system with 7 nanotube bundles has 158 m^2/g theoretical surface by assuming that the van der waals radii of carbon atom is 0.16nm. Our simulation results show that the amount of hydrogen uptaking is from 2.3 % to 4.4 % at the pressure range between 10 bar-70 bar under 80 K temperature. These results are in reasonable agreement with Ye's experiment which postulated that hydrogen is physically adsorbed in the carbon nanotube. Unfortunately, when the temperature is increased to room temperature, the amount of uptaking dramatically decreases towards 1 %, which agrees with the value reported in

Hirshcher's experiment [2] but disagrees with 8 % reported in Heben et al's experiment [4]. Heben et al. explained that the high uptaking may be caused by chemisorption rather than physisorption. However, so far no theoretical investigations can really support the postulate that chemisorption in nanotubes occurs at ambient condition.

The first idea to improve the hydrogen storage would be to modify the interlayer distance of graphite or the intertube distance of carbon nanotubes so as to provide more storage space in the materials. We investigate the hydrogen storage in pillared graphite and nanotubes. The results are shown in Figure 5. With increasing of the interlayer distance from equilibrium distance to 12 Å, the hydrogen storage amount will increase from 0 % to 0.6 % for graphite and from 0.2 % to 0.64 % for nanotube under 50 bar 300 K. The improvement is noticeable comparing with graphite or nanotube in the equilibrium geometry. However, it is still far below the storage amount even under super-high pressure. These simulations also indicate that those efforts [21,22] to improve the hydrogen storage by separating interlayer distance of graphite or carbon nanofibers (which is considered as amorphous graphite) is not optimistic.

Li ion interaction with hydrogen molecules

We notice that the presence of an alkali cation X^+ in an H_2 environment gives rise to a positively charged core, resulting from the interaction of X^+ with the nearby H_2 molecules, followed by a clustering of other H_2 molecules around this core [23]. Figure 6 shows the heats of formation of $Li^+-(H_2)_n$ via the reaction $Li^+ + n H_2 \rightarrow Li^+-(H_2)_n$. The heats of formation for the first H_2 molecule is 5.39 kcal/mol by MP4/6-311G* calculation, 4.3 kcal/mol for the second H_2 molecule and 4.07 kcal/mol for the third (Curve in blue)[14]. We noticed that the widely used B3LYP significantly under estimate the bonding (Curve in red), leading the heats of formation for the first H_2 4.0 kcal/mol, 3.8 kcal/mol for the second and 3.0 for the third H_2 molecule. Curve in purple is calculated using X3LYP functional developed especially for van der Waals interaction. The X3LYP values compare well with the MP4 ones [13], i.e., 5.12 kcal/mol for the first H_2 molecule, 4.47 kcal/mol for the second and 3.90 kcal/mol for the third. Thus X3LYP is used to calculate the interaction between hydrogen molecule and Li doped graphite systems which are too large system for

the MP4 calculation. X3LYP calculations show that each Li ion can adsorb up to 6 H₂ molecules and thus Li ion doped materials should have large potential to take-up ideal amount of hydrogen. Carbon-based materials, e.g., graphite, carbon nanotube, carbon fiber, are good materials to maintain Li ion because these materials have large electron affinity and make stable complexes with the Li ion.

Figure 7a shows energetic points of a hydrogen molecule bind with the Li doped carbon cluster calculated by the X3LYP method. The force field fitting is in good agreement with the quantum curve. All those force field parameters are listed in Table 1. X3LYP method predicted that the binding energy is around 4.0 kcal/mol for the first hydrogen molecule adsorption, 2.6 kcal/mol for the second hydrogen molecule and 3.0 kcal/mol for the third hydrogen molecule as shown in Figure 7b. The attempt to look for a structure with four hydrogen molecules binding to Li doped cluster failed. H₂ still maintains its molecular form in the cluster, i.e., H-H bond is 0.743 Å, comparable to 0.748 Å in free H₂ molecule. The first point in Figure 7b shows that the formation of the Li-H chemical bond will require at least 82.3 kcal/mole comparing to the molecular adsorption cases. This energy cost is so high that the H-H bond breaking is not feasible under ambient conditions.

This calculation leads to an optimistic estimation that the hydrogen storage for Li doped carbon materials may reach 7.1 mass % with 1:6 Li:C doping concentration. Next, we will discuss Li doped graphite and carbon nanotube systems.

Hydrogen storage in Li doped carbon nanotube and graphite

In order to increase the hydrogen storage capacity, we considered adding Li to the graphite and SWNTs. Our reasoning was that the high electron affinity of the sp² carbon framework would separate the charge from the Li, providing strong stabilization of the molecular H₂. We first considered a Li-doping concentration of Li:C=1:6, which corresponds to the most stable conformation of Li-GIC (graphite intercalated compound) at ambient conditions. Figure 8 shows the results for Li doped graphite and SWNTs at different pressures. It shows that Li doped graphite does not exhibit hydrogen storage capacity, in agreement with the experimental observation of Pinkerton, et al [11]. Li doped

SWNTs leads to ~1.2 mass % hydrogen storage at 1 bar, which increases to ~2.0 mass % at 50 bar. Here 99.5 % of the storage comes from the space inside the nanotubes shown in Figure 9. These results suggest an explanation for the differences observed between different experiments [10,11]. Pinkerton [11] found no observable hydrogen storage capacity for Li-doped nanotubes, but they used closed-end nanotubes that would prevent H₂ from entering the tubes. Yang [10] made nanotubes by chemical vapor deposition followed by purification with strong acid, which will cut off the nanotube caps, allowing H₂ to go inside. They found ~2.5 mass % hydrogen storage for Li-doped nanotubes at 1 bar and ambient temperature. This is consistent with our results of 1.2 mass % at the same conditions. The small discordance here might be because we considered the infinite crystal with no surfaces, whereas the experiments probably had substantial surface area that might increase the net storage. We conclude that Li-doped SWNT do exhibit modest hydrogen storage capacity at ambient conditions, but not enough to meet the DOE requirements for transportation. Consequently we will explore below how the hydrogen storage can be increased with additional Li doping and modified nanostructures.

Hydrogen storage in Li doped pillared carbon graphite and nanotube

Based on the discussion above, we designed two series system: (1) Li doped pillared graphene sheets (Li-PGS), and (2) Li doped pillared single wall carbon nanotube (Li-P-SWNT).

As the most popular Li doping concentration for graphite and nanotube, we first study 1:6 Li/C doping pillared graphite and carbon nanotube. Figure 8 shows the hydrogen storage amount in Li doped pillared graphite and carbon nanotubes is extremely improved than the pure pillared graphite and carbon nanotubes. In Figure 8a, hydrogen storage amount can reach 2.5 % even at 1 bar and room temperature as the pillared distance is 12 Å, which is more than 100 times comparing with the pure pillar graphite at same condition in Figure 5a. We noticed the negative results from Pinkerton's experiments of about 0 % hydrogen uptaking for Li doped graphite[11]. That is true because the interlayer space is too small to contain any hydrogen molecules. The Li doped pillared graphite will increase the space between graphene layers, thus will remove this spatial limitation. The same is

true for the Li doped pillared carbon nanotube. The slight difference is that Li doped carbon nanotube will have 1.8 % hydrogen storage at 1 bar and room temperature. That is understandable because all the hydrogen stored is in the inner space of the carbon nanotube. Because in the Li 1:6 doped carbon nanotube and graphite systems, the doped Li acts as core to attach hydrogen molecules, the hydrogen storage amount can be improved more if the doping concentration is increased.

To determine the maximum feasible Li doping concentration of graphite or carbon nanotube, we performed several DFT calculations to identify the best doping concentration of the Li-graphite system. In these calculations we employed the CASTEP [24] periodic QM software using the Perdew GGA II density functional combined with a plane-wave basis set. The geometries of Li-doped graphite or Li doped pillared graphite at various doping concentrations were fully optimized. We used a kinetic energy cutoff of 380eV for the plane wave basis set. We used the default convergence criteria that correspond to 0.0002 eV for the energy change per atom, 0.001 Å for the rms atomic displacement and 0.05 eV/Å for the rms residual force.

Figure 10a shows that at the equilibrium interlayer distance (3.4 Å) Li doped graphite is most stable for Li:C = 1:6, and Li:C = 1:8, in agreement with experimental observation.[25] However, for Li-doped pillared graphite, Li:C = 1:3 is the most stable structure with interlayer distance larger than 8 Å. Experiments also shows that it is possible to get Li:C=1:3 doped graphite and carbon nanotube. [26] We conclude that the Li:C = 1:3 doping concentration should be a feasible system to consider. Figure 10b shows that the hydrogen storage amount versus the Li doping concentration when the interlayer distance is 10 Å. At 1 bar 300K, the hydrogen storage can reach 5.6 % for Li:C 1:3 doped graphite. By increasing the pressure, the hydrogen uptaking can be improved to 6.5 % at 20 bar. This result is promising as no other materials can have such a storage amount at such conditions. Although Li:C 1:2 doping graphite can have higher hydrogen uptaking amount, 6.0 % at 1 bar, 7.1 % at 20 bar, Li:C 1:3 doping graphite is more favorite structure by considering the energetic curve at Figure 10a.

By changing the interlayer or inter-tube distance, we simulate the best performance of Li:C 1:3 doped graphite and carbon nanotube. Both the hydrogen uptaking mass % and hydrogen density are regarded as criterions. For the Li:C 1:3 doped graphite, the interlayer distance 10 Å will be the best structure that has 6.5 mass % hydrogen uptaking and 62.9 kg/m³ hydrogen density at 20 bar room temperature, while DOE target of hydrogen storage materials is 6.5 mass % and 62 kg/m³ at ambient condition. The interlayer distance 9 Å may give higher hydrogen density 69.1 kg/m³ but the mass percentage is lower (6.4 %). On the other hand, higher interlayer distance 12 Å leads to similiar hydrogen uptaking 6.5 % but lower hydrogen density 52 kg/m³. The DOE target could be surpassed to 6.7 mass% and 65.8 kg/m³ with an operating pressure of 50 bar.

Similarly, the structure with the inter-tube distance equal 9 Å may be the best structure for Li doped carbon nanotube. This structure can lead to 6.0 mass % and 58.7 kg/m³ at room temperature and 50 bar, which is close to DOE target. Figure 11 summarizes the results.

To obtain reversible hydrogen uploading and unloading, we propose to use temperature and pressure switching to control the process. In Figure 12, the hydrogen uptaking amounts versus temperature at different pressure are presented. The reversible hydrogen storage amount can be obtained by changing the pressure and temperature to reach the target. For example in Figure 12a, a system of Li:C = 1:3 with interlayer = 10 Å reaches 6.5 mass % hydrogen uptake under loading conditions of 20 bar and 300 K. Under the unloading conditions of 0.01 bar and 400 K, the residual hydrogen is 0.2 mass %. Therefore, the total load/unload will provide 6.3 mass % reversible hydrogen. If the pressure can be increased beyond 50 bar, the total load/unload can provide 6.5 mass % reversible hydrogen. This is far superior to any other hydrogen storage systems proposed up to now. Figure 12b shows that the Li:C=1:3 doped carbon nanotube will have a less hydrogen storage amount than the Li doped graphite. However, the working circle from 50 bar, 300K to 0.01 bar, 500K can lead to 5.4 mass % reversible hydrogen that is still very good comparing with known materials at such a working condition.

Proposed synthesis strategy for Li doped graphite

Ball milling has been established to effectively increase the Li-doping concentration and is ready to extend to the industrial scale [27]. There is also experimental evidence that the interlayer distance of graphite intercalated compound can be expanded. It was proved that ether type organic ligands can bind to alkali metal ions and co-intercalate into the host carbons so that the interlayer distance of graphite can be expanded from around 3.4 Å to 8.7-12.4 Å [28]. We believe that the same co-intercalation synthesis method can be extended to SWNT systems to expand the inter-tube distances.

Figure 13 proposes a possible scheme to synthesize a practical hydrogen storage system:

(1) Ternary compounds are first produced by the reaction between host carbons and 2,5-dihydrofuran solvated Li cation in low concentration such that the interlayer spaces of graphite are expanded;

(2) A Diels-Alder type reaction between the organic solvents and the graphite sheets is triggered to build covalent bonds that would maintain the interlayer space under operating conditions;

(3) Li-intercalation and proper ball milling are used to synthesize doped pillared graphite of higher Li concentration.

We have tested this process with computer simulations. For Li:C =1:3, we considered one pillar per 116 carbons and find interlayer distance = 8.0 Å to be optimal. Carrying out GCMC calculations on this system we find 5.7 mass % hydrogen storage at 300 K and 50 bar. For maximum performance the pillar should be modified to yield interlayer distance = 10 Å.

IV. Conclusion

In summary, we have designed a series of new materials for H₂ storage: Li doped pillared graphene and Li doped pillared nanotubes. We have tested and optimized the nanostructure of these Li-doped carbon materials using grand canonical Monte Carlo

simulations with a first principles-derived force field, We predict that for 1:3 Li:C doping and interlayer distance = 10Å, Li-pillared graphene will lead to hydrogen storage of 6.5 mass % and 62.9 kg/m³ at 20 bar and room temperature, attaining the DOE target. We find that Li doped pillared SWNT (1:3 Li:C doping and intertube distance = 9 Å), can lead to hydrogen storage capacity of 6.0 mass % and 58.7 kg/m³ at 50 bar and room temperature storage, which is close to DOE target. We also suggest ways to synthesis these systems by co-intercalation of solvated Li ion followed by Li-intercalation and ball milling.

ACKNOWLEDGMENT This work was supported by General Motors Corporation (Dr. Gerald Voecks). The facilities of the Materials and Process Simulation Center (MSC) used in these studies were funded by DURIP (ARO and ONR), NSF (CTS and MRI), and a SUR Grant from IBM. In addition, the MSC is funded by grants from ARO-MURI, NIH, ChevronTexaco, General Motors, Seiko-Epson, the Beckman Institute, Asahi Kasei, and Toray Corp.

Reference:

- [1] Schlapbach, L. and Zuttel, A., Nature 2001, 414, 353 and reference in.
- [2] Hirscher, M.; Becher, M.; Haluska, M. and et al Appl. Phys. A 2001, 72, 129
- [3] Ye, Y.; Ahn, C.C.; Witham, C.; Fultz, B. and et al. Appl. Phys. Lett. 1999, 74, 2307
- [4] Dillon, A.C.; Jones, K.M.; Bekkedahl. T.A.; Kiang, C.H. and et al. Nature 1997, 386, 377
- [5] Liu, C.; Fan, Y.Y.; Liu, M.; Cong, H.T.; Cheng, H.M. and Dresselhaus, M.S., Science 1999, 286, 1127; Fan, Y.Y.; Liao, B.; Liu, M.; Wei, Y.L.; Lu, M.Q. and Cheng, H.M., Carbon 1999, 37, 1649
- [6] Ahn, C.C.; Ye, Y.; Ratnakumar, B.V.; Witham, C.; Bowman, R.C. and Fultz, B. Appl. Phys. Lett. 1998, 73, 3378

- [7] Browning, D. J.; Gerrard, M. L.; Lakeman, J. B.; Mellor, I. M.; Mortimer, R.J. and Turpin, M.C., *Nano Lett.* 2002, 2, 201.
- [8] Orimo, S.; Meyer, G.; Fukunaga, T.; Zuttel, A.; Schlapbach, L. and Fujii, H., *Appl. Phys. Lett.* 1999, 75, 3093
- [9] Chen, P.; Wu, X.; Lin, J. and Tan, K.L., *Science* 1999, 285, 91
- [10] Yang, R.T. *Carbon* 2000, 38, 623
- [11] Pinkerton, F.E.; Wicke, B.G.; Olk, C.H.; Tibbetts, G.G.; Meisner, G.P.; Meyer M.S. and Herbst J.F., *J. Phys. Chem. B* 2000, 104, 9460
- [12] Deng, W.Q.; Xu, X.; and Goddard III, W.A. *Phys. Rev. Lett.* 2004, 92, 166103.
- [13] Xu, X. and Goddard III, W.A.; *P. Natl. Acad. Sci. USA* 2004, 101 2673.
- [14] The GCMC calculations were carried out using the sorption module of Cerius2 (Accelrys, San Diego)
- [15] Diep, P.; Johnson, J. K. *J. Chem. Phys.* 2000, 112, 4465.
- [16] Tao F.M. *J. Chem. Phys.* 1993, 98, 3049
- [17] Williams, K.A. and Eklund, P.C., *Chem. Phys. Lett.* 2000, 320, 352
- [18] Cracknell, R. F. *Phys. Chem. Chem. Phys.* 2001, 3, 2091.
- [19] Gao, G.H.; Cagin, T.; Goddard, W.A., *Phys. Rev. Lett.* 1998, 80, 5556.
- [20] CRC physical and chemistry hand book
- [21] US patent 5,653,951, Rodriguez; N. M. and Baker; R.T. K.
- [22] Orimo, S.I.; Matsushima, T.; Fujii H. and et al. *Molecular Crystals and Liquid Crystals* 2002, 386, 173

- [23] Barbatti, M.; Jalbert, G. and Nascimento, M.A.C., *J. Chem. Phys.* 2001, 114, 2213
- [24] For these calculations we employed the CASTEP periodic QM software (from Accelrys) using the Perdew GGA II density functional combined with a plane-wave basis set.
- [25] Abe, T.; Mizutani, Y.; Kawabata, N.; Inaba, M. and Ogumi, Z., *Syn. Metals* 2002, 125, 249.
- [26] Shimoda, H. and et al., *Phys. Rev. Lett.* 88, 0155021 (2002); Zhao, J and et al., *Phys. Rev. Lett.* 85, 1706 (2000)
- [27] Janot, R. and et al., *Carbon* 39, 1931 (2001)
- [28] Inagaki, M.; Tanaike, O.; *Carbon* 2001, 39, 1083.

Table 1. Force Field parameters based on quantum mechanics for GCMC simulations.

Van Der Waals	Functional Form	Well depth (kcal/mol)	Equilibrium distance (Å)	β
C	Morse	0.099	3.9940	10.963
H	Morse	0.0181	3.5698	10.709
C-H	Morse	0.0359	3.7443	12.168
Li ⁺ -H	Morse	2.1575	2.0180	7.125
Li ⁺ -C	Morse	4.350	2.5100	5.009

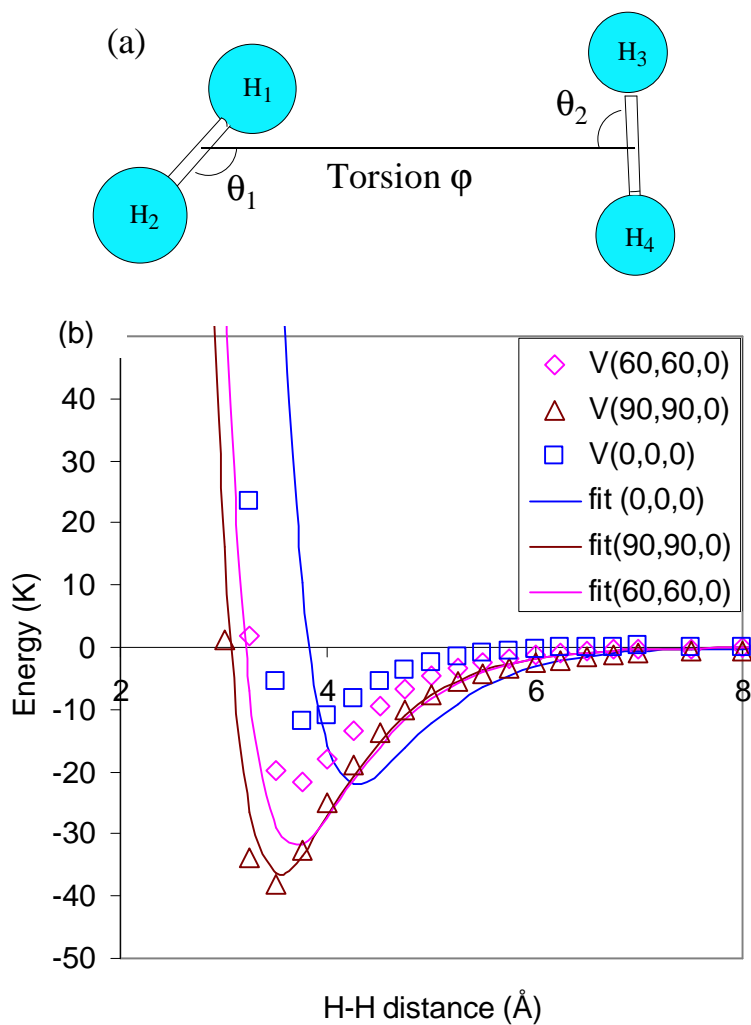


Figure 1 The comparison between force field calculation and quantum calculation results. (a) The definitions of $V(\theta_1, \theta_2, \varphi)$ where V is potential surface. (b) The potential curve from the quantum calculation and from force field. The quantum calculation is based on CCSD(T)//aug-cc-pVQZ.

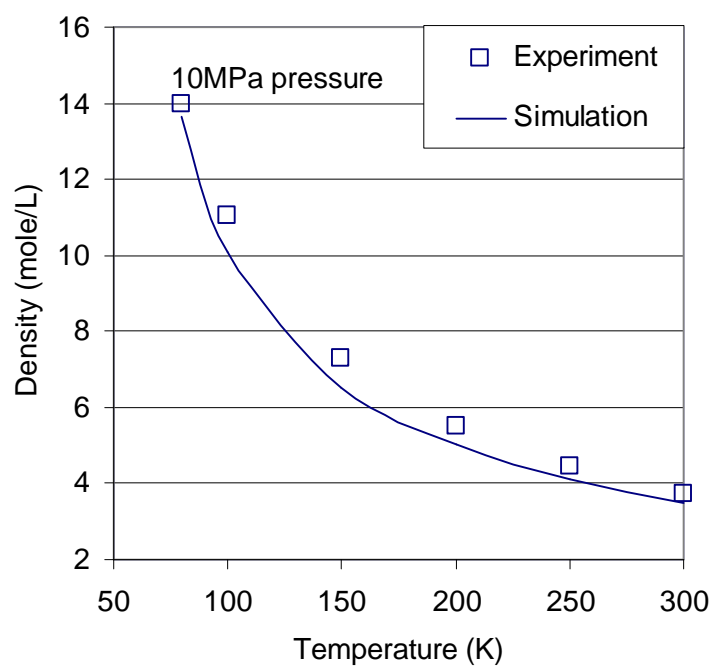
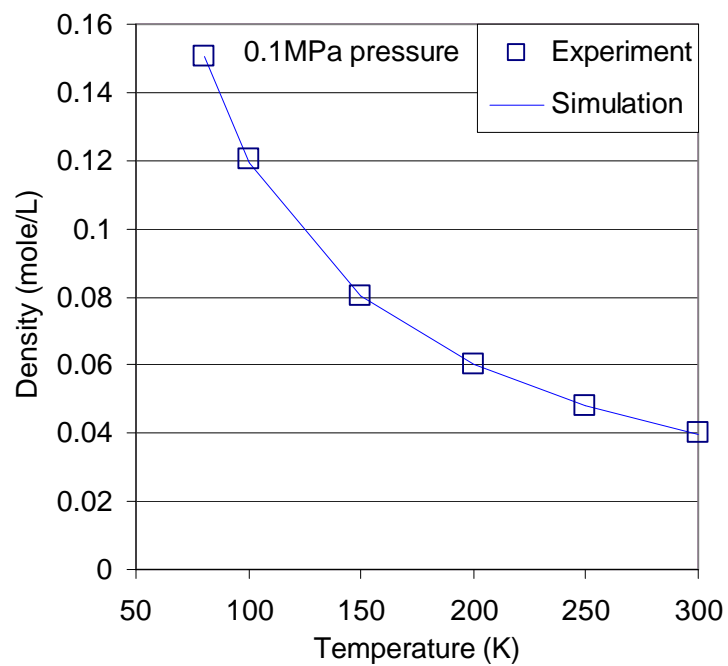


Figure 2. Simulated hydrogen gas density as compared with the experimental data. (a) at 100 bar. (b) at 1 bar.

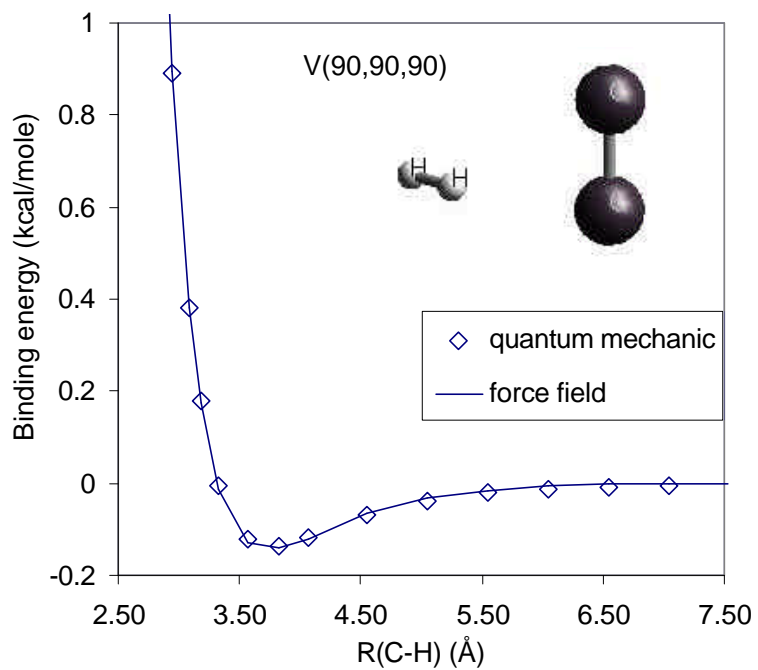


Figure 3. The force field fitting for the C-H cross term van der Waals interaction.

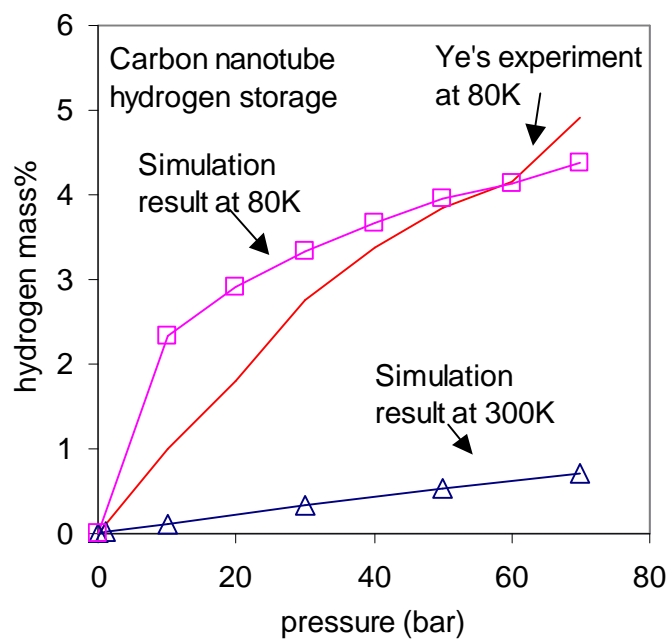
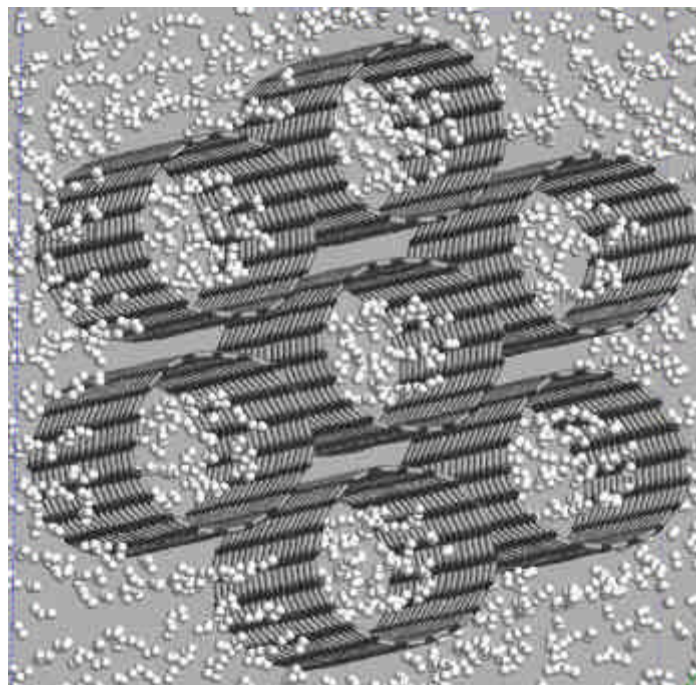


Figure 4. Hydrogen storage in carbon nanotube bundles. (a) hydrogen uptaking in carbon nanotube bundles; (b) comparison between simulation and the experimental results.

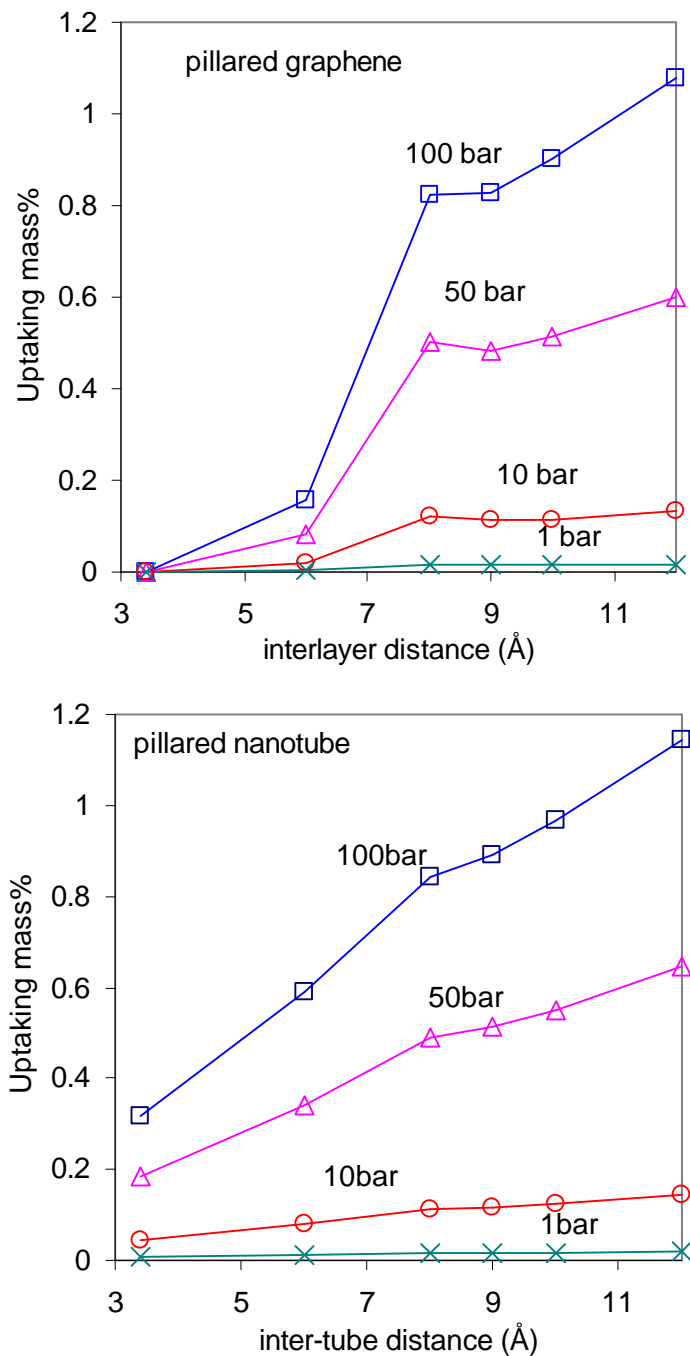


Figure 5. Hydrogen storage of pillared graphite and nanotube. (a) Pillared graphite. (b) Pillared carbon nanotube.

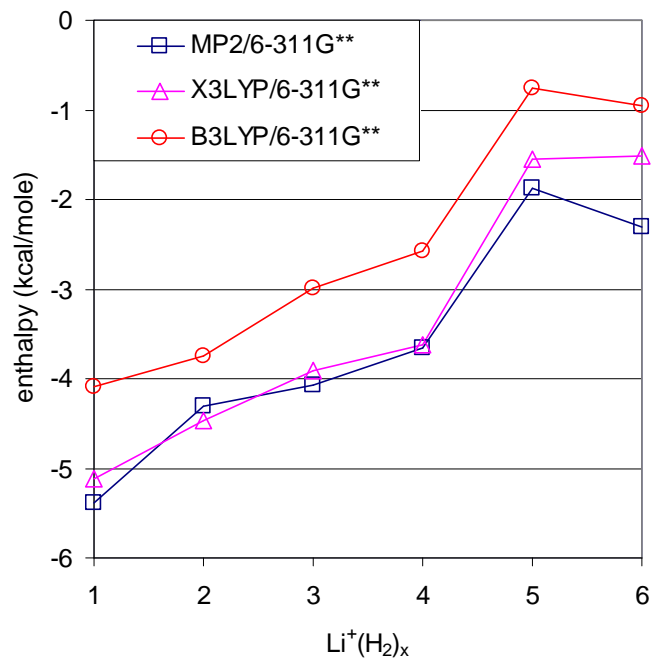


Figure 6. Heats formation of $\text{Li}^+(\text{H}_2)_n$ complexes. Comparison of MP2/6-311G**, X3LYP/6-311G** and B3LYP/6-311G**.

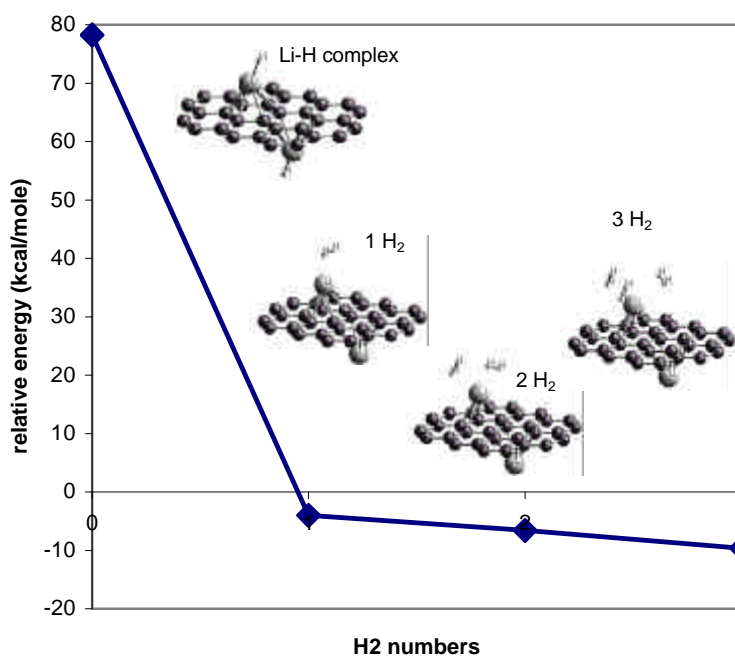
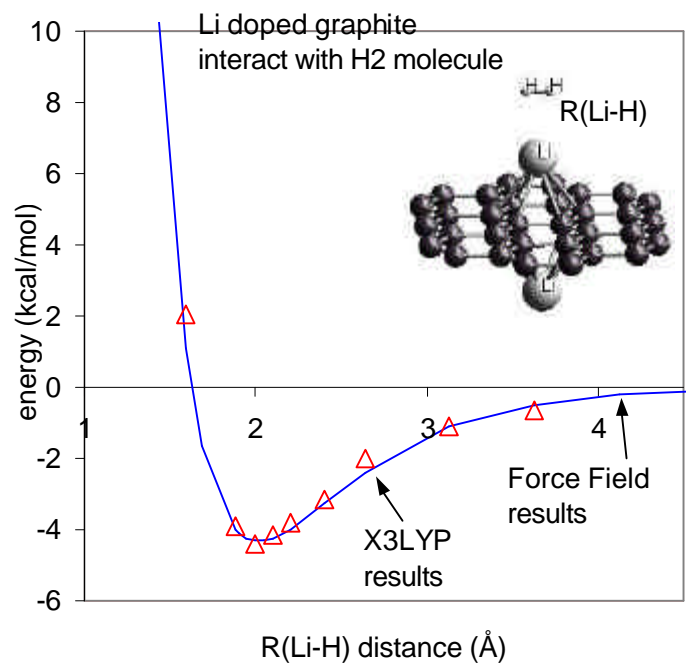


Figure 7. H₂ adsorption on Li doped carbon cluster. (a) Force field fitting to the quantum calculation curve. (b) hydrogen molecules binding with Li doped cluster.

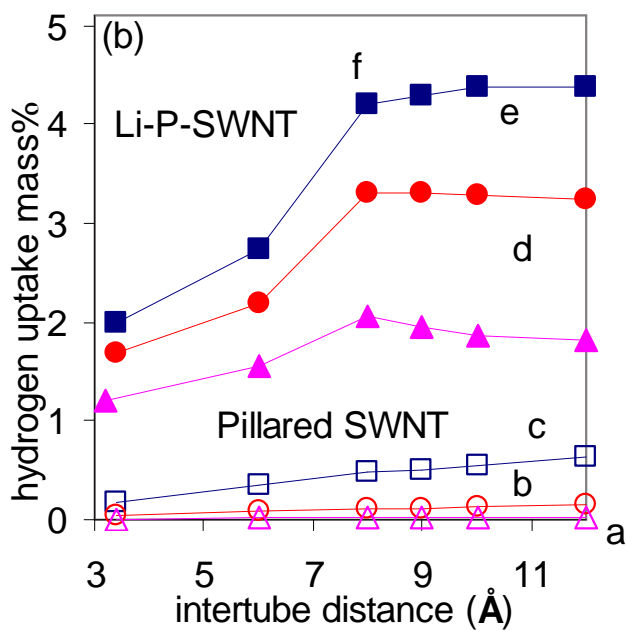
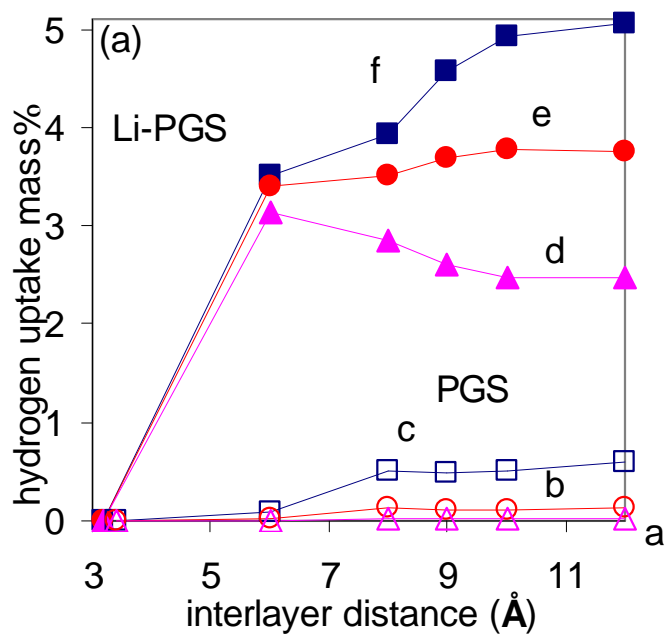


Figure 8. Hydrogen storage in Li 1:6 doped graphite and nanotube after being pillared. (a) Li doped pillared graphite sheet (PGS) (b) Li doped pillared carbon nanotube

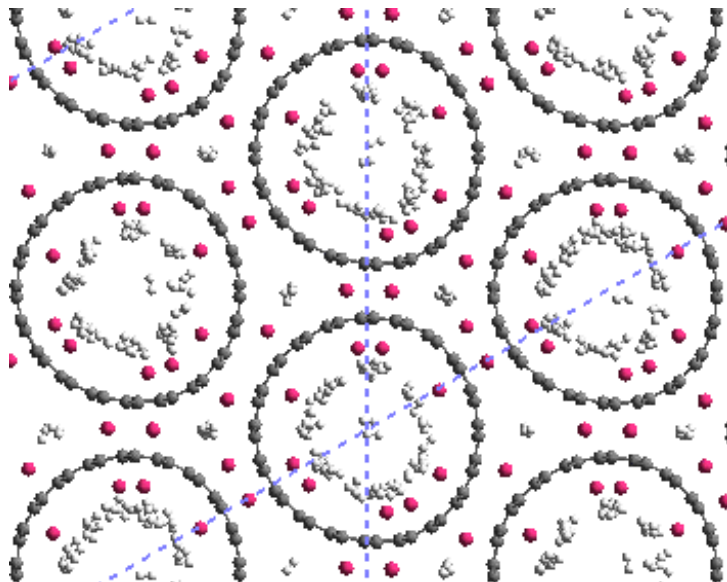


Figure 9. Hydrogen storage in Li doped carbon nanotube with equilibrium intertube distance.

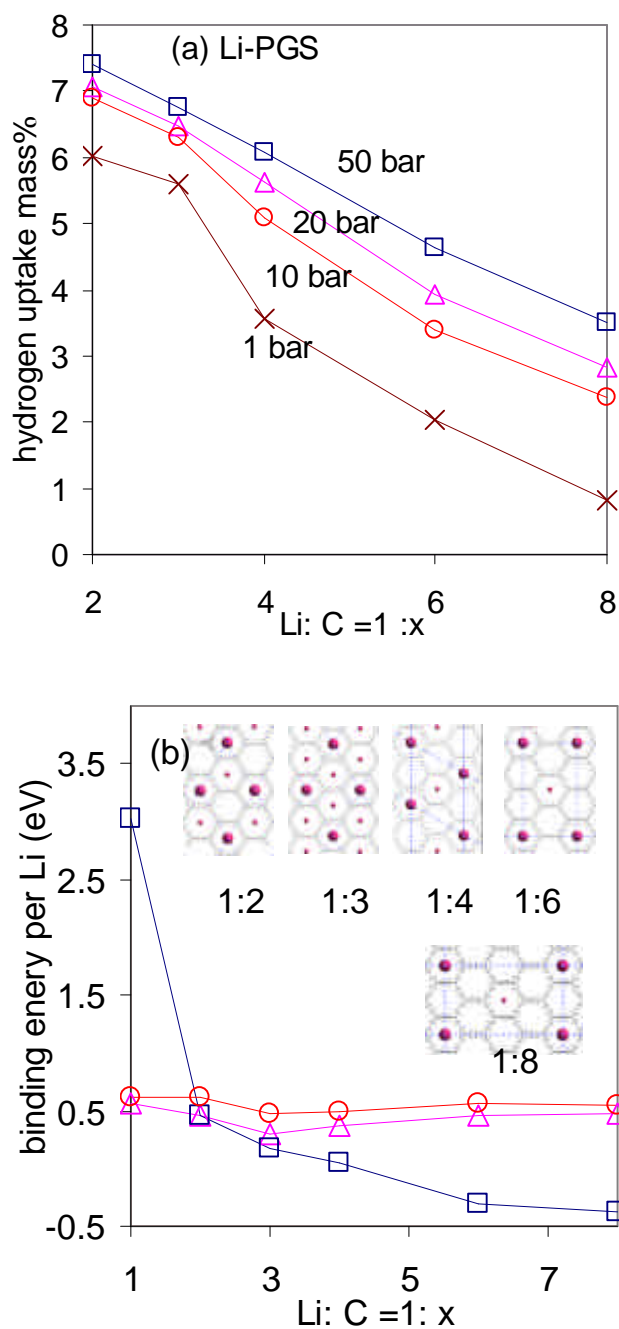


Figure 10. (a) Effects of Li-doping concentration on the mass hydrogen storage capacity under various pressures. (b) Binding energy per Li atom under various Li-doping concentrations. Key: square = equilibrium interlayer distance; circle = interlayer distance 8 Å; triangle = interlayer distance 10 Å. The zero energy reference responds to pure graphite crystal and pure Li metal.

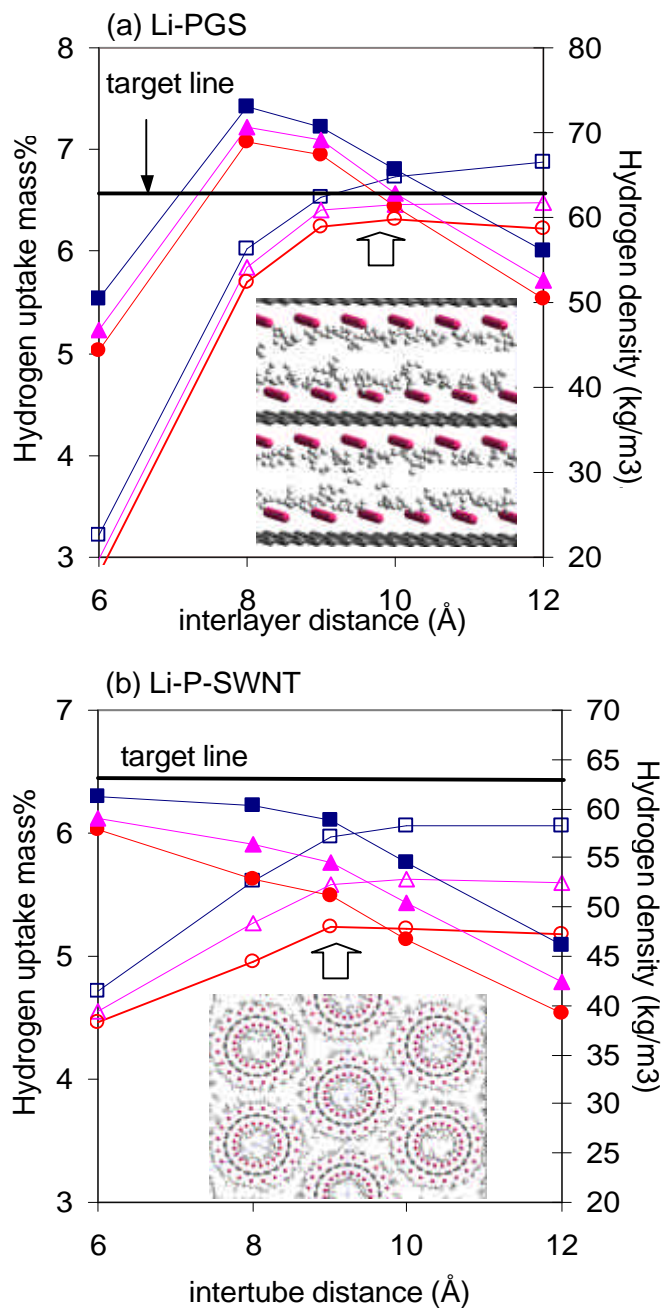


Figure 11. Optimization of nano-structures of (a) Li-Doped graphite and (b) Li-doped SWNTs systems for mass (white) and volumetric (black) hydrogen storage capacities. The Li-doping concentrations are Li:C = 1:3. The DOE target is shown by a line. The optimum interlayer or inter-tube distance is indicated by an arrow. Key: square = 50 bar; circle = 20 bar and triangle = 10 bar.

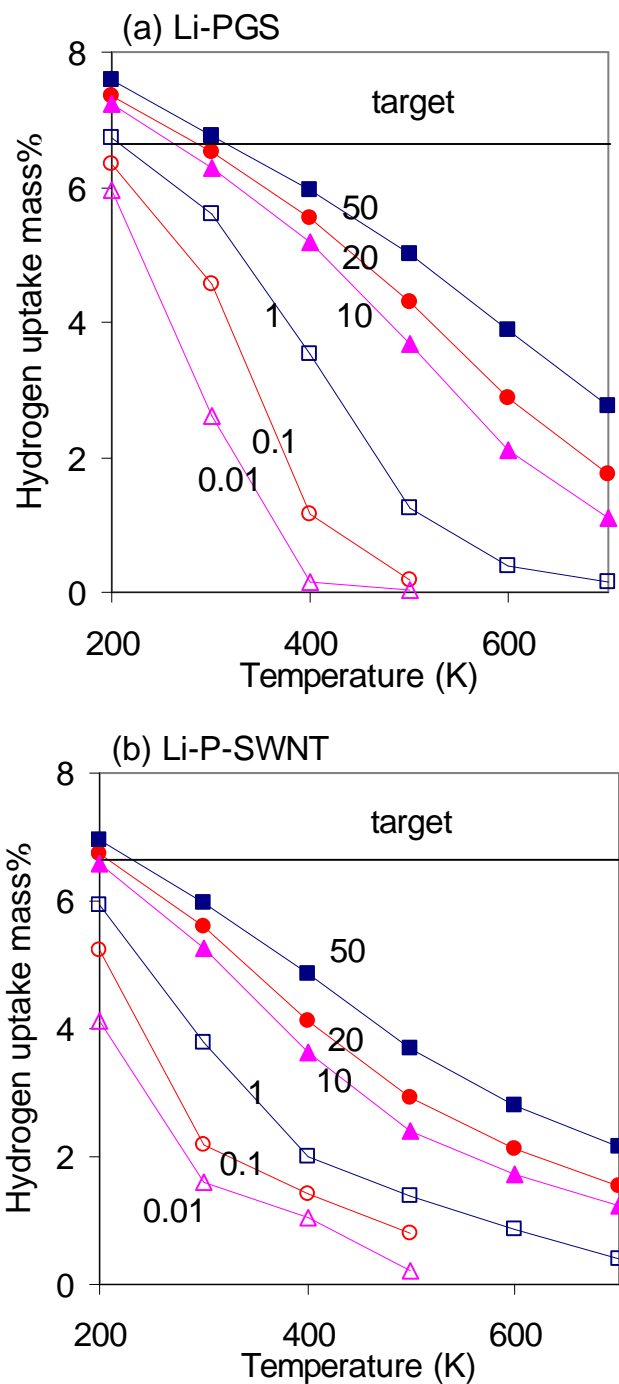


Figure 12 Temperature and pressure effects on the mass hydrogen storage capacity. (a) Li-DPG: Li:C = 1:3 and interlayer distance = 10 Å; (b) Li-doped pillared SWNTs: Li:C = 1:3 and inter-tube distance = 9 Å.

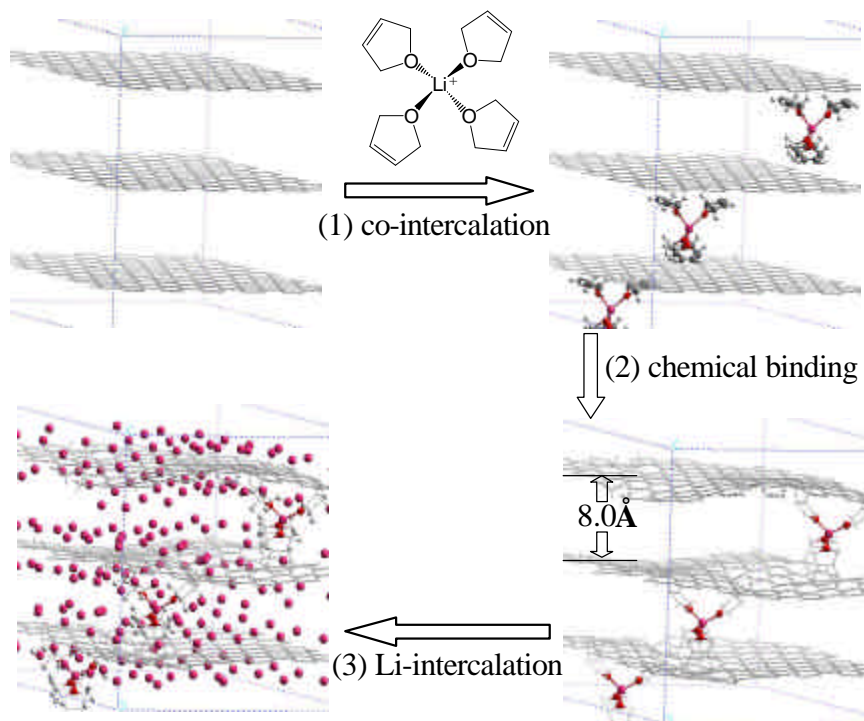


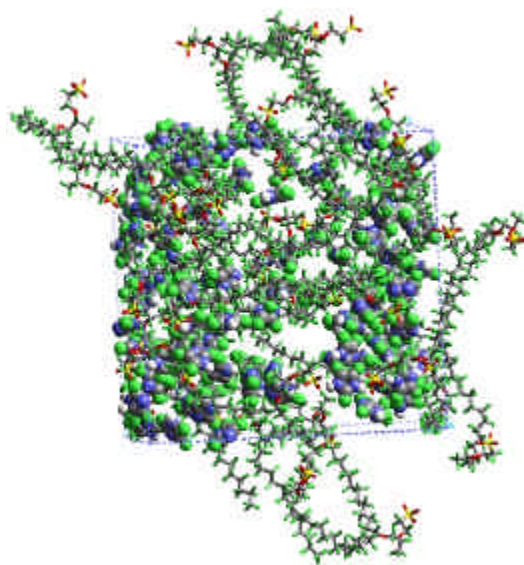
Figure 13. A scheme to synthesize the Li doped pillared graphene or nanotubes of high Li-doping concentrations and large interlayer distances.

*Chapter VII*FLUORINATED IMIDAZOLES AS PROTON CARRIERS FOR WATER-FREE
FUEL CELL MEMBRANES**

Abstract

We propose an alternative material (2,4,5-trifluoroimidazole impregnated Nafion) for use as a high temperature water-free membranes for proton exchange membrane fuel cells. This material has been tested computationally using MD and QM techniques, leading to an estimated conductivity of ~ 0.06 S/cm at 177°C . This material overcomes the weaknesses of the imidazole impregnated perfluorinated sulfonic acid membranes, which poisons the Pt electrodes. We find that 2,4,5-trifluoroimidazole weaken the binding to platinum surface, so that poisoning is not expected.

Figure for the table of Contents (imidazole impregnated nafion for proton exchange membrane).



* With Valeria Molinero's assistance at kinetic model development and MD trajectory analysis.

The quest for clean and efficient sources of electric power has intensified the research on proton exchange membrane fuel cells (PEMFC) in the last decade. The high conductivity of hydrated Nafion membranes, along with their chemical and mechanical stability, makes them favorites in applications with temperature of operations up to 80°C. At higher temperatures, this membrane steadily releases water, with a concomitant decrease in proton conductivity.[1] Higher temperatures of operation are desirable, however, to enhance the rate of the reaction at the Pt electrodes and more critical to avoid the poisoning of Pt by adsorption of CO, present as impurity in the feeding gases for the fuel cell. CO poisoning can be avoided if the electrode operates at $T > 120^\circ\text{C}$.[2] Therefore, the development of membranes with good proton conductivity and that can operate above 120 °C with Pt electrodes had become a principal goal of fuel cell research. Alternative water-free materials, such as organic-inorganic composite membranes [3], and blends of different polymers with phosphoric acid⁴, had been tried for PEMFC in that intermediate temperature range. However, none can satisfy the high proton conductivity and chemical stability requirements for fuel cell applications.

Imidazole (Im) is a heterocyclic molecule containing two N atoms, allowing it to pick a proton on one of the N and deliver the H from the other N site. Its high boiling point (257 °C [5]) makes it a good candidate to replace water as proton carrier in intermediate temperature PEMFC.[6-8] The conductivity of recast Nafion membrane with ~10%wt imidazole at 160-180°C was found to be ~0.1 S/cm, as high as that of 100% humidity Nafion at 80°C.[1] Notwithstanding the excellent proton conductivity of the recast Nafion-imidazole membrane, it was discarded for fuel cell applications because imidazole poisons the Pt electrode.[8]

In this communication we propose using 2,4,5-trifluoroimidazole (ImF3) as the proton carrier for water-free Nafion membranes operating above 120°C. We have carried out Quantum Mechanics (QM) and Molecular Dynamics (MD) simulations indicating i) that the ImF3 does not adsorb significantly on Pt, and ii) that the proton conductivity of ImF3/nafion membranes is comparable to that of Im/nafion.

Using DFT QM methods (GGA PW91), we find that the strong adsorption of Im to Pt (111) surface is responsible for poisoning of the electrode ($D_e=21.1$ kcal/mol binding energy). However, for ImF3 we find $D_e=1.3$ kcal/mol. [The details of the calculations are in the Supporting Information (SI)]. Similar calculations for CO/Pt(111) lead to $D_e = 38.5$ kcal/mol (exp. 42.3 ± 6.7 kcal/mol⁹), and for H₂O/Pt(111) lead to 11.0 kcal/mol (exp. 12.5 kcal/mol¹⁰), indicating that this level of calculation is adequate. Figure 1 shows the lowest energy configuration of the imidazole on the Pt surface; the adsorbate heterocyclic ring is perpendicular to the surface. In this configuration, the sp^2 lone pair of the N binds to a surface Pt atom. The effect of fluorination is to reduce the electronic density in the sp^2 lone pair orbital of the N, decreasing the binding energy to just 1.3 kcal/mol for ImF3. The Pt-N bond length illustrates the same trend increasing from 2.1 Å for Im, to 2.4 Å for ImF3. This result shows that perfluorination of the imidazole ring would prevent the poisoning of the Pt electrode by weakening the Pt-N bonds.

Now the question is whether the fluorination of imidazole will slow down the proton transport in the Nafion matrix. In water, protons are transported through two different mechanisms: the diffusion of protonated water molecules (vehicular diffusion) and the hopping of the proton along sequences of water molecules (Grothuss diffusion). Accurate MD methodologies, such as hybrid ab-initio MD^[11] and classical multistate empirical valence bond model^[12] have been used to compute proton diffusion. Their application of proton transport in realistic PEMFC, however, is limited in the first case by the size of the systems to be simulated, and in the second for the existence of a high concentration of protonated species. To estimate the total mobility we use the trajectory from classical MD calculations on a realistic model of the Nafion membrane^[13] and estimate both the vehicular mobility and the nonvehicular mobility from the same trajectory. We do this considering both a) imidazole (Im) and b) trifluoroimidazole (ImF3) as the proton carrier, in a proportion of 3 heterocyclic molecules per sulfonate. Details of the systems and simulations can be found in the SI. The temperature (177°C) and concentration of imidazole in Nafion (15%wt) were selected to be close to the experimental values for the recast membrane.⁸ We estimate the proton diffusion D in the carrier/nafion system as the sum of two contributions: a vehicular diffusion coefficient D_v and a hopping diffusion

coefficient D_H . The vehicular contribution was computed from the slope of the mean square displacement of the proton carrier (ImH^+ or ImF3H^+) with time in the equilibrated MD trajectories, $D_V = \overline{\dot{\mathbf{a}}^2(t)} / 6t$.

To compute the hopping diffusion in the membrane, we first parameterized the rate constant for the transfer of a proton from the protonated to the neutral carrier as a function of the intermolecular donor and acceptor N-N distance, using transition state theory [14]

$$k_{ij}(r) = \mathbf{k}(T, r) \frac{k_B T}{h} \exp\left(-\frac{E_{ij}(r) - 1/2 h \mathbf{w}(r)}{RT}\right)$$

where the tunneling factor k is given in ref. 14 and $E(r)$ is the energy barrier for the proton to be transferred from donor to acceptor, while they are at a distance r . We used QM to calculate the proton hopping barriers for imidazole and trifluoroimidazole. The hopping barriers depend strongly on the distance r between the proton donors and acceptor, as can be seen in Figure 2a, but not significantly on the fluorination of the carrier

We computed the probability P_{ij} for the proton to jump from each protonated carrier i to any the neutral one j , and average over all protonated carriers along the MD trajectories to obtain D_H

$$D_H = \frac{1}{6Nt} \int_0^{t \rightarrow \infty} \sum_i^N \sum_j^M k_{ij} r_{ij}^2 P_{ij} dt$$

Table 1 lists the estimated proton diffusion coefficients $D = D_H + D_V$ in the (fluorinated) imidazole-Nafion membranes at 177°C, and their contributions D_H and D_V .

Our calculations indicate that the ImF3/Nafion membrane has a proton conductivity ~60% that of Im/Nafion one. Since the specific conductivity of Im/Nafion is $S = 0.1$ S/cm at 177 °C, we expect ImF3/Nafion to have $S \sim 0.06$ S/cm, making it a good candidate for fuel cell applications. The vehicular contributions are comparable for the two membranes. The 40% decrease in the hopping contribution to the transport for ImF3 arises mainly from the decrease in the probability of close donor/acceptor distances (see Figure 2b). This decrease

arises because replacement of H by bulkier F atoms decreases the number of pairs at the close distances where the proton hopping mechanism is more effective.

It has also been argued [15] that the proton transfer in imidazole is limited by the reorientation of the molecule. We computed the characteristic reorientational times τ_R for ImH⁺ and ImF₃H⁺ in the Nafion membrane from the decay of the first order autocorrelation function $C_1(t)$ for the intramolecular NN vector. We find that the characteristic rotational time for ImF₃ is 20% smaller than for Im (89 versus 113 ps; see SI). Thus if this were the limiting factor, the decrease in mobility would be just 20%, rather than the 40% we calculated considering proton transfer as the limiting step.

In summary, we have demonstrated using QM and MD simulation methods that the perfluorination of the proton carrier in imidazole/Nafion membranes would solve the problem of electrode poisoning, while still providing a high proton conductivity.

Acknowledgment We thank Seung Soon Jang for his help with the Nafion model. The facilities of the Materials and Process Simulation Center are supported by ONR-DURIP, ARO-DURIP, SIR-IBM, DOE (ASI ASAP), NSF (CHE), and additional support is provided by DOE-ASCI, DOE-FETL, MURI-ARO-MURI, MURI-ONR-MURI, NIH, NSF, General Motors, ChevronTexaco, Seiko-Epson, Beckman Institute and Asahi Kasei.

Supporting Information Available: Computational methods and detailed results.

References

- (1) Steele, B. C. H.; and Heinze, A.; *Nature* 2001, 414, 345-352 and references in.
- (2) Ianniello, R.; Schmidt, V. M.; Stimming, U.; Stumper, J.; Wallan, A. *Electrochim. Acta* 1994, 39, 1863.
- (3) Alberti, G.; Casciola, M. *Annu. Rev. Mater. Sci.* 2003, 129 and references therein.
- (4) Schuster, M. F. H.; Meyer, W. H. *Annu. Rev. Mater. Sci.* 2003, 233 and references therein.

- (5) CRC Chem Phys. Handbook
- (6) Schuster, M.F.H.; Meyer, W.H.; Schuster, M.; et al, Chem. Mater. 2004, 16, 329-337 and references therein.
- (7) Kreuer, K. D. Solid State Ionics 1997, 97, 1-15.
- (8) Yang, C.; Costamagna, P.; Srinivasan, S.; Benziger, J.; Bocarsly, A. B. J. Power Sources 2001, 103, 1-9.
- (9). Yeo, Y. Y.; Vattuone, L.; and King, D. A.; J. Chem. Phys. 1997, 106, 392.
- (10) Thiel, P. A.; Madey, T. E. Surf. Sci. Rep. 1987, 7, 211
- (11). Hammes-Schiffer, S. and Tully, J. C.; J. Chem. Phys. 1994, 101, 4657-4667. Hammes-Schiffer, S. and Tully, J. C.; J. Chem. Phys. 1995, 103, 8528.
- (12). Day, T. J. F.; Soudackov, A. V.; Cuma, M.; Schmitt, U. W.; Voth, G. A. J. Chem. Phys. 2002, 117, 5839-5849. Iyengar S.S., Burnham C.J., Petersen M.K., Voth G.A. Comput. Sci. Eng. 2003, 5, 31-35.
- (13). Jang, S.S; Molinero, V.; Cagin, T.; Goddard III, W. A. J. Phys. Chem. B 2004, 108, 3149-3157.
- (14). Lill, M. A.; Helms, V. J. Chem. Phys. 2001, 115, 7985-7992.
- (15) Munch, W; Kreuer, K.D; Silvestri, W; Maier J; Seifert, G; Solid State Ionics, 2001,145, 437-443.

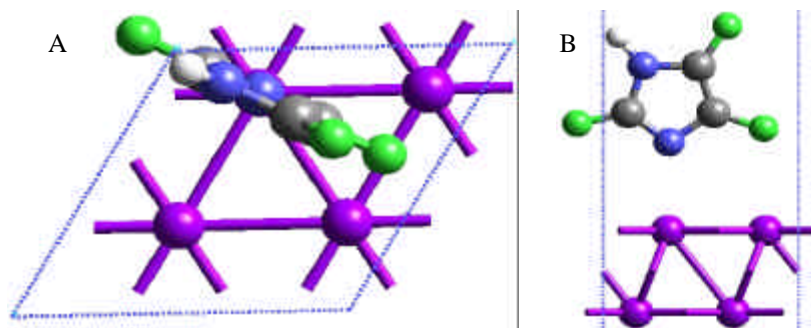


Figure 1. QM optimized structure of 2,4,5-trifluoroimidazole on Pt. A) Top view of the periodic cell displaying only the upper layer of Pt atoms. B) Side view. ImF3 binds through N to a top position in the Pt surface.

Table 1. Simulated Proton diffusion coefficient of nafion/imidazole complex.

	T (K)	$D_V^{(a)}$	$D_H^{(a)}$	$D^{(a)}$
Nafion+imidazole	450	0.15	1.60	1.75
Nafion+3F-imidazole	450	0.12	0.88	1.00

a) Diffusion coefficients in $10^{-5} \text{ cm}^2/\text{s}$.

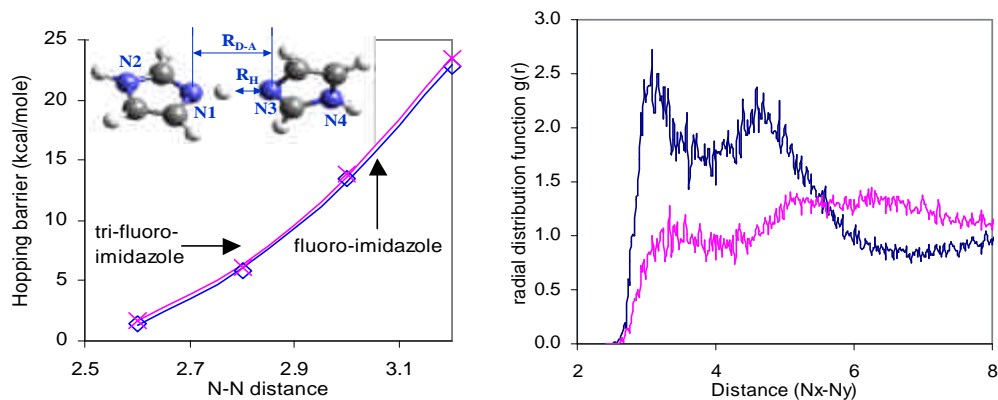


Figure 2. (a) Barriers for the proton transfer between imidazole/ imidazolium (blue) tri-fluoroimidazole/ tri-fluoroimidazolium (pink) at representative donor/acceptor N-N distances. The largest difference in the hopping barriers is less than 0.7 kcal/mol. (b). Radial distribution function $g(r)$ between donor and acceptor N sites of imidazole (blue) and trifluoroimidazole (pink) nafion membranes. The perfluorination decreases the number of close donor/acceptor neighbors.

Supporting information

Computational methods and detailed calculation results

Abstract

We organized this supporting material as follows: Section 1 describes the calculation method and detailed calculation results for Pt electrode poisoning problems, and Section 2 describes the methodology employed to estimate the proton diffusion in the imidazole/nafion and trifluoroimidazole/nafion membranes.

1. Pt electrode poisoning problem.

In order to study the poisoning of platinum in the presence of imidazoles, we used CASTEP [1] to calculate the binding energy between imidazole derivatives and platinum surface. A periodic slab that includes two layers of platinum totalizing 8 atoms was used to describe Pt (111) surface. The unit cell c parameter was set to be 16\AA at z direction for keeping 50% of the unit cell as vacuum in order to avoid any interaction between slabs. The calculations were performed by using nonlocal density functional theory (DFT) with the generalized gradient approximation (GGA-II) [2] and periodic boundary conditions. We used the norm-conserving plane wave pseudopotentials generated with the optimization scheme of Lin et al. [3] We found significant changes in relative energetics for cutoffs up to 600 eV, requiring a cutoff of 940 eV to obtain convergence. We found that a k -point sampling of $2\times 2\times 1$ was sufficient for convergence. All energies were extrapolated to 0 K using the correction technique of Gillan and De Vita.[4] All calculations were performed with the CASTEP code in the CERIUS2 software package.[1]

As comparison, we also studied the CO and H₂O adsorbed on the platinum surface. Figure S1 shows all detailed structures optimized by CASTEP program.

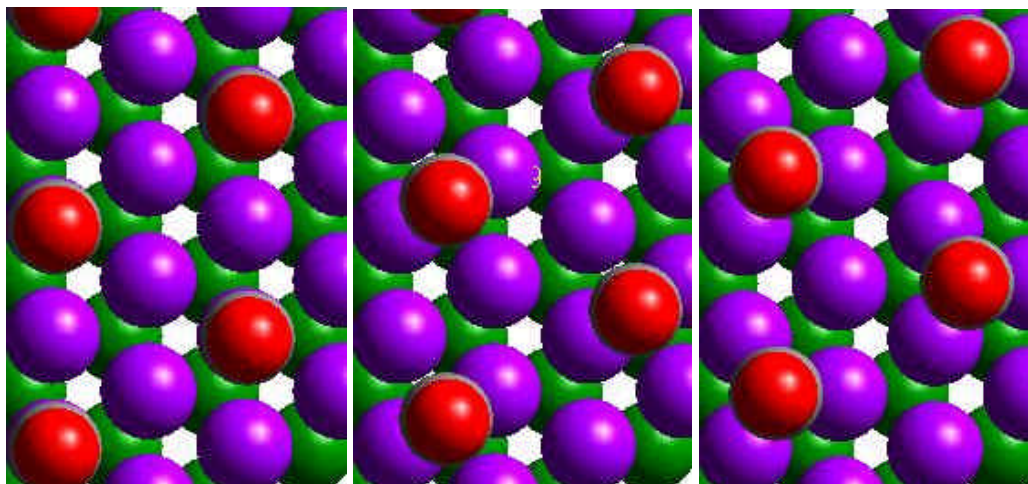


Figure S1. Structures of CO bind with Platinum 111 surface. a) top b) bridge, c) fcc hollow site. Pink atom is first layer Pt, Green is second layer Pt atom, red is oxygen atom, gray is carbon atom.

Table S1. Comparison of adsorption energies for CO on Pt computed in the current work with experimental results and other simulation results. (E in kcal/mole)

Energy functional	Top position	Bridge position	Three fold hollow
GGAI ^a	38.5	37.8	37.1
B88/P86 ^b	53.0	43.1	38.0
experiment ^c	42.3 ± 6.7		

a) this work, b) Ref 12 c) Ref. 9 of the paper.

Table S2. Comparison of bond distances of CO adsorbed on Pt surface of current work with experimental results and other simulation results. (Distances in Å)

Energy functional	Top position	Bridge position	Three fold hollow
GGAII ^a	1.852	2.021	2.095
B88/P86 ^b	1.89	1.99	
experiment ^c	1.85±0.10	2.08±0.07	

a) this work, b) Ref 12 c) Ref. 13 and 14

Table S2 shows that bond distances of top position Pt-CO are in good agreement with the experimental value and the bond distances of bridge position Pt-CO is 0.020 Å shorter than experimental value.

The second calculation we used for validation was the binding of water molecule with the Pt 111 surface, that is to have considered slight or no poisoning effects. By using the same calculation method as for CO, we found that the most stable binding site has a binding energy of 11.0 kcal/mole and corresponds to water over the top position. This result compares well with the experimental value of 12.5 kcal/mole (Ref. 10 of the paper)

Imidazole molecule has an sp^2 lone pair orbital that is easy to bind with Pt surface vacant orbital to make large binding energy. Our DFT calculation indicates that a 1/4 coverage imidazole layer on platinum surface, whose structure is shown in Figure S3, will have 21.1 kcal/mole binding energy which is twice water's binding energy with platinum surface. The large binding energy between platinum surface and imidazole will keep activated species such as H_2 away from surface and thus block further reactions. To reduce the binding energy between platinum and imidazole, we consider that replacing H for an electron-acceptor such as the fluoro groups at the ring carbons will stabilize the sp^2 lone pair orbital and thus increase the mismatch between sp^2 lone pair and platinum surface vacant orbitals, responsible for the binding. The DFT calculation results in Table S3 shows

the effect of fluorination on lowering the energy of the sp^2 orbital from -9.9eV for imidazole (Im) to -11.3eV for 2,4,5-trifluoroimidazole (ImF3). The energy of the platinum surface vacant orbital is -5.66eV , according to the Castep calculation. As expected, the mismatch between sp^2 lone pair of substituted imidazole and platinum vacant surface orbital has increased with the fluorination, with a concomitant decrease in the binding energy of the molecule to the surface (see Table S3).

Table S3 Computed binding energies of water, CO, Im and ImF3 to the Pt surface.

Energy functional	Top position Binding energy (kcal/mol)	Bond distance(Å)
Water	11.0	2.142
CO	38.5	2.095
Imidazole	21.1	2.100
2,4,5-trifluoroimidazole	1.3	2.449

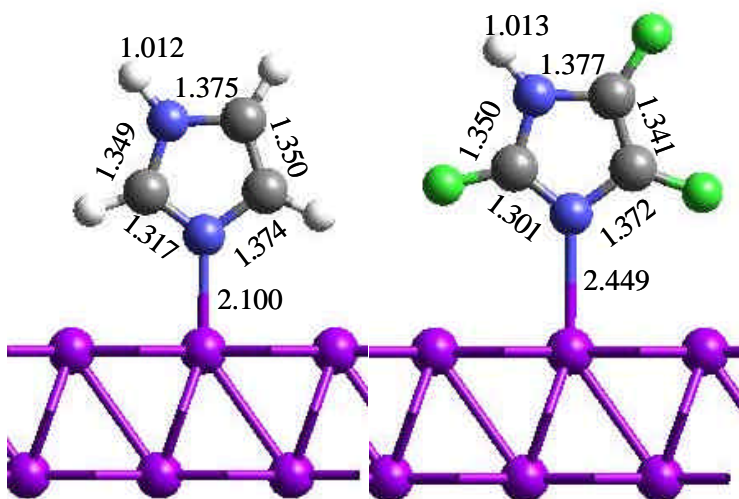


Figure S2. Binding of Im (left) and ImF3 (right) with platinum surface. The lone pair on nitrogen will strongly bind with platinum surface vacant orbitals. The color code is : Magenta for Pt, , gray for C, blue for N, green for F, and white for H.

The energies listed in Table S3 correspond to the binding energies of the monolayer to the Pt electrode. We also computed the intermolecular energy between the Im (or ImF3) in the monolayer, and found that is less than 1 kcal/mole.

We have considered other geometries for the binding of the Im and ImF3 to the Pt surface, and we found that the binding with the molecule plane perpendicular to the surface, with the bare N over a top position of the Pt 111 provides the highest binding energy. The binding energies of ImF3 perpendicular to the surface with the N over the three-fold FCC site is 0.92 kcal/mole, over the bridge site is 0.57 kcal/mole. We have also considered the binding of the ImF3 molecule parallel to the Pt surface, and found that the binding energy is even lower than the observed for the perpendicular geometry, confirming the absence of any poisoning effect of the ImF3 on Pt.

2. Im and ImF3 impregnated Nafion membranes.

In this section we describe the methodologies used to investigate the proton diffusion in the imidazole and trifluoroimidazole impregnated Nafion membranes.

2.1 Molecular Dynamics methods and force fields.

The Nafion/imidazole systems were modeled with fully atomistic detail using classical Molecular Dynamics in the canonical (NVT) and isobaric-isothermal ensemble (NPT). The calculations were performed using LAMMPS (Large-scale Atomic/Molecular Massively Parallel Simulator) code from Plimpton at Sandia [4,5], which was modified to handle our force fields.[9,11] The equations of motion were integrated using the Verlet algorithm[6] with a time steps of 1.0 fs, and the Particle-Particle Particle-Mesh (PPPM) method[7] was used for long range electrostatic interactions in the periodic cells.

The inter and intramolecular interactions were described through the DREIDING force field [8] in the version that improves the description of the fluorocarbon moieties [9]. Water is modeled using the F3C force field.[10] The force field details, charges, parameters, and application in the study of the structure and dynamics of hydrated Nafion membranes has been extensively described in a recent publication.[11] The imidazole,

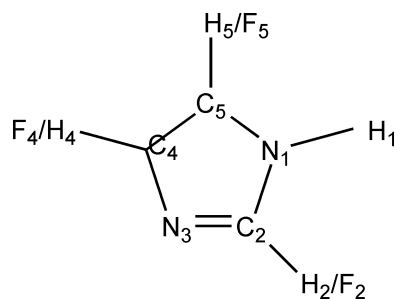
imidazolium, trifluoroimidazole and trifluoroimidazolium force field parameters correspond to the original DREIDING force field. The partial charges on the atomic sites of imidazole and trifluoroimidazole correspond to the the Mulliken charges computed from Quantum Mechanics optimization of the molecules in vacuum using B3LYP/6-311G** and are listed in Table S4.

We have prepared periodic simulation cells containing each four ionized Nafion chains, 40 protonated imidazolium (ImH⁺) (or trifluoroimidazolium, (ImF₃H⁺)) and 80 neutral Im or ImF₃. Each chain had the dispersed sequence [11] $(N_7P)_{10}$, where $N=(CF_2-CF_2)$ are the nonpolar TFE segments, and $P=(CF_2-CF(O-CF_2-CF(CF_3))-CF_2-CF_2-SO_3H)$ are the polar perfluorosulfonic vinyl ether (PSVE) segments,. The total number of atoms in each system was 3848. The proportion of 3 Im molecules per sulfonate of the Nafion chain corresponds to ~15% wt.

Table S4. The atomic charges for imidazoles and protonated imidazoles.

	ImH ⁺	Im	ImF3H ⁺	ImF3
N ₁	-0.1953	-0.5479	-0.2838	-0.6311
C ₂	0.1446	0.2063	0.4642	0.6701
N ₃	-0.1953	-0.4228	-0.2838	-0.4809
C ₄	-0.0978	-0.0301	0.2500	0.4067
C ₅	-0.0978	0.01816	0.2500	0.4217
H ₁	0.3666	0.3344	0.4097	0.3638
H ₂ /F ₂	0.2452	0.1546	-0.0827	-0.2402
H ₃	0.3666	----	0.4097	---
H ₄ /F ₄	0.2316	0.1354	-0.0667	-0.2583
H ₅ /F ₅	0.2316	0.1520	-0.0667	-0.2517

The label of the atoms for the charge assignment is indicated in the following scheme:



The ImF3/Nafion membranes were created and equilibrated as follows: we started from an equilibrated structure of hydrated Nafion, completely ionized, with 15 water molecules per sulfonate (~20%wt) at 353 K prepared as indicated in Reference [11], then the 560 water and 40 hydronium molecules were removed from the structure, and the polymer was loaded with i) 80 imidazole and 40 imidazolium, or ii) 80 trifluoroimidazole and 40 trifluoroimidazolium. We used the Monte Carlo procedure of Cerius2 Sorption Module [1] to load the molecules into the cell. The method was operated at fix load, and 10^5 Monte-Carlo steps were used to optimize the structures. The system was then equilibrated for 500 ps, performing a NPT dynamics at 450 K. The equilibration of the system was verified monitoring time dependence of the energy and density. Then, an 1 ns equilibrium NPT MD simulation at 450 K was run for each of the two systems. The equilibrium data of this work was collected from these 1 ns trajectories for each of the proton carriers..

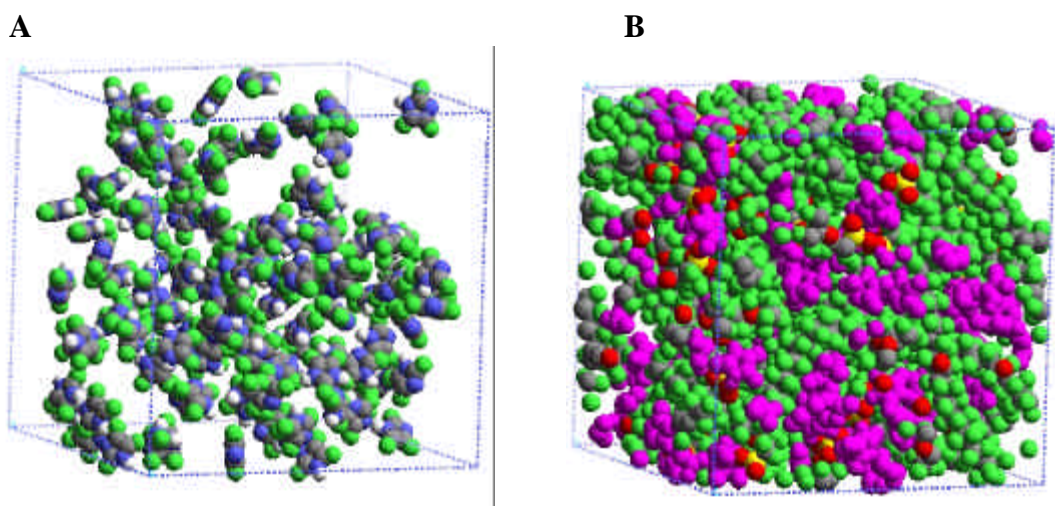


Figure S3. Typical configuration of ImF3/nafion that illustrates the structure of the membrane. A) Protonated (ImF3H⁺) and neutral (ImF3) carrier molecules, polymer hidden. B) Same configuration, showing the carriers (all in magenta) and the nafion chains.

2.2 Estimation of the proton diffusion coefficient.

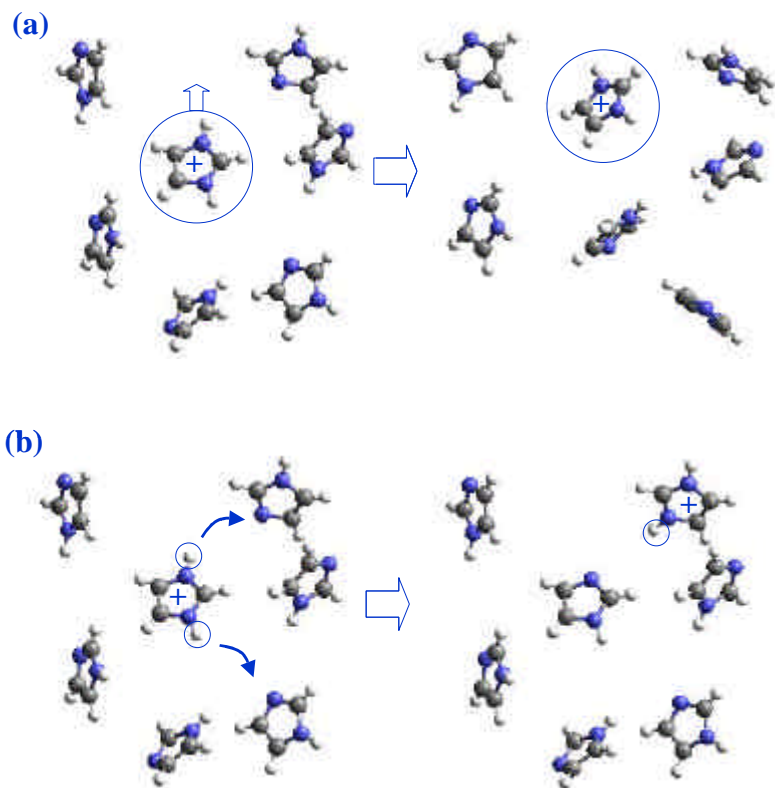


Figure S4. The scheme of proton diffusion mechanism. a) vehicular mechanism, protonated imidazole diffuse in the solvent. b) hopping mechanism, proton hops from one carrier to another

The proton diffusion mechanism includes the combination of two mechanisms, i.e., the vehicular mechanism and hopping mechanism. We use molecular dynamics (MD) to study protonated species, e.g., protonated imidazole and hydronium vehicular diffusion coefficients in Nafion.

2.2.1. Vehicular diffusion of protonated species.

The vehicular diffusion of the protonated molecules was calculated from the slope of the mean square displacement (MSD) with time:

$$D^{MSD} = \lim_{t \rightarrow \infty} \frac{\langle |\vec{r}(t) - \vec{r}(0)|^2 \rangle}{6t} \quad (1)$$

where r is the position vector and t is the time, and the brackets indicate an average over all the protonated carriers in the system and over the equilibrium trajectory. The resultant coefficient for the vehicular diffusion of imidazolium and trifluoroimidazolim are indicated in Table 1 of the paper.

2.2.2 Hopping contribution to proton diffusion.

The proton transfer rate $k(r)$ between a proton donor and a proton acceptor carrier was computed using transition state theory (TST) with the WKB [12] correction for proton tunneling.

$$k(r) = \mathbf{k}(T, r) \frac{k_B T}{2p\hbar} \exp\left(-\frac{E_b(r) - \hbar\omega_1(r)/2}{k_B T}\right)$$

where r is the distance between the donor and acceptor N atoms of the two molecules, $E_b(r)$ is the energy barrier to transfer the proton between these N atoms, and $\omega_1(r)$ is the frequency of the zero point energy correction.

We use B3LYP/6-311G** to scan the potential energy curves for the proton hopping reaction between a protonated and noprotonated (substituted) imidazole. The coordinates of energy curves are the N-N distance R_1 and the proton-oxygen distance R_2 (Figure S5). For each curve, R_1 is kept constant while R_2 is increased in increments of 0.01 Å. The calculated potential energy curves for several values of R_1 are displayed in Figure S5. The activation energy defined as the energy difference between the maximum and minimum points of the curve, decreases significantly as $R(N-N)$ decreases. At fixed R_1 , the left minimum corresponds to the equilibrium of a left imidazole molecule with a right protonated imidazole, whereas the symmetric minimum located at the right corresponds to a left protonated imidazole in equilibrium with a right imidazole molecule. A transition state for proton transfer corresponds to the maximum point in Figure S5, i.e., a proton is located equidistant between the two imidazole molecules. From Figure S5, we observe that, with the increase of the $R(N-N)$ distance, the activation barrier for proton transfer increases sharply, and at a certain small $R(N-N)$ value, the transfer is barrier free. Our results indicate that the proton hopping barrier is barely affected by the fluorination.

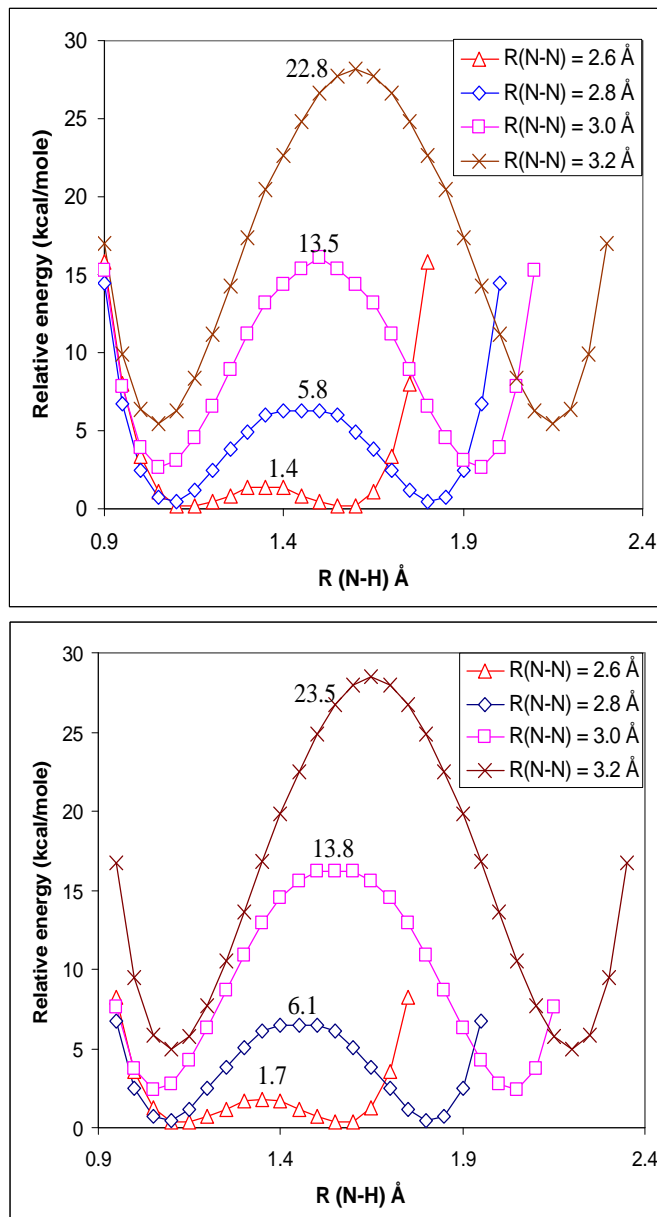
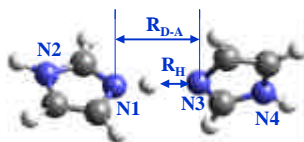


Figure S5. Proton hopping barriers a) between imidazoles and b) between trifluoroimidazoles.

Considering a particle hops distance r with hop rate k each time, the diffuse coefficient can be written as:

$$D = kr^2 \quad (2)$$

Therefore, for the case only considering proton hopping between carriers, the diffusion coefficient can be computed from the jump rates:

$$D_H = \frac{1}{6Nt} \int_0^{t \rightarrow \infty} \sum_i^N \sum_j^M k_{ij} r_{ij}^2 P_{ij} dt \quad (3)$$

where k_{ij} is the hopping rate from the i th position to the j th position, and the summation is taken over all possible values of i and j . P_{ij} is the probability of an ion being able to jump from site i to site j . We computed the distances between all pairs of donor and acceptors from the equilibrium molecular dynamics trajectory, and used Equation 3 to compute D_H . The distribution of distances between donor and acceptor N over the equilibrium trajectories for the Im/Nafion and ImF3/Nafion membranes is represented also in Figure 2b of the paper.

2.3 Orientational correlation times for proton carriers in Nafion membranes.

We computed the rotational correlation times from the integral of the first order orientational autocorrelation function C_1 for the vector formed by the two nitrogen atoms of each heterocycle:

$$C_1(t) = \frac{1}{N} \sum_{i=1}^N \langle \cos(\mathbf{q}_i(t)) \rangle \quad (4)$$

where N is the number of molecules of a given species (Im, ImH⁺, ImF3, or ImF3H⁺), $\mathbf{q}(t)$ is the angle rotated by the unit intramolecular NN vector in a time interval t , and the brackets indicate an average over multiple origins along the 1 ns equilibrium trajectory. Figure S6 shows $C_1(t)$ for the protonated and neutral carriers in the Nafion membrane at 450 K.

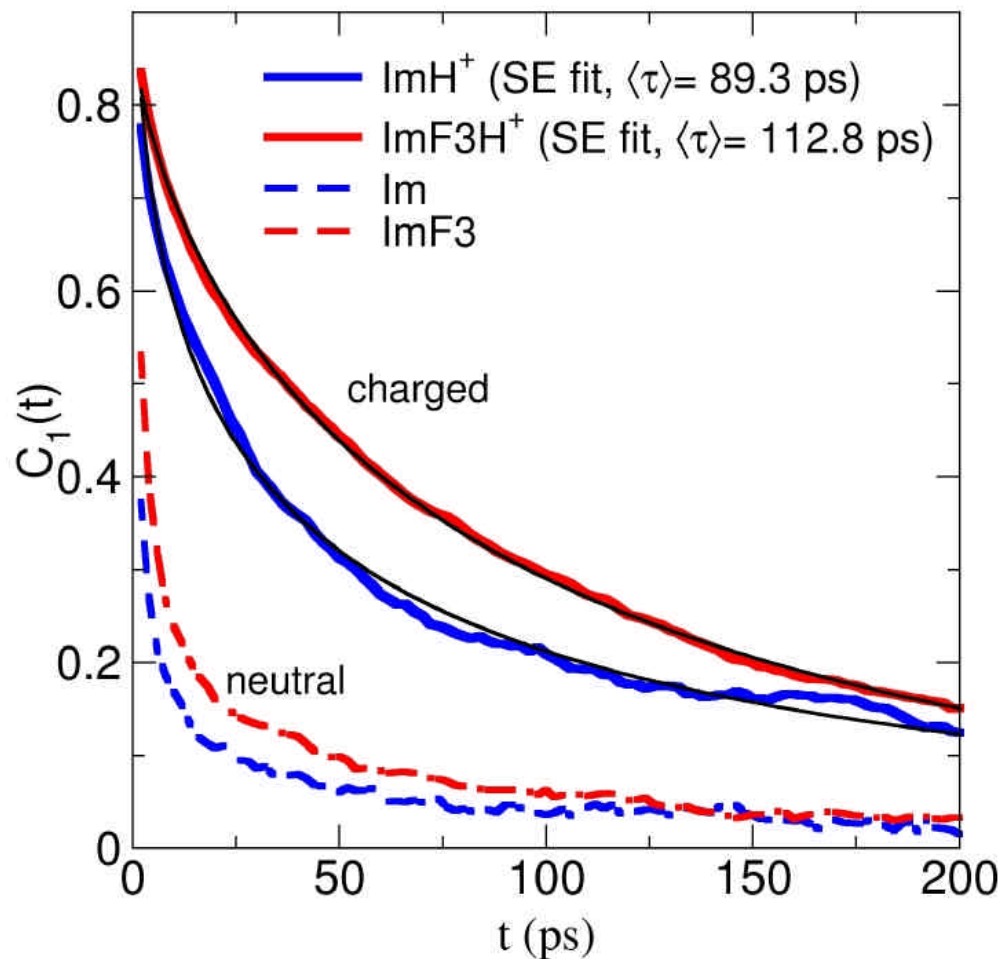


Figure S6. First order orientational correlation function for the unit vector that connects the two N atoms in the heteroring. Names as in the text. The black lines correspond to the best Stretched Exponential (SE) fits.

As the noise of the data increases with time t , due to the poorer statistics, we followed the usual custom of fitting the autocorrelation function to a stretched exponential function,

$$C_1(t) = Ae^{-(t/t)^b} \quad (5)$$

and computed the correlation time analytically from

$$\bar{t} = \frac{t}{b} \Gamma\left(\frac{1}{b}\right) \quad (6)$$

The resultant characteristic times for the rotation of the NN vector of the molecule are comparable for the hydrogenated and fluorinated species: 89.3 ps for imidazolium and 112.8 ps for trifluoroimidazolium.

References

- (1). Accelrys_Inc Cerius2 Modeling Environment, Release 4.0; Accelrys Inc.: San Diego, 1999.
- (2) Perdew, J. P.; Chevary, J. A.; Vosko, S. H.; Jackson, K. A.; Pederson, M. R.; Singh, D. J. and Fiohals, C. Phys. Rev. B 1992, 46, 6671.
- (3) Lin, J. S.; Qteish, A.; Payne, M. C.; and Heine, V.; Phys. Rev. B 1993, 47, 4174.
- (4) Plimpton, S. J. J. Comp. Phys. 1995, 117, 1.
- (5) Plimpton, S. J.; Pollock, R.; Stevens, M. In the Eighth SIAM Conference on Parallel Processing for Scientific Computing: Minneapolis, 1997.
- (6) Verlet, L. Phys. Rev. 1967, 159, 98.
- (7) Hockney, Roger W.; Eastwood, James W. Computer simulation using particles; McGraw-Hill International Book Co.: New York, 1981.
- (8) Mayo, S. L.; Olafson, B. D.; Goddard, William. A. J. Phys. Chem. 1990, 94, 8897.
- (9) Jang, Seung Soon; Blanco, Mario; Goddard, William A.; Caldwell, Gregg; Ross, Richard B. Macromolecules 2003, 36, 5331.
- (10) Levitt, Michael; Hirshberg, Miriam; Sharon, Ruth; Laidig, Keith E.; Daggett, Valerie J. Phys. Chem. B 1997, 101, 5051.
- (11) Jang, Seung Soon; Molinero, Valeria; Cagin, Tahir; Goddard III, William A. J. Phys. Chem. B 2004, 108, 3149-3157.

(12) Geschke D, Bastug T, Jacob T, Fritzsche S, Sepp WD, Fricke B, Varga S, Anton J. ,
Phys. Rev. B 2001, 64, 235411

(13) Ogletree DF, van Hove MA, Somorjai GA, Surf. Sci, 1986, 173, 351.

(14) Blackman, G.S.; Ogletree, D.F.; van Hove, M.A.; and Somorjai, G. A.; Phys. Rev.
Lett. 1988, 61, 2352.

Section 3: Carbon Nanotube technology

Chapter VIII: A Two-Stage Mechanism of Bimetallic Catalyzed Growth of Single-Wall Carbon Nanotubes

Abstract	156
Content	157
Reference.....	164
Figures and Tables	166

*Chapter VIII*A TWO-STAGE MECHANISM OF BIMETALLIC CATALYZED GROWTH OF SINGLE-WALL CARBON NANOTUBES^{††}

Abstract

Based on the analysis of Quantum Mechanics (the B3LYP flavor of Density Functional Theory) results for various reaction steps, we propose a two-stage mechanism for the metal atom catalyzed growth of single-wall carbon nanotubes (SWNT). This mechanism has two *essential* stages:

Nucleation of SWNT growth, which determines the number of nanotubes and

Growth with Defect Repair (G-DR), which determines the length of nanotubes.

Considering just the well studied systems involving Co, Ni, Pt, and Cu, our calculations indicate that Co is best for nucleation, followed by Co>Pt>Ni>Cu; while that Ni is best for G-DR, followed by Ni>Co>Pt>Cu, suggesting that Ni+Co is better than Ni or Co alone. This is consistent with experiment. We then considered a number of other metals (Cr, Fe, Mo, Rh, Pd) and based on the two-stage mechanism we suggest that Mo+Ni should be the best bimetallic catalyst from combining these elements (better than Ni+Co).

^{††} With Xin Xu's assistance at quantum mechanics calculations

The availability of single-wall carbon nanotubes (SWNT) has fired the imagination of advances in practical nanotechnology. The first SWNT were produced using arc discharge between metal containing carbon electrodes [1-2] with only modest yield, but laser vaporization techniques [3-4] now lead to high yield (more than 70-90%) of high quality SWNT. In addition, progress has been made in synthesizing SWNT with chemical vapor deposition [5-6] allowing control of the diameter with precise positioning on a substrate. Despite the promise, development of the effective processes for large-scale production of high quality SWNT required for commercial applications demands a much better understanding and control of the microscopic mechanisms. Unfortunately, the complexity of the synthetic procedures has made experimental determination of the mechanism very difficult and this complexity has also frustrated the progress in using theory and simulation to understand the mechanism of nanotube growth. [7]

Clearly, the presence of transition metals such as Ni and Co plays an essential role in producing single-wall nanotubes, since eliminating the metals leads only to finite fullerene balls and carbon deposits. Most likely, these metals act as isolated single atom catalytic sites since the concentration of the transition metal catalyst in the graphite material is quite low (<1%) and the growth temperature is too high for significant cluster formations. [8] On the other hand, there are synergetic effects of having two different metals present. For example, Co combined with Bi or Pb led to the broadening of the range of tube diameters, (with up to 60 Å diameter for Co + Bi) during arc discharge growth. [9] Moreover, the yield of SWNT for the Ni+Co and Ni+Pt bimetallic catalyst improves the production by 10-100 times. [4] However, the role(s) played by the metal remain quite uncertain, making it difficult to optimize the catalyst (metal and conditions).

Many mechanisms have been suggested but none explain the most salient observations from the experiments, namely:

- (1) the catalytic efficiency of different metals has the order Ni>Co>>Pt>>Cu [4] and

(2) the bimetallic catalysts such as Ni+Co produce 10-100 times than the yield of either Co or Ni alone, in the order Ni+Co>Ni+Pt >>Co+Cu [4] and Ni+Co > Ni+Fe ~ Ni >>Fe [10]

We consider that the metal atoms would bind most strongly to the exposed edge or a growing tube (or ball), which is highly active with isolated sp^2 radical sites containing destabilized pi bonds (1,2 benzyne type) in the plane. We consider that there are two likely roles of the metal:

(a) Nucleation: forming from available precursors a structure onto which carbon molecules and atoms can add to form bucky tubes

(b) Growth with Defect Repair (G-DR): build on the nucleated structure by adding carbon atoms and molecules to build the side walls while eliminating any carbon pentagons that would eventually close off the tube to terminate the growth.

To serve as a catalyst for growth with defect repair, the metal atom(s) would need to be sufficiently mobile to locate the defects associated with growth.

Based on this simple two-stage mechanism dominated by a nucleation stage and a defect repairing growth stage with migration, we developed a simple computational test for distinguishing the effectiveness of different metals, as illustrated by the diagram in Figure 1. In the nucleation stage, we consider that the small carbon clusters such as C_2 and C_3 dominating the vapor in growth conditions form stable polyynes ranging from C_{10} to C_{40} . [11] We consider that Co or Ni metal atoms add to the edges of the polyynes to form a cluster with one or more (isolated) metals, forming sites that can catalyze the addition of C_2 (and other gas phase species) to grow the ring into an initial tube [12]. In absence of a suitable metal, the nanotube can grow through C_2 additions, however, the formation of pentagon ring defects is energetically favorable, which would lead to closure of the nanotube (the path D in Figure 1) [8]. Thus for growth into bucky tubes, it is essential that the metal atoms at the growing edge of nanotube diffuse along the edge to find and anneal the pentagonal defects that would lead to closure of the nanotube. These

growth repair catalytic metal atoms might also assist the addition of C_2 or other gas phase species onto the growing edge.

We assume that the number of nanotube is determined by the efficiency of the nucleation stage, while the length of the nanotubes is determined by the effectiveness of the catalytic growth and repair stage. Both stages affect the yield of nanotubes. This suggests that improvement of yield for bimetallic catalysts may arise because one metal may be good at catalyzing nucleation (but may not be good for growth) while the other catalyst may be good for growth (while not so good for nucleation). Thus mixing these two catalysts can optimize both processes for maximum yield.

To test these ideas we carried out QM/MM (Quantum Mechanics combined with Molecular Mechanics) calculations (as implemented in Jaguar [13]) for SWNT with a catalytic atom attached to the edge. To examine the nucleation stage we considered a carbon ring cluster with 20 carbon atoms and a bound catalytic atom, fully optimized at the B3LYP/LACVP* level of Density Functional Theory (DFT). To examine the growth stage we considered a catalytic atom attached to a short carbon nanotube in which ~ 27 atoms near the metal are described with QM at B3LYP/LACVP* level while another ~ 138 carbon atoms are described using the Dreiding force field. [14]

First we test the two-stage model by considering the role of Ni, Co, Pt and Cu on both growth stages.

(A) *Nucleation of nanotubes* (see Figure 2): We assume that the nucleation stage of nanotube formation proceeds as follows: (1) First forming a suitable carbon ring and then attaching an appropriate metal atom to the edge of the ring forming a bridging site that causes the carbon ring structure to twist out of plane as in species (A). A Diels-Alder like addition of a C_2 molecule to (A) forms a hexagonal ring as in (B). (2) The metal atom then migrates along the carbon ring, passing through structures like (C) and (D) to form the twisted ring geometry as in (E). (3) The structure (E) is ready for another C_2 molecule to do the Diels-Alder addition forming a second hexagonal ring as (F). These three steps from (A) \rightarrow (F) complete a catalytic cycle for nucleation. These energetics suggest that Co is the

best catalyst for nucleation while Pt is almost as good as Co. Ni is a little worse than Co and Pt. Cu has an s^1d^{10} configuration so that it bonds to a single carbon atom for structures (A) and (E), leading to less stabilization of the new ring in (B) and (F). We conclude that Cu is the worst case for nucleation of nanotube among those metals.

(B) Growth of nanotubes — To grow the nucleated structure in Figure 2 into single-wall nanotubes, we must add carbons to form the six-member rings of the sidewall while avoiding the pentagonal rings that would tend to close up the tube. In the absence of metal atoms this latter tube closing mechanism probably dominates. C_2 can add on the edge of nanotube either perpendicular or parallel to the growth edge. Parallel addition forming hexagon rings is 25.7 kcal/mol energetically more favorable than perpendicular addition forming pentagon rings. However, when two C_2 species are added to two adjacent sites, the perpendicular additions will become energetically favorable than the parallel additions. As shown in Figure 1, pathway (D) is that two adjacent perpendicular additions lead to a defect with a new hexagon and two pentagon rings (called the 5,5,6,6 defect) while pathway (C) is that two adjacent parallel connections lead to two hexagon rings. Consequently, following pathway (D) leads to closure of the nanotube tip since it leads to formation of additional similar defects. In contrast, following pathway (C), the growth will continue since no defects are formed. The calculations show that without a metal pathway (D) is 30.2 kcal/mol more favorable than pathway (C). Therefore, in the absence of metal atoms nanotube growth will quickly terminate by closing the open end needed for growth. Thus the 5566 defects play a more important role than isolated pentagon rings.

Now, we discuss how the presence of an appropriate metal can affect the mechanism by catalyzing the annealing of the defect in pathway (D) in Figure 1 that would otherwise initiate dome closure of the tube. The catalytic atom must also diffuse along on the edge or on the wall of the nanotube to anneal the growth defects before they can cause closure. Thus we calculated the interaction between metal and this defect to study the efficiency of a catalyst to anneal the formed defects. Figure 3 indicates how a catalytic atom anneals the defect. After the catalytic atom attaches to the edge of the nanotube growth front to form species (A), it can move along the defect to form (B) and then insert into the defect to form species (C) in step (1). An incoming C_2 species can be attracted to the catalytic atom to

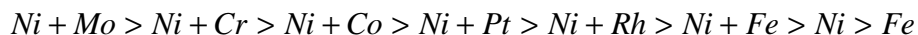
form (D), subsequently releasing the metal atom and forming species (E) in step (2). The result of these two steps is that the catalytic atom moves out from the defect and adds a C₂ to build a hexagon ring. In order to complete the catalytic cycle, another C₂ is added to form species (F), which rearranges into species (G) in step (3). This catalytic cycle can continue to grow the bucky tube. As shown in Fig. 3, our results indicate that Ni, Co and Pt lead to favorable energetics for this catalytic cycle, but Cu does not. Because steps from (C) to (G) involve C₂ addition, which is quite favorable energetically, step (1) from (A) to (C) which involves only rearrangement of the bound metal atoms with the edge defect will be the key step in determining the efficiency of various catalyst atoms. Comparing Ni, Co and Pt at step (1) from species (A) to (C), we see that Ni should be best for annealing the defect (rearrangement energy of only 1.5 kcal/mol). Next best is Co (requiring 9.8 kcal/mol), followed by Pt with a barrier of 18.6 kcal/mol. Poorest is Cu, which because of its s¹d¹⁰ structure can only form one bond with the edge, leading to the largest barrier of 51.2 kcal/mol to insert into a defect to set up multiple bonds. We expect that Cu will poison growth since it would block the forthcoming annealing. Therefore, we conclude the catalytic efficiency for the growth stage is Ni>Co>Pt>>Cu. Indeed this order is exactly the same as deduced from experiment. [4] This suggests that the ability to maintain growth is more important than nucleation for mono-metal catalyzed growth.

(C) The mechanism for bimetallic catalysts — Since the growth and nucleation stages involve different chemical properties, it is likely that the best catalyst for one might be different for the other. Thus we propose that the mechanism to explain the extraordinary improvement of SWNT production using bimetallic catalysts (10 to 100 times yield than the best monometallic catalyst) is that one metal is responsible for nucleation while the other is responsible for G-DR. Since we find that the effectiveness for the nucleation stage is Co > Pt > Ni > Cu while that the effectiveness for growth stage is Ni > Co > Pt > Cu, we conclude that the mixture of Co and Ni would be the best catalysts for growth, followed by Ni mono-metal and then Pt. Of course the worst would Ni mix with Cu where Cu is expected poison the catalyst. These conclusions are in exact agreement with experimental results. [4]

D) Design of new catalysts — In order to design better catalysts, we consider several additional metals: Cr, Fe, Rh, Mo. Previous arc discharge experiments on Fe and Rh by themselves show poor growth rates, while Mo by itself does not work. [15,16] In order to simplify the evaluation, we choose several key structures in the nucleation and G-DR stages, i.e., species (A) and (F) in Figure 2 and species (A) and (D) in Figure 3. Table 1 summarizes our results. We rank Rh, Pd, Cr, Mo along with Ni, Co, Pt and Cu by comparing the energetics of these key structures for nucleation and G-DR. Among all 8 candidates, the poorest at nucleation and G-DR catalyst is Cu, which likely would act as a poison to growth. This may explain why all attempts at bimetallic catalysts using Cu did not work (e.g., Ni+Cu and Co+Cu [4]). Therefore new catalyst should not include any Cu component.

We find that the best catalyst for nucleation is Mo followed by Cr, and then Co, Pt and then Rh, Fe, Ni, and Pd.

However, the best growth catalyst is still Ni, followed by Fe and then Mo and Co. Therefore, we predict that the best catalyst for SWNT growth is Ni+Mo. Combining the predictions for nucleation and growth, these results suggest the following sequences of effectiveness:



Although there is less data about bimetallic catalysts for nanotube growth, our predictions lead exactly to the sequence: Ni+Co>Ni+Pt>Ni>Ni+Cu established experimentally in reference [4] and the sequence Ni+Co > Ni+Fe ~ Ni >>Fe established experimentally in reference [9] (we find that Ni + Fe should be slightly better than Ni alone, but the experiments report that they are similar). Indeed an experiment shows that Ni+Cr is more efficient than Ni alone for arc discharge growth of carbon nanotubes. [17] No experiments have been reported for the combinations Ni+Mo, Fe+Mo and Co+Mo that

we expect to be the best catalysts. Some chemical vapor deposition (CVD) did find that Mo impurities enhance the yield of nanotube combined with Fe or Co. [18,19]. But this may not be relevant since the mechanism for CVD production of SWNT (likely involving nucleation and growth on the solid surface) is quite different than the gas phase growth for laser vaporization we are considering. On the other hand our predicted preferences for different metals are reasonably consistent with CVD experiments, suggesting that there may be similar processes in both growth situations.

Lee et al. [8] discussing the mechanism for Ni acting alone, suggested that Ni migrates along the growth edge to prevent tube closure by eliminate pentagons as they form. They did not show why Ni would be better at this than other atoms. Our proposed growth stage is similar except that we conclude that the critical defect which must be removed is the 5566 defect, which as discussed above is much more stable than isolated five-member rings and hence more difficult to eliminate. In addition we showed that Ni is much better than other atoms. Of course in addition to defect repair stage that is important to growth our mechanism also accounts for nucleation,

Another mechanism proposed by Andriotis et al. [20] assumed that Ni atom repairs defects in the nanotube, binds to the defect, and then catalyzes the incorporation of a gas phase carbon atom to anneal the Ni-stabilized defects, freeing the Ni atom to be available to migrate to a new defect site. They did not explain why Ni is better than other atoms. Because a free carbon atom is much more active than metal atoms, we expect that replacing a metal atom in the carbon nanotube by free carbon atoms is energetically favorable for most metals. Thus the Andriotis mechanism does not explain the observed huge difference in catalytic behavior between Ni, Co, Pt and Cu, the last of which has no nanotube yield.

In summary, we propose a reasonable catalytic mechanism for the growth of carbon nanotubes that explains the observations on both monometallic and bimetallic catalytic effects on the basis of steps based on atomistic quantum calculations. Thus our two stage mechanism explains that the monometallic catalytic efficiency is in the sequence: Ni > Co > Pt >> Cu and also explains that the bimetallic catalytic efficiency is sequenced as: Ni + Co > Ni + Pt > Ni > Ni +Cu. These results agree with experiment. [4,10] In addition we

used the two-stage mechanism to consider several systems not previously studied. We conclude that Ni+Mo and Cr+Ni should be even more efficient than the current catalysts and that Fe+Mo and Co+Mo might also be good catalysts.

This work was supported by an NSF-NIRT grant. The facilities of the Materials and Process Simulation Center (MSC) used in these studies were funded by DURIP (ARO and ONR), NSF (CTS and MRI), and a SUR Grant from IBM. In addition, the MSC is funded by grants from ARO-MURI, NIH, Chevron Texaco, General Motors, Seiko-Epson, the Beckman Institute, Asahi Kasei, and Toray Corp.

Reference:

- [1] S. Iijima and T. Ichihashi, *Nature (London)* **363**, 603 (1993).
- [2] D. S. Bethune, C. H. Kiang, M. S. Devries, G. Gorman, R. Savoy, et al, *Nature (London)* **363**, 605 (1993).
- [3] A. Thess, R. Lee, P. Nikolaev, H. J. Dai, P. Petit, et al, *Science* **273**, 483 (1996).
- [4] T. Guo, P. Nikolaev, A. Thess et al., *Chem. Phys. Lett.* **243**, 49 (1995).
- [5] H. M. Cheng, F. Li, G. Su, H.Y.Pan, L.L. He and et al., *Appl. Phys. Lett.* **72**, 3282 (1998)
- [6] H. J. Dai, J.Kong, C.W. Zhou, N. Franklin, T. Tomblor and et al., *J. Phys. Chem. B* **103**, 11246 (1999).
- [7] J. C. Charlier and S. Iijima, *Top. Appl. Phys.* **80**, 55 (2001).
- [8] Y. H. Lee, S.G. Kim and D. Tomanek et al., *Phys. Rev. Lett.* **78**, 2393 (1997).
- [9] C. H. Kiang, W. A. Goddard et al., *J. Phys. Chem. Solids* **57**, 35 (1996)
- [10] A. A. Puretzky, D.B. Geohegan, X. Fan and et al., *Appl. Phys. A* **70**, 153 (2000).

- [11] X. Hua, T. Cagin, J. Che and W.A. Goddard, *Nanotechnology* **11**, 85 (2000)
- [12] C. H. Kiang and W. A. Goddard, *Phys. Rev. Lett.* **76**, 2515-2518 (1996).
- [13] Jaguar 4.0, Schrodinger, Inc. Portland, OR, 1997.
- [14] QM/MM calculation: the nanotube QM region is created by including metal atoms and the 5566 defect (14 carbon atoms) plus 3 adjacent 6-member rings where metal atom will immigrate to (12 carbon atoms). The ab initio total energy calculations were performed by using B3LYP. The atomic basis set used is LACVP* including relativistic effects for heavy atoms. The ground state was chosen by the structure with the lowest energy among different spin states of each structure. Dreiding force field was described in S. L. Mayo, B. D. Olafson and W. A. Goddard, *J. Phys. Chem.* **94**, 8897 (1990)
- [15] Y. Saito, K. Nishikubo, K. Kawabata and T. Matsumoto, *J. Appl. Phys.* **80**, 3062 (1996). [16] H. Takikawa, O. Kusano and T. Sakakibara T, *J. Phys. D* **32**, 2433 (1999)
- [17] V. N. Bezmel'nitsyn, A.G. Domantovskii, A.V. Elets'kii, E.V. Obraztsova and et al., *Phys. Solid State*, **44**, 656 (2002)
- [18] Y. J. Yoon, J. C. Bae, H. K. Baik, S. J. Cho, S. J. Lee and et al., *Physica B* **323**, 318, (2002).
- [19] A. M. Cassell, J. A. Raymakers, J. Kong and H. J. Dai J, *J. Phys. Chem. B* **103**, 6484 (1999).
- [20] A. N. Andriotis, M. Menon and G. Froudakis, *Phys. Rev. Lett.*, **85**, 3193 (2000).

Table 1. Energetics for the diagnostic steps of the nucleation and growth mechanisms (units: kcal/mol). Category IV is best while category I is worst.

	I		II		III		IV	
<i>Nucleation</i>	Cu	-198.4	Pd	-212.221	Pt	-233.8	Cr	-256.7
Species (A) → Species (F) in Figure 2			Ni	-215.8	Co	-236.1	Mo	-259.0
			Fe	-222.2				
			Rh	-227.8				
	Poorest		Poor		Good		Best	
<i>Growth</i>	Cu	51.25	Pd	28.45	Co	9.83	Ni	1.48
Species (A) → Species (C)			Rh	25.40	Mo	8.54	Fe	2.94
			Cr	25.23				
			Pt	18.55				
	Poorest		Poor		Good		Best	

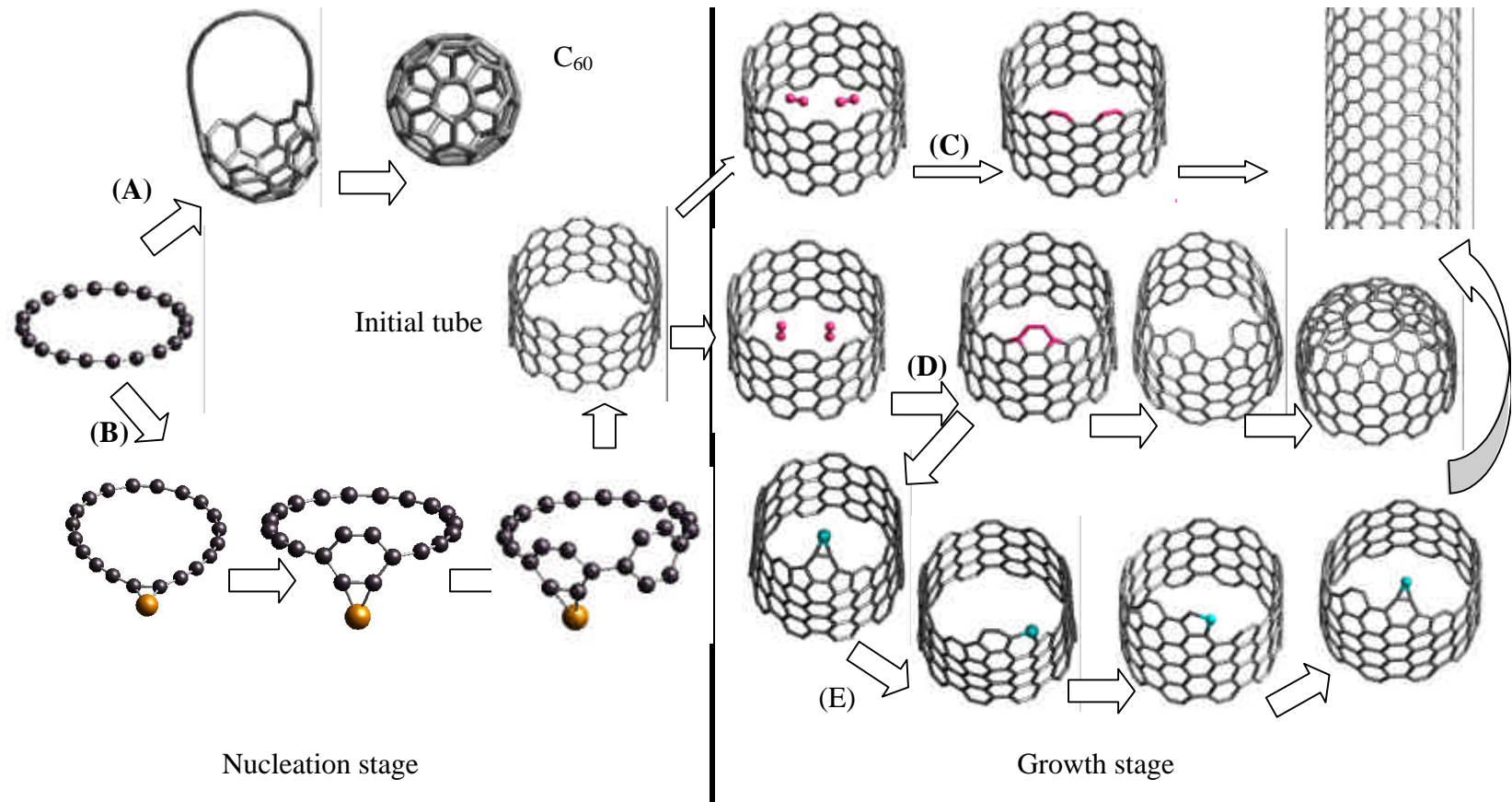


FIG. 1 Idealized steps for the two-stage growth model of nanotubes.

Nucleation Stage: This stage has two distinct types of paths. Path (A): Without a metal the rings lead to formation of C₆₀ or fullerenes (see Ref 11). Path (B): The presence of catalytic metal on a ring initiates the formation of six member rings, leading to tube formation.

Growth Stage: This stage has three distinct types of paths: Path (C) favors forming a nanotube by direct parallel addition of C₂ at the growth edge; Path (D) forms a 5566 defect (that would lead to tube closure) by direct vertical addition of C₂ at the growth edge which without a metal present is 30 kcal/mol more favorable than path (C); Path (E) anneals the 5566 defect with the assistance of catalytic metal atoms.

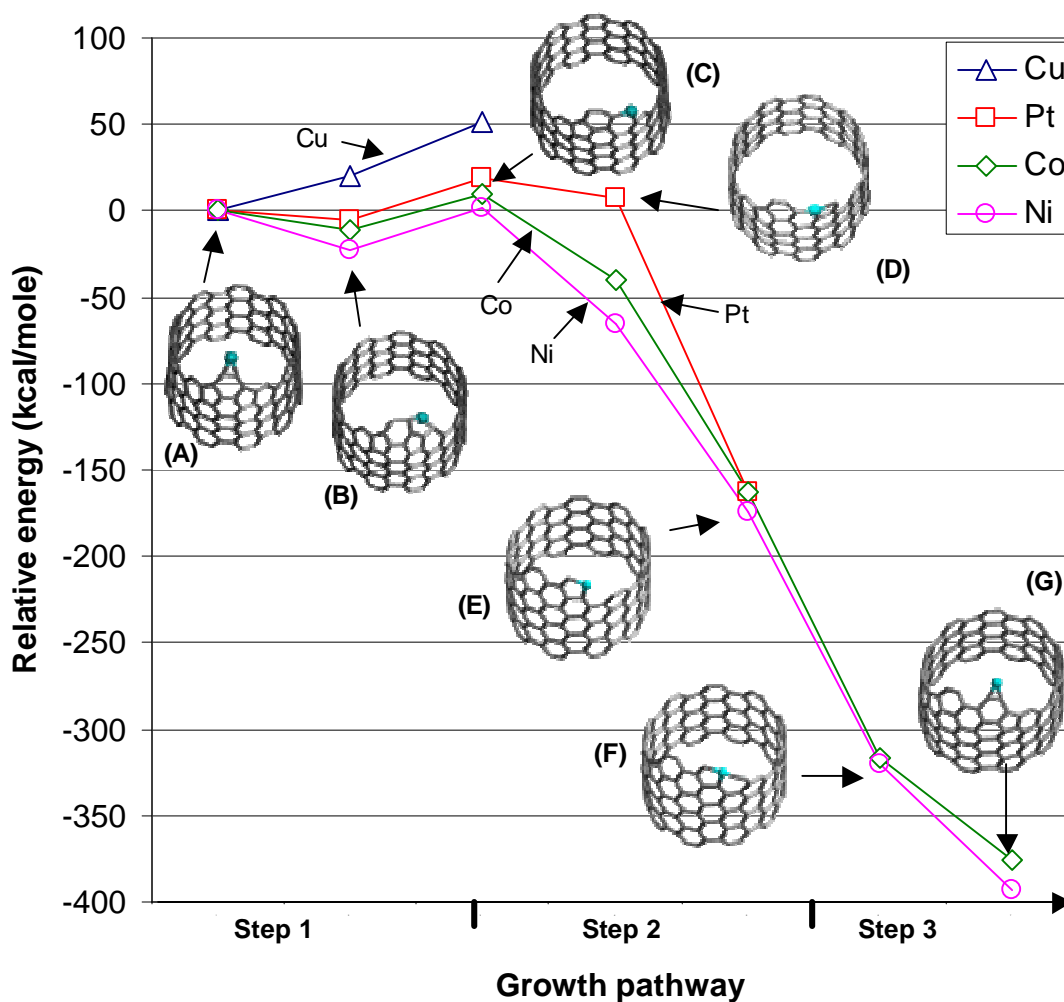


FIG. 3. Catalytic circle for the growth stage of SWNT (Path E of Figure 1). Species (A) has a (5566) defect which without metal would tend to close the nanotube as in Path D of Figure 1.

Step 1: Moving the metal atom from (B) to (C) eliminates one 5-ring defect, the critical step in the repair mechanism.

Step 2: A C_2 adds on the growth edge and releases the metal from the defect.

Step 3: Metal migrates along the edge and assists another C_2 addition to go onto another cycle.

The diagnostic for a successful G-DR is ΔE from species (A) to (C). Shown are the energetics for four different metals.

A p p e n d i x A

LIST OF PUBLICATIONS

SELECTED JOURNAL PAPERS

1. **Deng, W.-Q.**; Xu X.; and Goddard III, W.A.; “New Alkali Doped Pillared Carbon Materials Designed to Achieve Practical Reversible Hydrogen Storage for Transportation” *PHY REV LETT* (2004) **92**, 166103
2. **Deng, W.-Q.**; Molinero V.; and Goddard III, W.A.; “Fluorinated imidazoles as proton carriers for water-free fuel cell membranes” *J AM SOC CHEM* Submitted 2004
3. **Deng, W.-Q.**; Xu X.; and Goddard III, W.A.; “Simulation of Li-doped pillared carbon based materials for reversible hydrogen storage” *J PHY CHEM* submitted 2004
4. **Deng, W.-Q.**; Xu X.; and Goddard III, W.A.; “Ultrafast proton-hopping molecular switch” *J AM SOC CHEM* submitted 2004
5. **Deng, W.-Q.**; and Goddard III, W.A.; “The Nano-bracelet, a new family of organic semiconductors.” Submitted 2004
6. **Deng, W.-Q.**; and Goddard III, W.A.; “Predictions of Hole Mobilities in Oligoacene Organic Semiconductors from Quantum Mechanical Calculations” *J PHY CHEM* In press
7. **Deng, W.-Q.**; Xu, X.; and Goddard III, W.A.; “A two-stage mechanism of bimetallic catalyzed growth of single-wall carbon nanotubes” *PHY REV LETT* submitted 2003
8. **Deng, W.-Q.**; Muller, R. P. and Goddard III, W.A.; “Mechanism of the Stoddart-Heath bistable rotaxane molecular switch” *J AM SOC CHEM* submitted 2003
9. Che, J. W.; Cagin, T.; **Deng, W.-Q.** and Goddard III, W.A.; “Thermal conductivity of diamond and related materials from molecular dynamics simulations” *J CHEM PHYS* 113 (16): 6888-6900 OCT 22 2000

PATENTS

1. "Carbon-based compositions for reversible hydrogen storage". pending CIT 3806-P, 2003.
2. "Proton hopping molecular switch" In preparation.
3. "Nanobracelet organic semiconductor" In preparation.

New Alkali Doped Pillared Carbon Materials Designed to Achieve Practical Reversible Hydrogen Storage for Transportation

Wei-Qiao Deng, Xin Xu,* and William A. Goddard[†]

Materials and Process Simulation Center, Division of Chemistry and Chemical Engineering, California Institute of Technology, Pasadena, California 91125, USA

(Received 29 May 2003; published 21 April 2004)

We propose a new generation of materials to maximize reversible H₂ storage at room temperature and modest pressures (< 20 bars). We test these materials using grand canonical Monte Carlo simulations with a first-principles-derived force field and find that the Li pillared graphene sheet system can take up 6.5 mass% of H₂ (a density of 62.9 kg/m³ at 20 bars and room temperature. This satisfies the DOE (Department of Energy) target of hydrogen-storage materials for transportation. We also suggest ways to synthesize these systems. In addition we show that Li-doped pillared single-wall nanotubes can lead to a hydrogen-storage capacity of 6.0 mass% and 61.7 kg/m³ at 50 bars and room temperature storage, which is close to the DOE target.

DOI: 10.1103/PhysRevLett.92.166103

PACS numbers: 68.43.-h, 61.46.+w

Perhaps the most promising technology to dramatically decrease pollution while conserving the decreasing supply of fossil fuel is the use of hydrogen fuel cells in transportation. Unfortunately this solution is impeded by the lack of safe and economical ways to store the hydrogen on board a vehicle. The U.S. Department of Energy (DOE) has estimated that attaining a suitable driving range for automotive applications will require storing 6.5 mass% of hydrogen (density of 62.5 kg/m³), whereas the best materials such as cubic TiV₂ can storage only up to 2.6 mass% at 10 bars and 313 K [1].

Recent claims of large hydrogen uptake for lightweight nanostructured carbon materials, in the form of tubes [2–5], fibers [6,7], and mechanically milled graphite [8], have attracted considerable experimental and theoretical interest. For example, Ye *et al.* used high-purity single-walled carbon nanotubes (SWNTs) and obtained ~8.0 mass% of H₂ adsorption at 80 K and above 100 bars [3]. Browning *et al.* reported that 6.5 mass% hydrogen can be stored in carbon nanofibers under conditions of 120 bars pressure and ambient temperature [7]. These H₂ uptake systems require either high pressure [7] or very low temperature [6] or both [3] that limit the applicability for mobile applications that require working conditions of roughly 1–20 bars and ambient temperature. Chen *et al.* reported remarkable hydrogen-storage capacities of 20 mass% for Li-doped nanotubes at 653 K and 14 mass% for K-doped nanotubes at room temperature [9]. They also reported smaller but still significant absorptions in alkali doped graphite (14 mass% for Li and 5 mass% for K) [9]. Unfortunately, later studies revealed that these high H₂ uptakes were due to the impurity water gain/loss present in the hydrogen feedstream rather than to H₂ itself [10,11].

We report here a new class of materials for reversible hydrogen storage designed to meet the criteria for transportation applications. To validate our design we use a

multiscale computational strategy [12,13], in which quantum mechanics (QM) at the X3LYP [14] level of density functional theory (DFT) developed to accurately treat van der Waals interactions is used to determine an accurate force field (FF) [15]. We then use this FF with grand canonical Monte Carlo (GCMC) simulations to determine the H₂ uptake as a function of pressure and temperature [13].

As discussed below, normal condensed graphite and nanotube systems are too dense to bind sufficient H₂ and we also considered graphene sheet and SWNT systems pillared to provide more space. To determine the optimum performance, we first ignore the space taken by the pillars and then address it later. For our model SWNT we consider (10,10) which leads to a tube diameter of ~13.6 Å, close to the mean diameter most frequently observed in SWNT synthesized by the arc-discharge or pulsed-laser vaporization techniques [16]. Curves (a)–(c) in Fig. 1(b) show the predicted H₂ storage at 300 K and

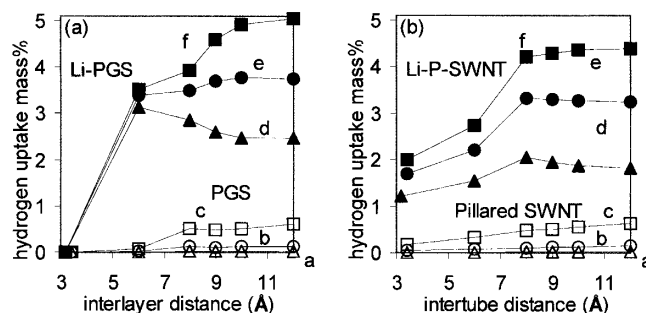


FIG. 1. Dependence of the mass hydrogen storage capacity on the interlayer (intertube) distances under various pressures for (a) PGS (white) and Li-GIC or Li-PGS (black); and (b) (10,10) SWNTs (white) and Li-P-SWNT (black) systems. The doping concentration is Li:C = 1:6. The pressures are square = 50 bars; circle = 10 bars, and triangle = 1 bar.

various pressures for pure pillared SWNTs (P-SWNT) as a function of the intertube distance (ITD) between the SWNT. The first point at 3.4 Å corresponds to the equilibrium ITD in the SWNT crystal, where we find 0.2 mass% at 50 bars, due entirely to the internal spaces of the SWNTs. These results are in good agreement with recent experiments [2,3,6] and computations on SWNTs [17]. Thus Ye *et al.* [3,6] reported 2–4 mass% storage for 20–50 bars at 80 K, comparable to our calculated results of 3–4 mass% at the same conditions; Hirscher [2] reported 0.005 mass% storage at 300 K and 1 bar while we calculate 0.01 mass% under these conditions. For P-SWNT we find a slight increase to 0.1 mass% at 10 bars and 0.5 mass% at 50 bars for ITD > 8 Å. The performance of pure pillared graphene sheets (PGS) is similar. Curves (a)–(c) in Fig. 1(a) show the predicted hydrogen storage for a function of the interlayer distance (ILD). The first point (3.4 Å) corresponds to the equilibrium ILD in bulk graphite, leading to zero hydrogen uptake. As the ILD is increased to over 8 Å, we find that the hydrogen uptake for PGS reaches 0.1 mass% at 10 bars and 0.5 mass% at 50 bars. Thus we conclude that the hydrogen-storage capacity at ambient conditions is very limited for carbon-only systems such as graphene sheets and SWNTs, even if pillared to provide more space for the hydrogen.

In order to increase the hydrogen-storage capacity, we considered adding Li to the PGS and P-SWNT systems. Our reasoning was that the high electron affinity of the sp^2 carbon framework would separate the charge from the Li, providing strong stabilization of the molecular H_2 . We first considered a Li-doping concentration of Li:C = 1:6, which corresponds to the most stable conformation of Li-GIC (graphite intercalated compound) at ambient conditions. Curves (d)–(f) in Fig. 1(a) show the results for Li-PGS. The first point at ILD = 3.4 Å shows that Li-GIC does *not* exhibit hydrogen-storage capacity, in agreement with the experimental observation of Pinkerton *et al.* [11]. Curves (d)–(f) in Fig. 1(b) show the results for Li-P-SWNT. The equilibrium ITD of 3.4 Å leads to 1.2 mass% hydrogen storage at 1 bar, which increases to ~2.0 mass% for 50 bars. Here 99.5% of the storage comes from the space *inside* the nanotubes. These results suggest an explanation for the differences observed between different experiments [10]. Pinkerton [11] found no observable hydrogen-storage capacity for Li-doped nanotubes, but they used closed-end nanotubes that would prevent H_2 from entering the tubes. Yang [10] made nanotubes by chemical vapor deposition followed by purification with strong acid, which will cut off the nanotube caps [10], allowing the H_2 to go inside. The found ~2.5 mass% hydrogen storage for Li-doped nanotubes at 1 bar and ambient temperature. This is consistent with our results of 1.2 mass% at the same conditions. The small discordance here might be because we considered the infinite crystal with no surfaces, whereas the experiments probably had

substantial surface area which might increase the net storage. We conclude that Li-doped carbon SWNTs do exhibit modest hydrogen-storage capacity at ambient conditions, but not enough to meet the DOE requirements for transportation. Consequently we will explore below how the hydrogen storage can be increased with additional Li-doping and modified nanostructures. The results in Fig. 1 show that a Li-PGS and Li-P-SWNT in which graphene or SWNT sheets are separated by ILD or ITD of 6 to 12 Å significantly enhance the storage capacity. This is in sharp contrast to the situation for undoped PGS or P-SWNTs where increasing the ILD or ITD has a very limited effect on the storage capacity. This is also in contrast to the un-pillared system where Li doping has only a very modest effect on hydrogen storage. The Li-doped pillared systems also lead to a much larger benefit from increased pressure. Thus Fig. 1 shows that at 10 bars and room temperature the hydrogen-storage capacity increases from 0.1 mass% for PGS to 3.7 mass% for Li-PGS (Li:C = 1:6) with the ILD increased to 10 Å.

Our simulations show that Li dopants act as positive (acidic) cores that attract hydrogen molecules. The lack of hydrogen-storage capacity in ordinary graphite and SWNT systems is due to the restricted space available around the Li dopants. These results suggest that by pillaring to increase the interlayer distances and by increasing the Li-doping concentration, it may be possible to reach the DOE goal with Li-doped pillared carbon-based materials.

Given the very favorable synergetic affect of combining Li doping with pillaring of graphitic sheets, we considered optimizing the amount of Li. Figure 2(a) shows that increasing the Li-doping concentration increases the hydrogen-storage capacity nearly linearly, increasing from 3.7 mass% at Li:C = 1:6 to 6.5 mass% at Li:C = 1:3 (for Li-PGS with ILD = 10 Å at 10 bars). To determine the maximum feasible concentration, we carried out a DFT

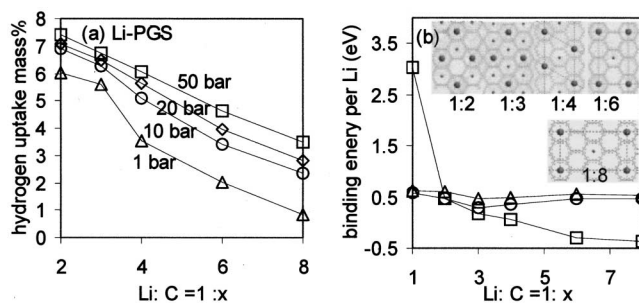


FIG. 2. (a) Effects of Li-doping concentration on the mass hydrogen storage capacity under various pressures. ILD = 10 Å. (b) Binding energy per Li atom under various Li-doping concentrations. Keys in (b) square = equilibrium interlayer distance; circle = interlayer distance 8 Å; triangle = interlayer distance 10 Å. The zero energy reference responds to pure graphite crystal and pure Li metal.

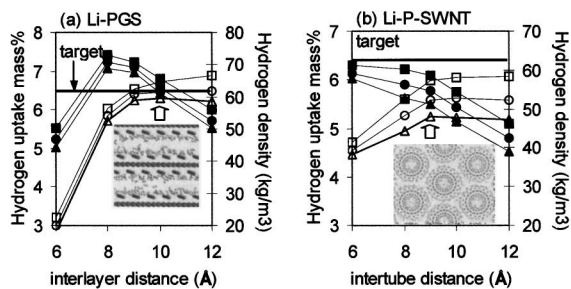


FIG. 3. Optimization of nanostructures of (a) Li-PGS and (b) Li-P-SWNT systems for mass (white) and volumetric (black) hydrogen storage capacities. The Li-doping concentrations are Li:C = 1:3. The DOE target is shown by a line. The optimum interlayer or intertube distance is indicated by an arrow. Key: square = 50 bars; circle = 20 bars, and triangle = 10 bars.

calculation on Li-GIC and Li-PGS for various Li:C ratios [18]. Figure 2(b) shows that at the equilibrium interlayer distance Li-GIC is most stable for Li:C = 1:6 and Li:C = 1:8, in agreement with experimental observation. However, for Li-PGS, Li:C = 1:3 is the most stable structure for $ILD > 8 \text{ \AA}$. Figure 3(a) shows the hydrogen-storage performance for the optimum Li-PGS (Li:C = 1:3 and $ILD = 10 \text{ \AA}$). At room temperature and 20 bars this leads to hydrogen storage of 6.5 mass% and 62.9 kg/m^3 , which fulfills the DOE requirements (6.5 mass% and 62 kg/m^3). The DOE target could be surpassed to 6.7 mass% and 65.8 kg/m^3 with an operating pressure of 50 bars. Figure 3(b) shows the results for Li-P-SWNT for Li:C = 1:3 and $ITD = 9 \text{ \AA}$. Here we find hydrogen storage of 6.0 mass% and 61.7 kg/m^3 at room temperature and 50 bars. Thus Li-PGS has better hydrogen-storage performance than Li-P-SWNT and is likely to be much less expensive, making Li-PGS an excellent candidate for developing a practical H_2 storage system for transportation. Figure 4 illustrates how temperature and pressure effects can be used to design the load/unload operating process for a reversible hydrogen-storage system. For example Li-PGS (Li:C = 1:3 with $ILD = 10 \text{ \AA}$) reaches 6.5 mass% hydrogen uptake under loading conditions of 20 bars and 300 K. Under the unloading conditions of 0.01 bar and 400 K, the residual hydrogen is 0.2 mass%. Therefore, the total load/unload will provide 6.3 mass% reversible hydrogen. This is far superior to any other hydrogen-storage system.

Ball milling has been established to effectively increase the Li-doping concentration and is ready to extend to industrial scales [19]. There is also experimental evidence that the ILD of GIC can be expanded. It was proved that either type organic ligands can bind to alkali metal ions and cointercalate into the host carbons so that the interlayer distance of GIC can be expanded from around 3.4 \AA to $8.7\text{--}12.4 \text{ \AA}$ [20]. We believe that the same cointercalation synthesis method can be extended to SWNT

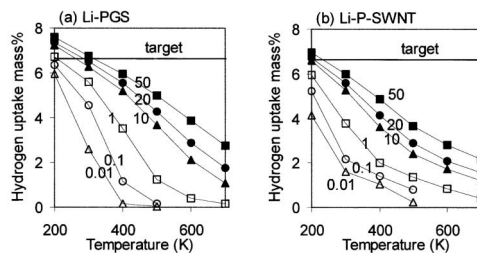


FIG. 4. Temperature and pressure (unit: bar) effects on the mass hydrogen storage capacity. (a) Li-PGS: Li:C = 1:3 and $ILD = 10 \text{ \AA}$; (b) Li-P-SWNT: Li:C = 1:3 and $ITD = 9 \text{ \AA}$.

systems to expand the intertube distances. Figure 5 proposes a possible scheme to synthesize a practical hydrogen-storage system such as the following:

- (i) Ternary compounds are first produced by the reaction between host carbons and 2,5-dihydrofuran solvated Li cation in low concentration such that the interlayer spaces of graphite are expanded.
- (ii) A Diels-Alder-type reaction between the organic solvents and the graphite sheets is triggered to build covalent bonds that would maintain the interlayer space under operating conditions.
- (iii) Li-intercalation and proper ball milling are used to synthesize PGS of higher Li concentration.

We have tested this process with computer simulations. For Li:C = 1:3, we considered one pillar per 116 carbons and find $ILD = 8.0 \text{ \AA}$. Carrying out GCMC calculations on this system we find 5.7 mass% hydrogen storage at 300 K and 50 bars. For maximum performance the pillar should be modified to yield $ILD = 10 \text{ \AA}$.

Summarizing, we have designed a series of new materials for H_2 storage: Li-PGS and Li-P-SWNT. We have tested and optimized the nanostructure of these Li-doped

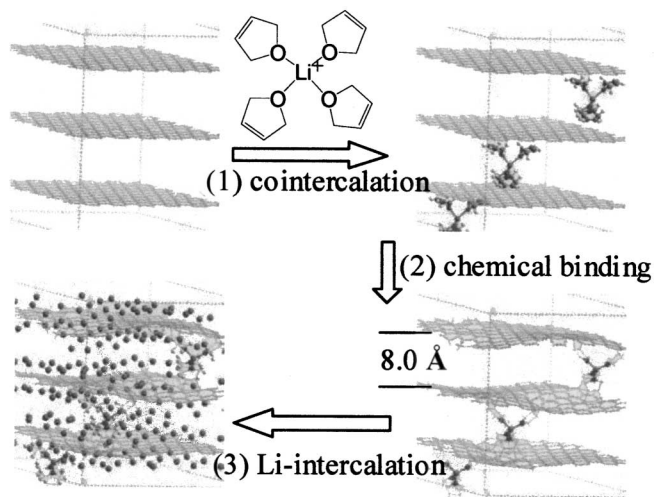


FIG. 5. A scheme to synthesize the Li-doped pillared graphene or nanotubes of high Li-doping concentrations and large interlayer distances.

carbon materials using grand canonical Monte Carlo simulations with a first principles-derived force field. We predict that for 1:3 Li:C doping and $ILD = 10 \text{ \AA}$, Li-PGS will lead to hydrogen storage of 6.5 mass% and 62.9 kg/m^3 at 20 bars and room temperature, attaining the DOE target. We find that Li-P-SWNT (1:3 Li:C doping and $ITD = 9 \text{ \AA}$), can lead to a hydrogen-storage capacity of 6.0 mass% and 61.7 kg/m^3 at 50 bars and room temperature storage, which is close to the DOE target. We also suggest ways to synthesize these systems by cointercalation of solvated Li ion followed by Li-intercalation and ball milling.

This work was supported by the General Motors Corporation (Dr. Gerald Voecks). The facilities of the Materials and Process Simulation Center (MSC) used in these studies were funded by DURIP (ARO and ONR), NSF (CTS and MRI), and a SUR grant from IBM. In addition, the MSC is funded by grants from ARO-MURI, NIH, ChevronTexaco, General Motors, Seiko-Epson, the Beckman Institute, Asahi Kasei, and the Toray Corporation.

*On sabbatical leave from Xiamen University, Xiamen 361005, China.

†To whom correspondence should be addressed.

Email address: wag@wag.caltech.edu

- [1] L. Schlapbach and Z. Zuttel, *Nature* (London) **414**, 353 (2001), and references therein.
- [2] M. Hirscher *et al.*, *Appl. Phys. A-MATER* **72**, 129 (2001).
- [3] Y. Ye *et al.*, *Appl. Phys. Lett.* **74**, 2307 (1999).
- [4] A. C. Dillon *et al.*, *Nature* (London) **386**, 377 (1997); A. C. Dillon *et al.*, in *Proceedings of the 2000 Hydrogen Program Review* (NREL Report No. NREL/CP-507-28890, 2000).
- [5] C. Liu *et al.*, *Science* **286**, 1127 (1999); H. M. Cheng *et al.*, *Z. Metallkd.* **91**, 306 (2000).
- [6] C. C. Ahn *et al.*, *Appl. Phys. Lett.* **73**, 3378 (1998); Y. Y. Fan *et al.*, *Carbon* **37**, 1649 (1999).
- [7] D. J. Browning *et al.*, *Nano Lett.* **2**, 201 (2002).
- [8] S. Orimo *et al.*, *Appl. Phys. Lett.* **75**, 3093 (1999).
- [9] P. Chen *et al.*, *Science* **285**, 91 (1999).
- [10] R. T. Yang, *Carbon* **38**, 623 (2000).
- [11] F. E. Pinkerton *et al.*, *J. Phys. Chem. B* **104**, 9460 (2000).
- [12] To describe the van der Waals (vdW) interactions between the Li dopants, carbon materials, and hydrogen systems we use Morse potentials with the parameters determined by fitting to accurate *ab initio* calculations as described here. (i) For the H-H vdW term, we fitted the potential curve between two H_2 molecules using CCSD(T) *ab initio* QM with the aug-cc-pVQZ basis set. (ii) For the C-H vdW term, we calculated the interaction between H_2 and C_2 molecules using the MP4 *ab initio* QM with the aug-cc-pVTZ basis set plus midpoint bond functions. (iii) To determine the interactions between doped Li ions and hydrogen molecules, we considered a planar C_{32} cluster (ten aromatic rings) doped with one Li atom on each side (in the optimum configuration found for Li:C = 1:3 Li-PGS) to which one H_2 was bonded. These calculations used X3LYP [6-311G(d,p) basis set], a new DFT functional which leads to an accurate description of van der Waals and hydrogen bond interactions [14]. High quality *ab initio* calculations [MP4/6-311G(d,P)//MP2/6-311G(d,p)] have previously been reported [21] showing that Li cation binds six H_2 molecules at zero Kelvin with the enthalpy for adding successive H_2 of -5.39 , -4.3 , -4.07 , -3.65 , -1.87 , and -2.3 kcal/mol; this agrees well with the X3LYP results of -5.12 , -4.47 , -3.9 , -3.63 , -1.55 , and -1.52 kcal/mol for the same system.
- [13] The GCMC calculations were carried out using the sorption module of Cerius2 (Accelrys, San Diego) with the FF described in Ref. [15]. In order to obtain an accurate measure of H_2 loading, we used 1000 000 configurations to compute the average loading for each condition (pressure and temperature). To minimize undesirable boundary effects we used a finite three-dimensionally periodic cell containing four independent sheets each with 216 carbon atoms.
- [14] X. Xu and W. A. Goddard III, *Proc. Natl. Acad. Sci. U.S.A.* **101**, 2673 (2004).
- [15] G. H. Gao, T. Cagin, and W. A. Goddard III, *Phys. Rev. Lett.* **80**, 5556 (1998).
- [16] M. S. Dresselhaus *et al.*, *Science of Fullerenes and Carbon Nanotubes* (Academic Press, New York, 1996).
- [17] Q. Wang and J. K. Johnson, *J. Chem. Phys.* **110**, 577 (1999).
- [18] For these calculations we employed the CASTEP periodic QM software (from Accelrys) using the Perdew generalized gradient approximation II density functional combined with a plane-wave basis set. The geometries of Li-GIC or Li-PGS at various doping concentrations were fully optimized. We used a kinetic energy cutoff of 380 eV for the plane-wave basis set. We used the default convergence criteria which correspond to 0.0002 eV for the energy change per atom, 0.001 Å for the rms atomic displacement, and 0.05 eV/Å for the rms residual force.
- [19] R. Janot *et al.*, *Carbon* **39**, 1931 (2001).
- [20] T. Abe *et al.*, *Synth. Met.* **125**, 249 (2002); M. Inagaki *et al.*, *Carbon* **39**, 1083 (2001).
- [21] M. Barbatti *et al.*, *J. Chem. Phys.* **114**, 2213 (2001).